Università degli Studi di Ferrara

Dottorato di ricerca in Fisica XXII Ciclo

Coodinatore Prof. Filippo Frontera

Study of the $e^+e^- \to J/\psi\pi^+\pi^-$ Process via Initial-State Radiation at *BABAR*

Settore Scientifico Disciplinare FIS01

Dottorando Valentina Santoro

Advisor

Chiar. mo Prof. Roberto Calabrese

Anni 2006/2008

To Giuliana my wonderful little girl

Contents

Introduction **1**

1 Charmonium spectroscopy **3**

1.1 Introduction 3

1.2 Mass spectrum and potential model 4

1.3 Experimental techniques for charmonium study 11

1.3.1 e^+e^- annihilation 11

2 The New Heavy Mesons **17**

2.1 Introduction 17

2.2 The X(3872) 17

2.3 The Y(4260) 19

2.3.1 The discovery of the Y(4260) 19

2.3.2 Search for the Y(4260) in other decay modes 21

2.3.3 Search for the Y(4260) in $\psi(2S)\pi^+\pi^-$ 23

2.3.4 The possible theoretical interpretations of the Y(4260) 26

3 The *BABAR* experiment **31**

3.1 Introduction 31

3.2 The PEP-II Asymmetric Collider 33

3.3 The *BABAR* detector 37

3.3.1 The Silicon Vertex Tracker 39

3.3.2 Drift Chamber 40

3.3.3 Cherenkov detector 43
3.3.4 Electromagnetic calorimeter 47
3.3.5 The Instrumented Flux Return 50
3.3.6 Trigger, Data Acquisition and Reconstruction . . . 57

4 Study of the $J/\psi\pi^+\pi^-$ final state after ISR **61**
4.1 Event Selection 61
4.1.1 ISR cross section 61
4.1.2 Analysis strategy 62
4.1.3 Data and Monte Carlo samples 63
4.1.4 Event reconstruction 64
4.2 The selection criteria 65
4.3 Selection optimization 66
4.3.1 Checks on the selected events 74
4.3.2 Multiple candidates 79
4.3.3 Di-pion invariant mass distribution 79
4.4 Fit procedure and validation 80
4.4.1 Resolution studies 80
4.4.2 Fit to the $\psi(2S)$ data 82
4.5 Study of the $J/\psi\pi^+\pi^-$ mass spectrum 89
4.5.1 Study of resonance lineshape 89
4.5.2 Validation of the analysis on Run 1 to Run 4 data 90
4.6 Unblind the full dataset 90
4.7 Systematic errors 100

5 Conclusions **103**

Appendix **109**

Bibliography **113**

Introduction

Many new states have been recently discovered at the B-factories above the $D\overline{D}$ threshold in the charmonium energy region. While some of them appear to be consistent with conventional $c\bar{c}$ states others do not fit with any charmonium model expectation. Several interpretations for these states have been proposed: for some of them the mass values suggest that they could be conventional charmonia, but also other interpretations like $D^0\overline{D}^{*0}$ molecule or diquark-antidiquark states among many other models have been advanced. Reviews can be found in Refs. [1][2]. In all cases the picture is not completely clear.

Among the new charmonium-like states, the $Y(4260)$ is probably the most intriguing. Its discovery was reported by BaBar in the $J/\psi\pi\pi$ subsystem in the radiative return reaction $e^+e^- \to \gamma_{ISR}\ J/\psi\pi\pi$ [3]. Using 233 fb^{-1} of data, a broad enhancement has been observed at 4260 MeV/c^2, an unbinned fit with a Breit-Wigner signal function and a second order polynomial background yields 125 ± 23 $Y(4260) \to J/\psi\pi^+\pi^-$ events, with a mass $M_Y = 4259 \pm 8(stat)^{+2}_{-6}(syst)$ MeV/c^2 and a width $\Gamma_Y = 88 \pm 23(stat)^{+6}_{-4}(syst)$ MeV. The $Y(4260)$ has been searched also in $e^+e^- \to \gamma_{ISR}\ p\overline{p}$ events: no signal has been found so it was possible to set the upper limit $\mathcal{B}(Y(4260) \to p\overline{p})/\mathcal{B}(Y(4260) \to J/\psi\pi^+\pi^-) < 13\%$ at 90% C.L. [4]. Looking for the $Y(4260)$ in the radiative return process $e^+e^- \to \gamma_{ISR}\ \psi(2S)\pi^+\pi^-$, where $\psi(2S) \to J/\psi\pi^+\pi^-$, BaBar observed a broad structure near 4.32 GeV, that is not consistent with the $\psi(4415) \to J/\psi\pi^+\pi^-$. A fit to the mass spectrum with a single resonance yields a mass of 4324 ± 23 MeV/c^2 and a width of 172 ± 33 MeV (where the errors are statistical only). This structure has a mass that differs somewhat from the reported for the $Y(4260)$, however, the possibility that it represents evidence for a new decay mode for the $Y(4260)$ cannot be ruled out at this time.

This sort of overpopulation of the expected 1^{--} states in the mass region above the $D\overline{D}$ threshold is increased by the report by Belle collaboration of two more enhancements in ISR $J/\psi\pi^+\pi^-$: $Y(4008)$ [5] and $\psi(2S)\pi^+\pi^-$ $Y(4660)$ [6] which still need a confirmation from BaBar.

This work is an update of the previous BaBar analysis. In this note we describe an analysis of the following ISR interaction.

$$e^+e^- \to \gamma\ J/\psi\pi^+\pi^-$$
$$\hookrightarrow e^+e^-,\ \mu^+\mu^-$$

We study the invariant mass spectrum of the $J/\psi\pi^+\pi^-$ system to search for new states with a mass beyond that of the $\psi(2S)$.

Chapter 1

Charmonium spectroscopy

1.1 Introduction

The charmonium system was discovered in 1974, when two experimental groups, at SLAC and Brookhaven, announced almost simultaneously the observation of a new narrow resonance, called J/ψ[7]. This was followed very shortly by the discovery by the SLAC group of another narrow state, which was called ψ'[8]. These two resonances were interpreted as bound states of a new quark, called the charm or c quark, and its antiquark ($\bar{c}$), whose existence had been predicted several years before to account for the non-existence of flavor changing neutral currents[9]. Since then the charmonium has proven to be a powerful tool for the understanding of the strong interaction. The high mass of the c quark ($m_c \approx 1.5 GeV/c^2$) makes it plausible to attempt a description of the dynamical properties of the ($c\bar{c}$) systems in terms of non-relativistic potential models, in which the functional form of the potential is chosen to reproduce the asymptotic properties of the strong interaction. The free parameters in these models are to be determined from a comparison with the experimental data.

More than thirty year after the J/ψ discovery, charm and charmonium spectroscopy continues to surprise and challenge. A new era began in April of 2003 when *BABAR* announced the discovery of the enigmatic $D_s(2317)$. Since then CLEO, BELLE, CDF and BES have joined the scrum and the number of new states has risen to double digits.

In 2005 *BABAR* discovered the Y(4260) in $J/\psi\pi^+\pi^-$ events after ISR (Initial state radiation). This resonance cannot be fully explained by a simple charmonium model, its nature is still unclear; four-quark state, hybrid and baryonium state are some of the interpretations that have been proposed to explain it. The primary purpose of

this work is the update of this analysis using the full *BABAR* data sample.

1.2 Mass spectrum and potential model

Since 1974, quarkonium production and decay is one of the most interesting field to test the quantum chromodynamics (QCD), in particular some effective theories like perturbative QCD (PQCD) and the non relativistic QCD (NRQCD). Quarkonium is a good testing ground for QCD since the energy levels are due to strong interaction. In particular, the heavy quarkonium system ($Q\bar{Q}$, where Q can be either c, the charm, or b the bottom flavor) can be treated with non relativistic models for the two valence quarks, with a great simplification of the theoretical treatment.
When two particles form a bound state, the attractive potential can be studied measuring the energy spectrum of the system. In atomic physics, the binding energy of the electron-nucleus system depends on the orbital angular momentum (L), spin (S) and total angular momentum ($J = L + S$) state (neglecting the nucleus angular momentum I). The spectroscopic notation $n^{2S+1}L_J$ is used to classify the energy levels of the system. A similar pattern of energy levels is present in positronium (the e^+e^- bound state) this has been used to study the potential between the electron and positron. The same concept can be applied also to the mesons the quark-antiquark ($\bar{q}q$) bound state. The intrinsic parity P and charge conjugation C of a charmonium state are related to the angular momentum by the relations:

$$\begin{aligned} P &= (-1)^{L+1} \\ C &= (-1)^{L+S} \end{aligned}$$

for this reason for the quarkonium system is often used the J^{PC} notation.

The charmonium spectrum consists of eight narrow states below the threshold for open charm (3.73GeV)and several tens of states above the threshold, some of them wide (because they decays to $D\bar{D}$), some of them still narrow, because their decay to open charm is forbidden by some conservation rule. Below the threshold almost all states are well established, with the possible exception of the 1^1P_1 (h_c) which has been observed recently but whose properties still need to be measured accurately. On the other hand, very little is known above the threshold. Only one state has been positively identified as a charmonium D state, the $\psi(3770)$, then there are several new state, first of all the $X(3872)$ discovered in B decays, that are

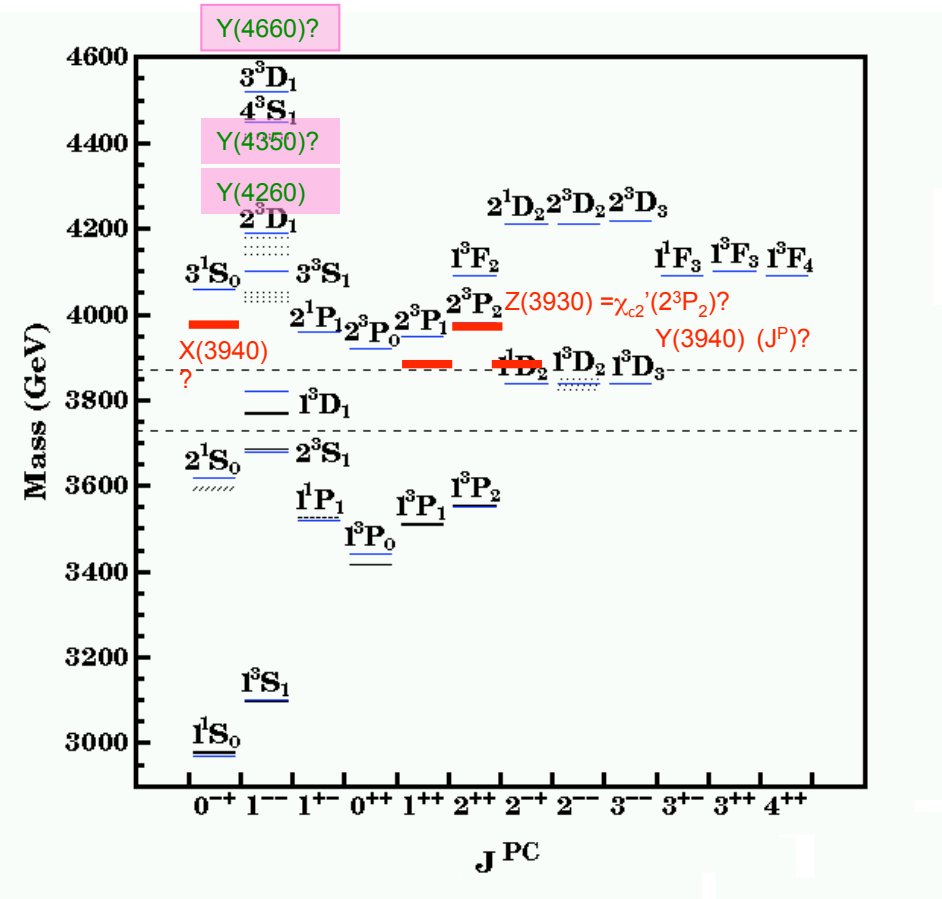

Figure 1.1: The charmonium spectrum with the new "charmonium-like" states.

very difficult to accommodate in the charmonium spectrum. More about these new state will be discussed in the next chapter.
Event though the charmonium mass spectrum is qualitatively similar to the positronium spectrum, the non perturbative feature of QCD prevent the possibility of describing it on the basis of the fundamental theory of interaction. For this reason the natural approach to the charmonium spectroscopy is to build an effective potential model. This approximation allow to integrate out many fundamental effects like gluon emission or light quark pairs and to deal with an effective potential which is the result of the $Q\bar{Q}$ direct interaction as well as the energy of the gluon field. This potential should nevertheless reproduce the two main features of the bound quark states in the two limits of small and large distance asymptotic freedom and confinement. Any potential written in this way must be flavor independent, so the following discussion made for the charmonium spectrum can be applied directly also to the bottomonium.
The $c\bar{c}$ system can be described with a Schrödinger equation:

$$H\mathbf{\Psi}(x) = E\mathbf{\Psi}(x) \tag{1.1}$$

where the hamiltonian for the $c\bar{c}$ can be written as

$$H = H_0 + H^{'} \tag{1.2}$$

and H_0 can be expressed by a free particle hamiltonian plus a non-relativistic potential $V(r)$

$$H_0 = 2m_c + \frac{p^2}{m_c} + V(r) \tag{1.3}$$

where m_c is the charm quark mass and p its momentum. $H^{'}$ includes the spin and the orbital dependent part of the strong interaction, explaining the charmonium fine structure.
$V(r)$ can be built thinking at the properties of strong interaction in the limit of small and large distances. At small distance the potential between the quarks is coulomb-like:

$$V(r) \sim -\frac{4}{3}\frac{\alpha_s(r)}{r} \tag{1.4}$$

where r is the distance between the quarks and α_s is the strong coupling constant. The value of the running coupling constant α_s depends on the energy scale of the interaction μ (Fig 1.2).

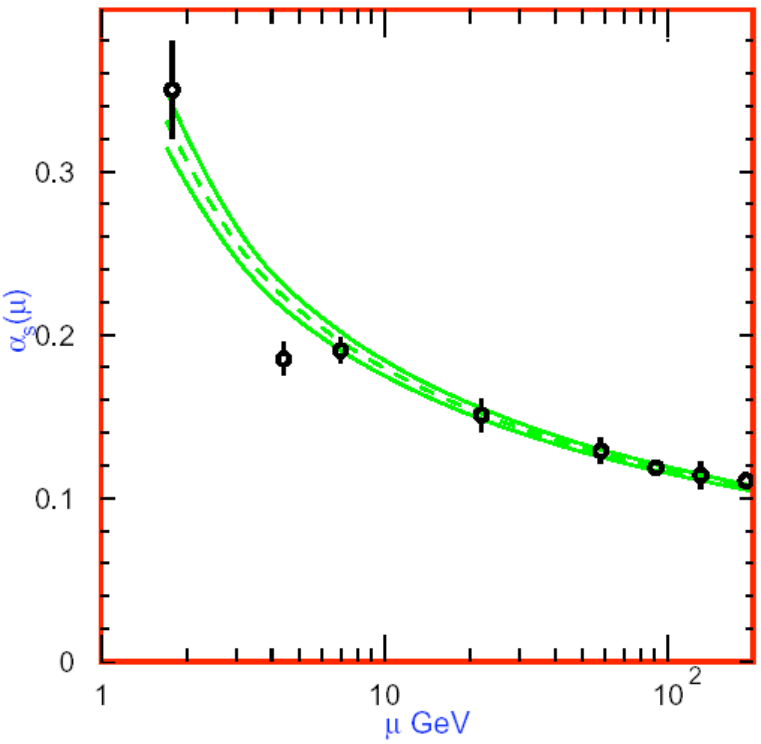

Figure 1.2: Behaviour of α_s[10].

At the leading order in the inverse power of $\ln(\mu^2/\Lambda^2)$, it is described by:

$$\alpha_s(\mu) = \frac{4\pi}{\beta_0 \ln(\mu^2/\Lambda^2)} \tag{1.5}$$

$$\beta_0 = 11 - \frac{2}{3}n_f \tag{1.6}$$

where $\Lambda \simeq 0.2$ GeV is the non-perturbative scale of QCD (the energy where 1.6 diverges) and n_f is the number of quarks lighter than the energy scale μ. It is clear from Equation 1.6 that, as the energy scale of a strong process decrease and become closer to Λ, α_s increases and the QCD can not be treated as a perturbative theory.

At large distance the "confinement" term is dominating. It can be written in the form:

$$V(r) \sim kr \tag{1.7}$$

where $k \simeq 1GeV \cdot fm^{-1}$ is called string constant. The energy of a $q\bar{q}$ system increase with the distance so the absence of free quarks in nature is explained by the confinement term.
The two behaviors can be put together to write the Cornell potential, shown in Figure 1.3 [11].

$$V(r) = -\frac{4}{3}\frac{\alpha_s(r)}{r} + kr \tag{1.8}$$

With this potential, the charmonium wave function can be expressed as:

$$\psi(r, \theta, \phi) = R_{nl}(r)Y_l^m(\theta, \phi) \tag{1.9}$$

but this is not enough accurate to reproduce the mass difference for charmonium states in the same orbital angular momentum or spin multiplets. To explain the charmonium fine structure one needs additional interaction term depending on S and L [12]

$$H^{'} = V_{LS} + V_{SS} + V_{tens} \tag{1.10}$$

the various term are described in the following:

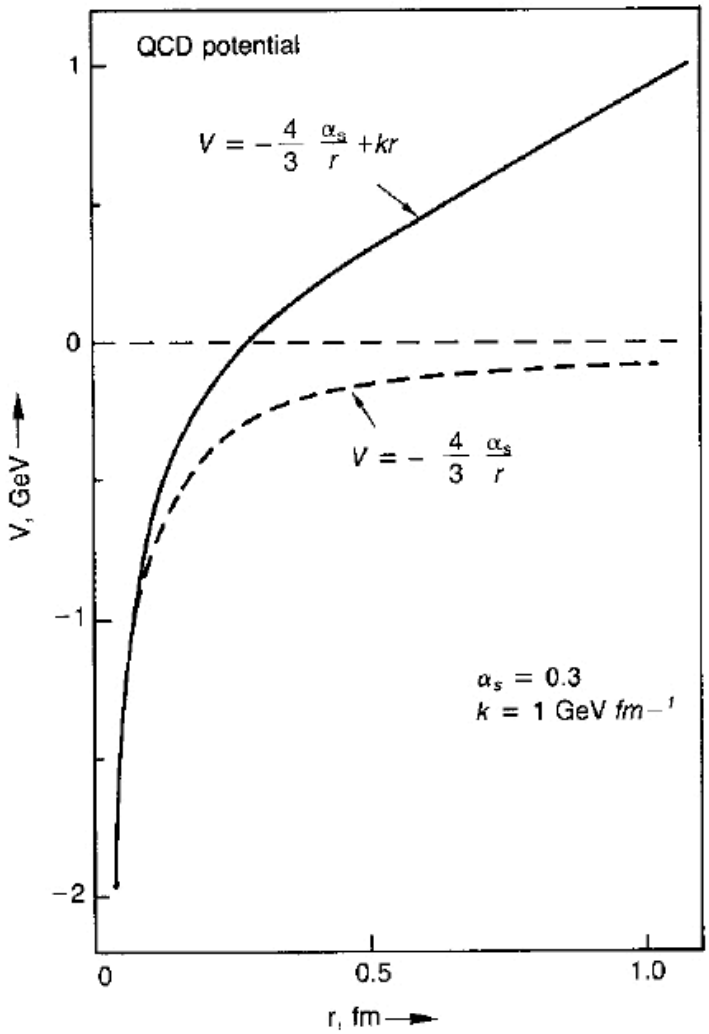

Figure 1.3: Cornell potential.

- **spin-orbit**: the spin orbit term splits the states with the same orbital angular momentum depending on the $\langle \mathbf{L} \cdot \mathbf{S} \rangle$ expectation value (fine structure):

$$V_{LS} = (\mathbf{L} \cdot \mathbf{S})(3\frac{dV_v}{dr} - \frac{dV_S}{dr})/(2m_c^2 r) \tag{1.11}$$

  where V_s and V_v are the scalar and vector components of the non relativistic potential $V(r)$

- **spin-spin**: this term describes the effect of the interaction between the spin of the quarks and is responsible of the splitting between the spin singlet and triplet (hyperfine structure)

$$V_{SS} = \frac{\mathbf{2}(\mathbf{S_1} \cdot \mathbf{S_2})}{3_c^2} \bigtriangledown^2 V_V(r) \tag{1.12}$$

  the expectation value for $\mathbf{S_1} \cdot \mathbf{S_2}$ is $+1/4$ for S=1 and $-3/4$ for S=0

- **tensor**: the tensor potential, in analogy with electrodynamics, contains the tensor effects of the vector potential

$$V_T = \frac{S_{12}}{12m_c^2}\left(\frac{1}{r}\frac{dV_V}{dr} - \frac{d^2V_V}{dr^2}\right) \tag{1.13}$$

$$S_{12} = 2[3(\mathbf{S} \cdot \hat{\mathbf{r}})(\mathbf{S} \cdot \hat{\mathbf{r}}) - S^2] \tag{1.14}$$

The Coulomb-like part of $V(r)$ corresponds to one gluon exchange and contributes only to vector part V_v of the potential, the scalar part V_S is due to the linear confining potential. The linear confining term could in principle contribute to both V_S and V_V but the fit of the χ_{cJ} masses suggest that the V_V contribution is small [13]. The theory can not predict the coefficients weighting the different contributions from the various terms of potential 1.10. In addition, all the theoretical energy levels can be corrected to take into account relativistic effects. All those contributions need to be compared with experimental data of charmonium spectroscopy to evaluate the relative weight.
Another possibility to predict the charmonium mass spectrum is to compute it with the lattice QCD, which is essentially QCD applied to a discrete 4 dimensional space. The field theory fundamental principles and the path integral can be used to calculate the properties of the strong interaction. The value of the lattice spacing, usually denoted with a, can be decided depending on the specific problem that has

to be solved. Another important parameter is the QCD bare coupling constant g, or $\beta = 6/g^2$ [14]. Typical value are $\beta \approx 6$ and $a \approx 0.1fm$. The physical quantities can be obtained in the limit $a \to 0$.

1.3 Experimental techniques for charmonium study

1.3.1 e^+e^- annihilation

The earlier studies of charmonium spectroscopy were performed almost exclusively at e^+e^- colliders. In these experiment e^+e^- annihilation proceeds primarily through an intermediate virtual photon, creating a bound $c\bar{c}$ state, as show in Fig 1.4. Other production mechanism include photon-photon fusion, initial state radiation and B-meson decay.

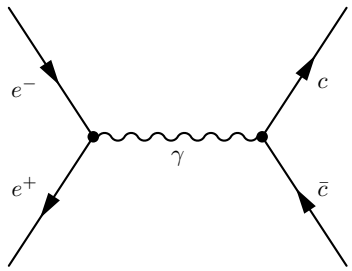

Figure 1.4: The Feynman diagram for the process $e^+e^- \to c\bar{c}$.

In addition to that, the production of double charmonium in e^+e^- annihilation has been observed at the B factories.
Many experiments have studied charmonium physics in e^+e^- annihilations: the early SLAC experiments Mark I, II and III, TPC and Crystal Ball; the DASP and PLUTO experiments at DESY; CLEO and CLEO-c at the Cornell Storage Ring; the LEP experiments; the BES experiment at the BEPC collider in Beijing; *BABAR* and Belle at the SLAC and KEK-B B factories, respectively. We will now turn to a discussion of the individual charmonium production mechanism.

Direct formation

In e^+e^- annihilations direct charmonium formation is possible only for states with the quantum numbers of the photon $J^{PC} = 1^{--}$, namely the J/ψ ,ψ' and $\psi(3770)$ resonances. Precise measurement of the masses and widths of these states can be obtained from the energy of the electron and positron beams, which are known with good accuracy. All other states are produced in the radiative decays of the $J^{PC} = 1^{--}$ resonances. This is illustrated in Fig 1.5 , which shows the inclusive photon spectrum from the Crystal Ball experiment from the process [15]

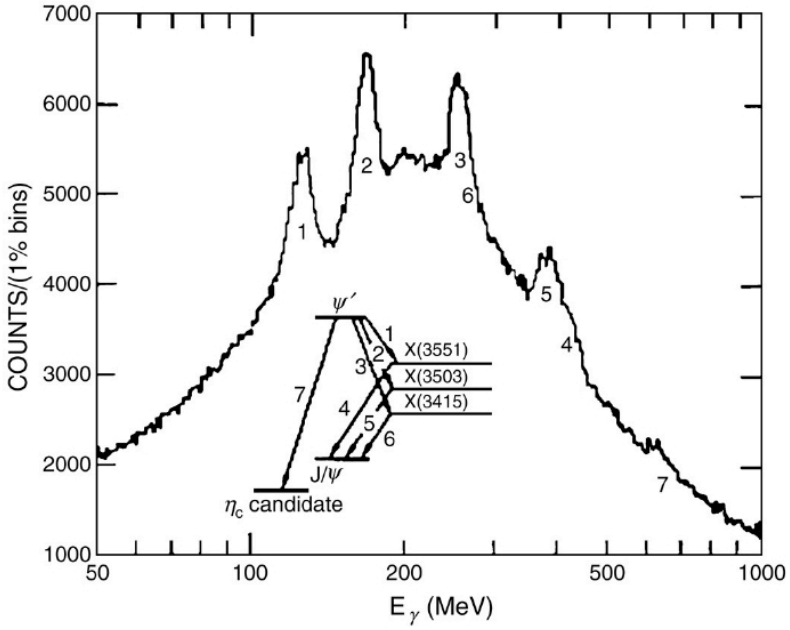

Figure 1.5: The inclusive photon spectrum from the Crystal Ball experiment .

$$e^+e^- \rightarrow \psi(2S) \rightarrow \gamma + X \tag{1.15}$$

The peak marked with the number 1, 2, 3, and 7 corresponds to the $c\bar{c}$ states which can be reached from the ψ' via radiative transition, namely the $\chi_{cJ}(1^3P_J)$ and the $\eta_c(1^1S_0)$; 4, 5, and 6 corresponds to the radiative decays form the χ_{cJ} states to the J/ψ. The parameters of these resonances are determined from the measurement of the recoil photon energy; as a consequence, the precision in the measurement of the masses and widths of these states is limited by the detector resolution, which

is worse than the precision with which the beam energies are known. A further disadvantages is that radiative cascades which involves small branching ratios or multiple steps are difficult to observe.

Two-photon production

Electron-positron annihilations at high energies can produce the J-even charmonium states through two virtual photons via the process

$$e^+e^- \rightarrow e^+e^- + (c\bar{c}) \tag{1.16}$$

this is illustrated in 1.6. The production rate in this case decrease by a factor of α^2 from the rate for a single photon, where α is the fine structure costant. The $(c\bar{c})$ state is usually identified by means of its hadronic decays.

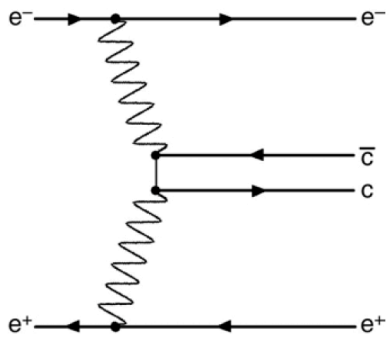

Figure 1.6: The Feynman diagram for the $\gamma\gamma$ fusion process .

Initial state radiation (ISR)

Another mechanism for the production of charmonium states in e^+e^- collisions is Initial State Radiation (ISR). In this process illustrated in Fig 1.7, either the electron or the positron radiates a photon before the annihilation, thereby lowering the effective center-of-mass energy. Like in direct formation only $J^{PC} = 1^{--}$ states can be produced. This process allow a large mass range to be explored and is very useful for the measurement of R, the ratio of the total $e^+e^- \rightarrow hadrons$ cross section to the $e^+e^- \rightarrow \mu^+\mu^-$ cross section, and in the search for new vector states.

This technique is used in the analysis that will be presented in the chapter 3.

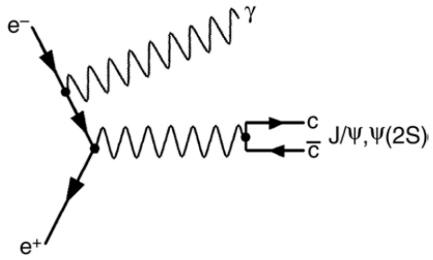

Figure 1.7: Initial state radiation production of charmonium .

B meson decays

Charmonium states can be produced in the (color suppressed) decays of the B mesons, as shown in Fig 1.8. The large data samples available at the B factories made this approach very powerful to study known states, as well as the discovery of new resonances.

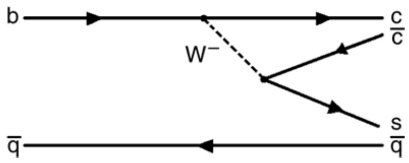

Figure 1.8: B mesons decay to charmonium .

The discovery of $\eta_c(2S)$ [16] and X(3872) [17] are recent example which illustrate well the discovery potential of the B factories. The decays of the B meson provide a clean production environment for charmonium. States of any quantum number can be formed. The small production rates can be overcome by restricting the study to specific exclusive final states, to take advantage of the B mass and beam energy constraints.

Double charmonium

The production of double charmonium in e^+e^- annihilation (illustred in Fig 1.9) was discovered by the Belle collaboration studying the recoil momentum spectrum of the J/ψ in $e^+e^- \to J/\psi + X$ [18]

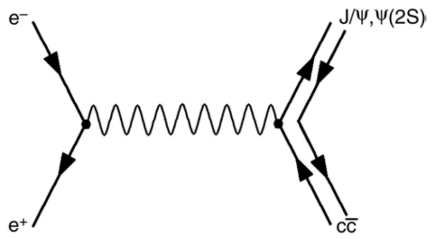

Figure 1.9: Double charmonium production in e^+e^- .

The collaboration measured the production cross section for $J/\psi+\eta_c$. In addition to that, they found also evidence for $J/\psi + \chi_{c0}$ and $J/\psi + \eta_c^{'}$ production.

$p\bar{p}$ ANNIHILATION.

The intrinsic limitations of e^+e^- experiments, where direct formation is possible only for $J^{PC} = 1^{--}$ states can be overcome by using $p\bar{p}$ annihilation: in this case the coherent annihilation of the three quarks in the proton with the three antiquarks in the antiproton makes it possible to form directly states with all quantum numbers, via intermediate states with the appropriate number of gluons and/or virtual $q\bar{q}$ pairs. Fig 1.10 shows as an example the annihilations via two- and three-gluon intermediate states for C-even and, respectively C-odd charmonium states. This technique, originally proposed by Dalpiaz in 1979 [19], became successfully employable a few years later thanks to the development of stochastic cooling.
The resonant formation of charmonium state in $p\bar{p}$ annihilations has been studied at the CERN Intersecting Storage Rings by the R704 experiment(1983-1984), and at the Fermilab antiproton accumulator by the E760 (1990-1992) and E835 (1996-2000) experiments. In all three experiment a high luminosity, nearly point-like annihilations source was obtained by intersecting the $\bar{p}$ beam with an internal hydrogen gas jet target. With this arrangement, peak luminosities up to $5 \times 10^{31} cm^{-2} s^{-1}$ have been reached.

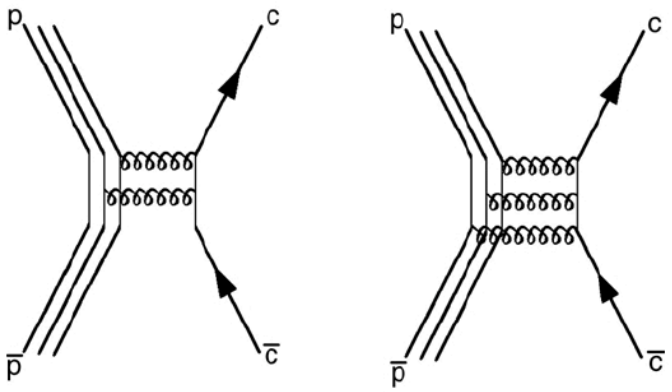

Figure 1.10: Charmonium formation in $p\bar{p}$ annihilation via two-and three-gluon intermediate states .

Chapter 2

The New Heavy Mesons

2.1 Introduction

For many years it was possible to consider the charmonia as a "well" understood system: the spectrum of low-lying states was well-established, with one or two gaps, as were the major transitions. However recently there has been s long list of discoveries, or claims of evidence: the h_c, the η_c and an alphanumeric soup of "X", "Y" and "Z" mesons, some understandable as $c\bar{c}$ states, some where a conventional assignment is elusive. This revival in spectroscopy is due in part to the large datasets accumulated at the B-factories. In the following paragraph I will focus on the X(3872) and on the Y(4260), since the X(3872) was the first state that was not easy to fit in the charmonium spectroscopy, and the study of the Y(4260) is the aim of this work.

2.2 The X(3872)

The X(3872) is the poster boy of the new heavy hadrons - it has been observed by four experiments in three decay modes and two production channels and continues to refuse to fit into our expectations for charmonium. The X(3872) was found by BELLE [17], with a clear sign in decays $B^+ \to K^+ X[J/\psi\pi^+\pi^-]$ as shown in Fig. 2.1. The observation agree on a peak with natural width below experimental resolution. It is importanto to note that the mass of the X(3872)= 3872.2 ± 0.8 MeV is very close to the $D^0\overline{D}^{*0}$ threshold 3871.8 ± 0.4 MeV.
Soon after its discoveries numerous theoretical explanation have been proposed. The possibilities include a bound state of $D^*\bar{D}$ very close to $D^{*0}\overline{D}^0$ threshold [28], a hybrid charmonium [29], a diquark-antidiquark state [30], and a conventional

charmonium state [31].

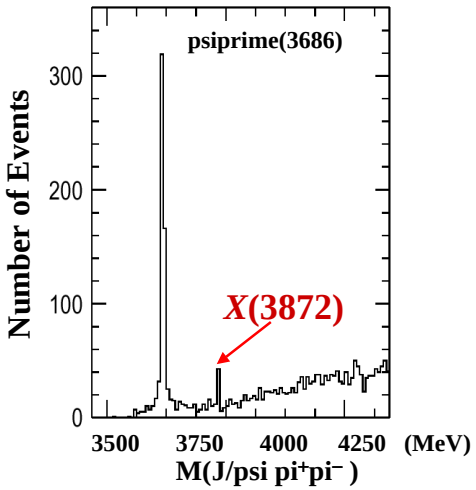

Figure 2.1: The X(3872) in $J/\psi\pi^+\pi^-$. The high energy peak is due to the $\psi(2S)$

A recent CDF [20] analysis suggests that the $\pi^+\pi^-$ distribution is dominated by an intermediate ρ meson (Fig 2.2). The decay of the X(3872) $\rightarrow J/\psi\rho$ would have indicated that if the X(3872) is a a charmonium state, the decay would have violated isospin. Since it would be quite unusual to have the dominant decay to be isospin violating, a search of the isospin partner $X^+ \rightarrow J/\psi\rho$ was conducted in vain by *BABAR* [21] . The quantum number of X(3872) are not yet determined: BELLE [22] and *BABAR* [23] observed the decay in $J\psi\gamma$ (which implies C=+1). Both CDF [20] and BELLE [24] performed an angular analysis of $J/\psi\pi^+\pi^-$: the most likely assignment are $J^{PC} = 1^{++}$,2^{-+}. In addition *BABAR* has published an analysis of the $B \rightarrow XK$ with $X \rightarrow D^{*0}D^0$ [27] and BELLE report evidence of decays to $D^0\overline{D}^0\pi^0$. [26].

In summary, a narrow state at 3871.9 MeV is seen in B decays and $p\bar{p}$ collisions but its interpretation need still more data to be clarified.

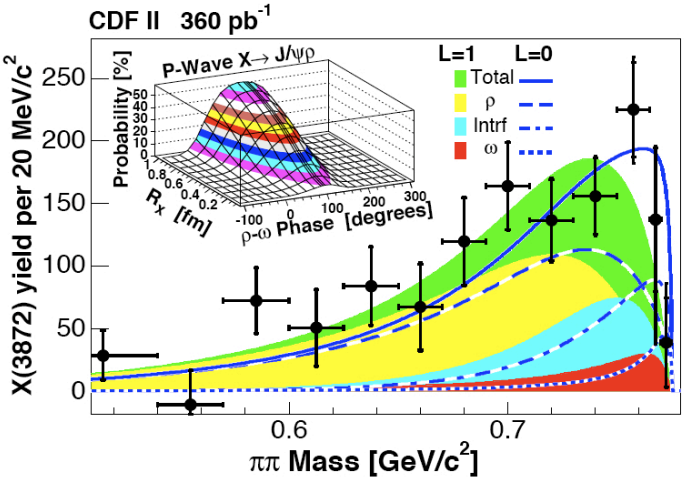

Figure 2.2: $\pi^+\pi^-$ invariant mass distribution for the X(3872) .

2.3 The Y(4260)

2.3.1 The discovery of the Y(4260)

In 2005 *BABAR* discovered the Y(4260) $\rightarrow J/\psi\pi^+\pi^-$ [33] in the ISR reaction e^+e^- $\rightarrow \gamma_{ISR}\ J/\psi\pi^+\pi^-$ using $233fb^{-1}$ of data, where the detection of ISR photon was not required. They found an unexpected bump with width less than 100MeV as shown in Fig 2.3. The mass region between 3.8 and 5.0 GeV/c^2 is fitted with a Breit-Wigner signal function and a second order polynomial background. The sub-figure shows a broader mass region with 2 peaks: the high peak is due to $\psi(2S)\pi^+\pi^-$ and the low peak at mass ~ 4.26 is due to the Y(4260).

The number of signal events extracted from the fit is 125 ± 23, the mass is $M_Y = 4259 \pm 8^{+2}_{-6} MeV/c^2$ and the width is $\Gamma_Y = 88 \pm 23^{+6}_{-4} MeV$. The branching fraction obtained is $\Gamma_{Y,ee} * BF(Y(4260) \rightarrow J/\psi\pi^+\pi^-) = 5.5 \pm 1.0^{+0.8}_{-0.7}\ eV$. Since it is produced in ISR events we know that the $J^{PC} = 1^{--}$.
The invariant mass of the $\pi^+\pi^-$ is not consistent with the phase space model as shown in Fig 2.4. The high peak around 1 GeV may suggest the possible contribution of the $f_0(980)$.

Soon after its discovery the Y(4260) was confirmed in the same production process by CLEO [34] and in direct production by CLEO-c [35]. The latter paper studies several decays mode reported in the table 2.1. They found evidence for the

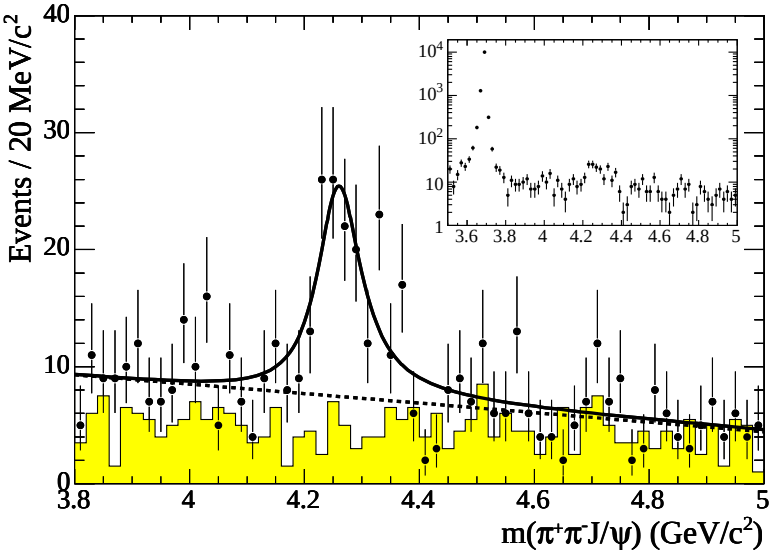

Figure 2.3: The $J/\psi\pi^+\pi^-$ invariant mass distribution in the range 3.8,5.0 GeV/c^2. The dots represent the data, the filled histogram shows the background from the J/ψ sidebands, the solid-curve represents the fit result and the dashed line show the background .

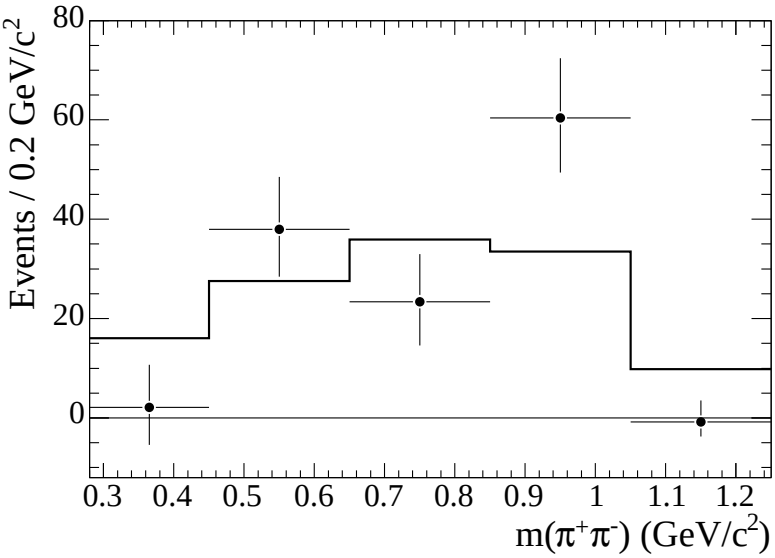

Figure 2.4: The $\pi^+\pi^-$ invariant mass distribution for the Y(4260) $\rightarrow J/\psi\pi^+\pi^-$ data is shown as points with error bars. The histogram shows the distribution for Monte Carlo events where Y(4260) $\rightarrow J/\psi\pi^+\pi^-$ is generated according to an S-wave phase space model.

decay of the Y(4260) in $J/\psi\pi^0\pi^0$ (5.1 σ) and $J/\psi K^+K^-$ (3.8 σ).

Table 2.1: Y(4260) decays mode studied by CLEO ($\sqrt{s}$= 4260MeV). ϵ is the detector efficiency, N_s the signal events and N_B the background events and σ is the $e^+e^- \to$ Y(4260) cross section. Upper limit are at 90% CL.

Channel	ϵ (%)	N_s	N_b	σ (pb)
$\pi^+\pi^-\ J/\psi$	38	37	2.4	$58^{+12}_{-10} \pm 14$
$\pi^0\pi^0\ J/\psi$	22	8	0.3	$23^{+12}_{-8} \pm 1$
$K^-K^+\ J/\psi$	21	3	0.07	$9^{+9}_{-5} \pm 1$
$\eta\ J/\psi$	16	5	2.7	< 32
$\pi^0\ J/\psi$	22	1		< 12
$\eta^{'}\ J/\psi$	11	0	1.5	< 19
$\pi^+\pi^-\pi^0\ J/\psi$	22	0		< 7
$\eta\eta\ J/\psi$	6	1		< 44
$\pi^+\pi^-\psi(2S)$	19	0		< 20
$\eta\psi(2S)$	15	0		< 25
$\omega\chi_{c0}$	9	11	11.5	< 25
$\gamma\chi_{c1}$	26	1	3.3	< 90
$\gamma\chi_{c2}$	27	4	3.3	< 90
$\pi^+\pi^-\pi^0\chi_{c1}$	9	0		< 46
$\pi^+\pi^-\pi^0\chi_{c2}$	9	0		< 96
$\pi^+\pi^-\phi$	18	7	5.5	< 5

The decay $J/\psi\pi^0\pi^0$ is particular interesting since it tells us that the Y(4260) isospin is I=0. The Y(4260) was confirmed also by the BELLE experiment that report another more enhancement in ISR $J/\psi\pi^+\pi^-$ the $Y(4008)$ [73] a broad resonance with the following parameters $M_{Y(4008)} = 4008 \pm 40^{+114}_{-28}$ and $\Gamma_{Y(4008)} = 226 \pm 44 \pm 87$.

They fit the mass distribution with two coherent Breit-Wigner as shown in Fig 2.5, assuming there is no continuum production of $e^+e^- \to J/\psi\pi^+\pi^-$.

2.3.2 Search for the Y(4260) in other decay modes

Since the Y(4260) decay to $J/\psi\pi^+\pi^-$ the natural explanation is that contain $c\bar{c}$ quarks. If this state is a conventional charmonium state is expected to decay with a large BR to $D\bar{D}$. However *BABAR* search for $D\bar{D}$ decays [37] but they did not find any evidence as shown in Fig 2.6. The upper limit is:

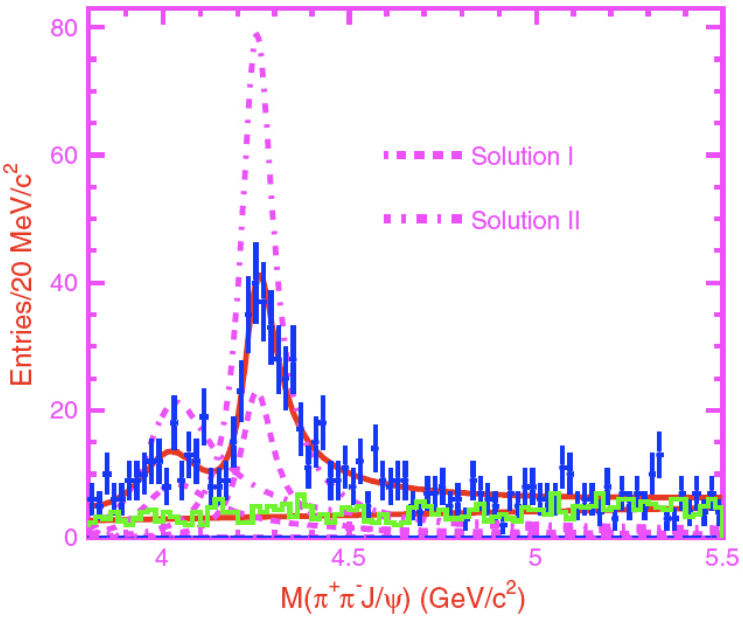

Figure 2.5: Fit to $J/\psi\pi^+\pi^-$ invariant mass spectrum with two coherent resonances. The curves show the best fit and the contribution from each component. The histogram shows the scaled sideband distribution .

$$\frac{\mathcal{B}(Y(4260) \to D\bar{D})}{\mathcal{B}(Y(4260) \to J/\psi\pi^+\pi^-)} < 1.0 \ (90\%C.L.) \tag{2.1}$$

This unique feature intrigues many speculation on its nature.

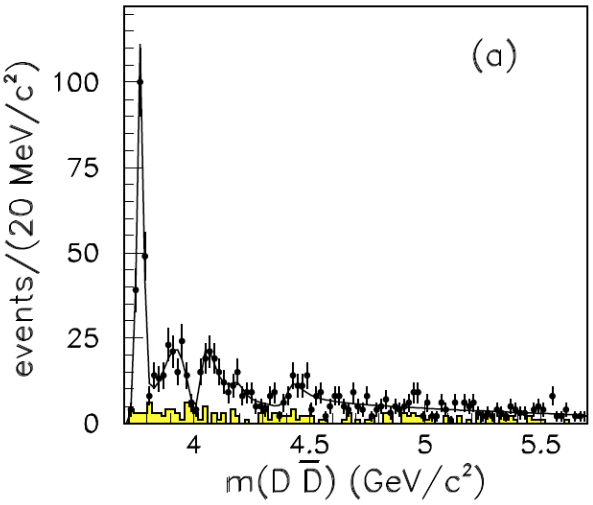

Figure 2.6: The ISR $D\bar{D}$ invariant mass spectrum, summed over all reconstructed final states. The shaded mass spectrum is from $D\bar{D}$ mass sidebands.

Other decay modes studied by *BABAR* in which there was no evidence of the Y(4260) are:

- $Y(4260) \to \phi\pi^+\pi^-$, $\Gamma^Y_{ee} \times \mathcal{B}(Y(4260) \to \phi\pi^+\pi^-) < 0.4\ eV\ 90\%CL$ [38]
- $Y(4260) \to p\bar{p}$, $\frac{\mathcal{B}(Y(4260)\to p\bar{p})}{\mathcal{B}(Y(4260)\to J/\psi\pi^+\pi^-)} < 0.13\ (90\%C.L.)$ [39]

Finally the Y(4260) has been searched also in B decays [40] by *BABAR* in $B^\pm \to K^\pm\ J/\psi\pi^+\pi^-$ they report "an excess of events" around 4.3 GeV with a significance around 3 σ.

2.3.3 Search for the Y(4260) in $\psi(2S)\pi^+\pi^-$

Since the Y(4260) decays in $J/\psi\pi^+\pi^-$ is natural to search for the decay mode to $\psi(2S)\pi^+\pi^-$. *BABAR* using 298 fb^{-1} study the process $e^+e^- \to \gamma_{ISR}\ \psi(2S)\pi^+\pi^-$ [75]. The interesting surprise was that they did not see any evidence of the Y(4260) but they saw a new structure: the Y(4320) as show in Fig 2.7 incompatible both

with the Y(4260) (the probability that the two structures are the same is 6.5×10^{-3}) and with the $\psi(4415)$ (2.0×10^{-9}).

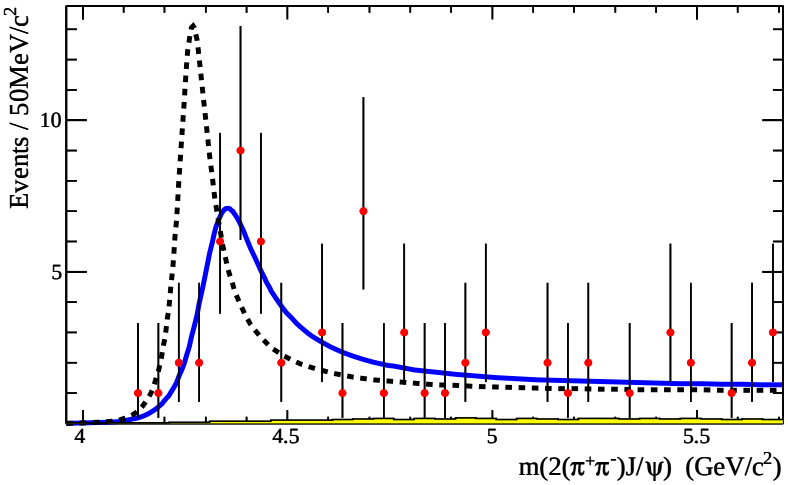

Figure 2.7: The $2(\pi^+\pi^-)J/\psi$ invariant mass spectrum up to 5.7 GeV/c^2 for the final sample. The shaded histograms represents the fixed background and the curves represent the fits to the data. The dotted line is the Y(4260) line shape.

While the absence of the Y(4260) $\rightarrow \psi(2S)\pi^+\pi^-$ could be explained if the pion pairs in the $J/\psi\pi^+\pi^-$ decay were produced with an intermediate state that is too massive to be produced with a ψ(2S) (e.g. an f^0), the absence of the $Y(4320)$ $\rightarrow J/\psi\pi^+\pi^-$ is still to be understood, more statistics might be needed in case the $Y(4260)$ decay hides the $Y(4320)$.

Recently BELLE has published the confirmation of the $Y(4320)$ [76]. Furthermore, they have unveiled a new state that was not clearly visible in the *BABAR* data due to the limited statistics the $Y(4660)$. As shown in Fig 2.8.

A critical piece of information for unravelling the puzzle is whether the pion pair comes from a resonant state.

Fig 2.9 shows the $\pi^+\pi^-$ invariant mass-spectra published by BELLE for all the regions where new resonances where observed. There is some indication that only the $Y(4660)$ has a well defined intermediate state (most likey an f^0) while others have a more complex structure.

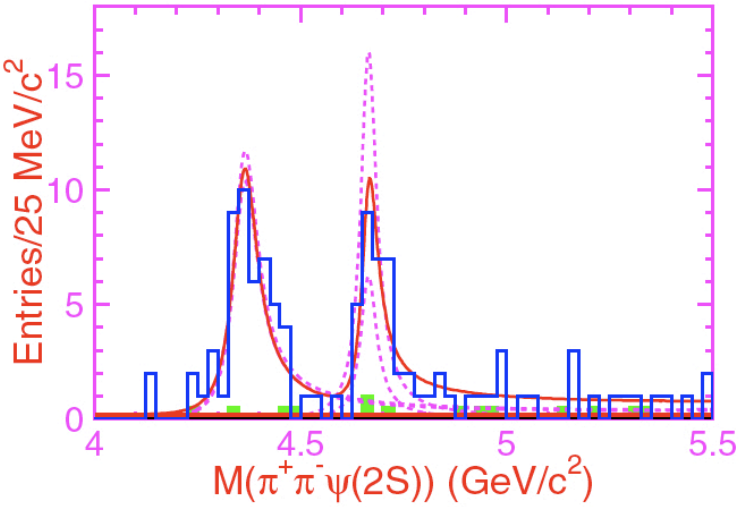

Figure 2.8: The $2(\pi^+\pi^-)J/\psi$ invariant-mass distribution. The open histogram is the data while the shaded histogram is the normalized ψ(2S) sidebands. The curves show the best fit with two coherent resonances together with a background term and the contribution from each component. The interference between the two resonances is not shown. The two dashed curves at each peak show the two solutions.

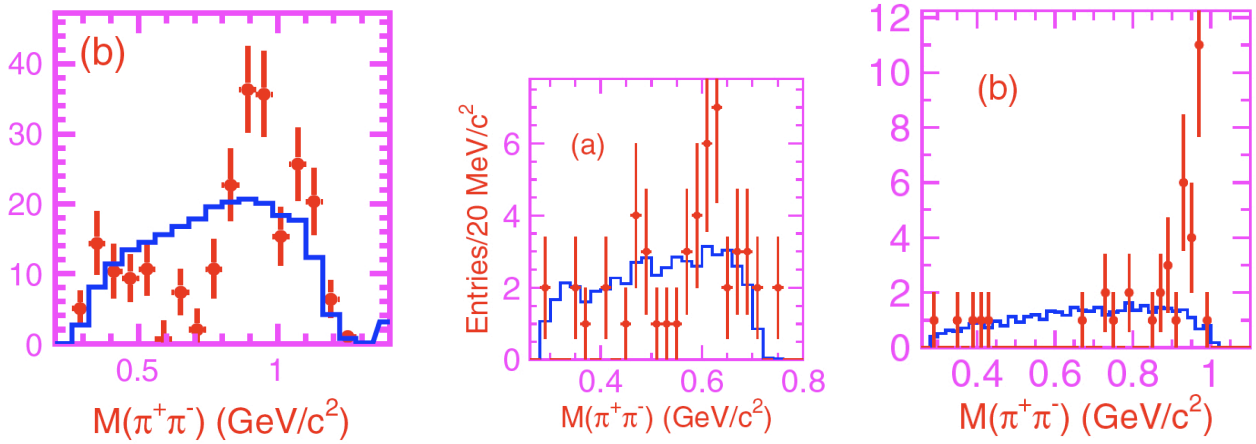

Figure 2.9: (a) $\pi^+\pi^-$ invariant mass distribution in $Y(4260) \to J/\psi\pi^+\pi^-$. (b) $\pi^+\pi^-$ invariant mass distribution in $Y(4320) \to \psi(2S)\pi^+\pi^-$. (c) $\pi^+\pi^-$ invariant mass distribution in $Y(4660) \to \psi(2S)\pi^+\pi^-$.

2.3.4 The possible theoretical interpretations of the Y(4260)

The Y(4260) lies far above the decay threshold with a width less than 100MeV. It's very difficult to accommodate Y(4260) as a conventional $c\bar{c}$ radial excitation or a D-wave. In the next sections are presented the possible theoretical interpretations of the Y(4260) and why some possible interpretations are excluded.

Conventional $c\bar{c}$ state.

With $J^{PC} = 1^{--}$, a conventional $c\bar{c}$ state is either a radial excitation or a D wave state. From PDG [43], the masses of the well-established radial excitation: $\psi(2S)$, $\psi(3S)$, $\psi(4S)$ are 3686MeV, 4040 MeV, 4415MeV respectively. Furthermore none of these state has been observed decay to $J/\psi\pi^+\pi^-$. The mass of $\psi(1^3D_1$ and $\psi(2^3D_1$ are 3770MeV and 4159 ± 20MeV [43]. The $\psi(3^3D_1$ state should lie above 4.5 GeV. Therefore, it's nearly impossible to accommodate Y(4260) as a conventional charmonium radial excitation or a D-wave state.

Molecule.

Hadronic molecules are states which lie below the continuum threshold and carry a small amount of binding energy. Y(4260) lies far above the $D\bar{D}$, $\omega J/\psi$ threshold.
One may wonder whether Y(4260) is a hadronic molecule composed of $\bar{D}_s D_{sj}(2317)$ since it is only 26MeV below $\bar{D}_s D_{sj}(2317)$ threshold. However the angular momentum and parity conservation exclude the possibility of $\bar{D}_s D_{sj}(2317)$ forming a 1^{--} molecular state.
Y(4260) is 24 MeV below $\bar{D}D_1(2420)$ threshold but the $D_1(2420)$ is a very narrow resonance. Its total width of $50 \sim 90$ MeV disfavors the identification as a $\bar{D}D_1(2420)$ molecular state. The total width also disfavors the identification as a $\bar{D}D_1^{'}$ or $\bar{D}(2310)\bar{D}^*$ or $\bar{D}^*D_1^{'}$ molecule since both $D_0(2310)$ and $D_1^{'}$ are very broad resonances. Hence Y(4260) can not be a hadronic molecule.

Hybrid charmonium [44].

Naively when one gluon is confined within a hadron bag, its binding energy is around 1.1GeV. Hence the $J^{PC} = 1^{--}$ hybrid charmonium mass may be around 4.2GeV. Recently Kalashnikova and Nefediev [45] using QCD string model calculated the mass and splitting of lowest charmonium hybrid state with a magnetic gluon. They

predict that if the Y(4260) is the lowest charmonium hybrid state $c\bar{c}g$, three J^{-+} hybrid charmonia should reside not very far from it. This model can explain very well the non-existence of decay to $D^{(*)}\bar{D}^{(*)}$ since they are forbidden by some selection rules. About the possible decay modes of the hybrid charmonium there is not much discussion in the charmonium literature. Physically these decays may occur via the following process: $J/\psi\pi^0\pi^0$, $\eta\eta J/\psi$. The decay modes: Y(4260) $\rightarrow \omega + \chi_{c0,c1,c2}$, $\rightarrow 3\pi + \chi_{c0,c1,c2}$ may be important if Y(4260) is really a hybrid meson.

Four quark interpretation of Y(4260) [46].

One of the first possible theoretical interpretation proposed soon after its discovery is that the Y(4260) is the first orbital excitation of a diquark-antidiquark state ($[cs][\bar{c}\bar{s}]$). A crucial prediction of this model is that the Y(4260) should decay predominantly to $D_s\bar{D}_s$, and it should also be seen in non leptonic B decays in association with one kaon.
If we assume that the decay of the Y(4260) proceeds through to an $f^0(980)$ which fits the $([sq][\bar{s}\ barq])_{S-wave}$ hypothesis [47] this suggests a $([cs][\bar{c}\bar{s}])$ composition for the Y(4260). All considered, we are led to the following assumption:

$$Y(4260) = ([cs]_{S=0}[\bar{c}\bar{s}]_{S=0})_{P-wave} \tag{2.2}$$

with both diquark state in a $\bar{\mathbf{3}}$ color state. In addition we expect diquarks involving charmed quarks to be bound also in states with non vanishing spin [48]. Thus, several other states with $J^{PC} = 1^{--}$ are possible and one would expect the physical Y(4260) to be a linear super position of all such states. The state in equation 2.2 is supposedly the lowest lying among them. Given the quantum numbers $J^{PC} = 1^{--}$, the state in equation 2.2 should decay strongly into a pair of mesons to open charm. The quark composition in equation 2.2 implies a definite preference for charm-stranges states:

$$\Gamma_{Y(4260)}(D_s\bar{D}_s) \gg \Gamma_{Y(4260)}(D\bar{D}) \tag{2.3}$$

Quark diagram corresponding to $D_s\bar{D}_s$ and to the $J/\psi f_0(980)$ decays in Fig. 2.10.

The Y(4260) should also be seen in B^- and B^0 weak non-leptonic decay, see the quarks diagram in Fig. 2.11 with:

$$\Gamma(B^0 \rightarrow YK_s) = \frac{1}{2}\Gamma(B^- \rightarrow YK^-) \tag{2.4}$$

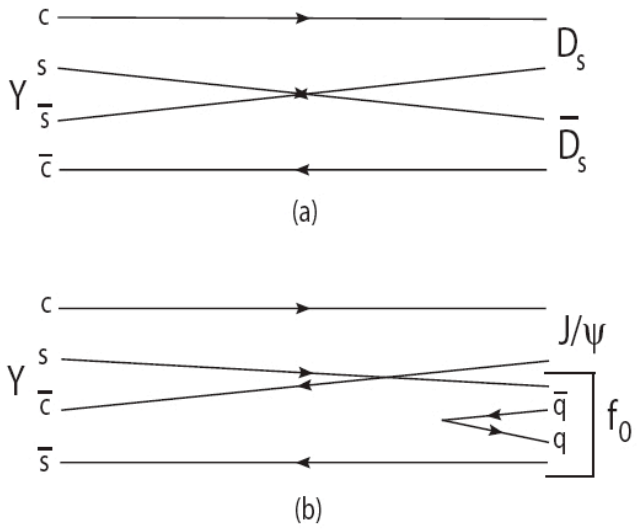

Figure 2.10: (a)Quark diagram for the dominant decay channel to $D_s\bar{D}_s$. (b) Decay amplitude for $Y \to J/\psi f_0(980)$ under the assumption that both Y and f_0 are four-quark state.

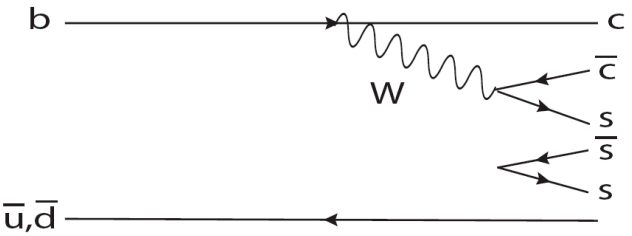

Figure 2.11: (a)Quark diagram for the weak decay of a $B^{-,0}$ meson into YK^- and YK_s. Kaons can be obtained in two independent way by combining the spectator antiquark with a strange quark from the weak vertex or from the sea pair.

Baryonium [49].

An extended baryonium picture can be built to classify the new "charmonium" like states $Y(4260)$, $Y(4320)$, $Y(4660)$ and $Z^{\pm}(4430)$ [50] All these resonances are hard to be embedded into the regular charmonium spectroscopy. The Y(4260) can be interpreted as a $(\Lambda_c - \bar{\Lambda}_c)$ structure [51]. If we extend this baryonium picture to include Σ_c^0 as a basic ingredient, the Λ_c and Σ_c^0 can be taken as basis vector in two-dimensional space, which is similar to the proton and neutron in constructing the pion by Fermi and Yang more than fifty years ago [52]. Approximately, assuming that the transformation in this two-dimensional "C-spin" space is invariant, i.e., there exists a SU(2) symmetry between Λ_c and Σ_c^0. Then, from this doublet one can make up four baryon- antibaryon configurations, the "C-spin" triplet and siglet. As shown in the table 2.2. This is just an imitation of the isospin for proton and neutron system.

Table 2.2: The experimental measurements and baryonium model predictions (speculations) for spin triplet states B and their radial excitations B^*. The question mark means unobserved in experiment, and the pseudoscalar partners of the listed states are all missing. The number in the brackets are in the units of MeV

	triplet	triplet	triplet	singlet
B	$Z_1^+(4330?)$	$Y(4260)$	$Z_1^-(4330?)$	$Y(4560?)$
B^* (radial excitation of B)	$Z_1^{+*}(4430)$	$Y(4360)$	$Z_1^{-*}(4430)$	$Y(4660)$

It is known that the $Y(4320)$ and $Y(4660)$ were observed in $e^+e^- \to \Gamma_{ISR}$ $\psi(2S)\pi^+\pi^-$ but there are no similar structures in $J/\psi\pi^+\pi^-$. One of the possibilities is that these states are the first radial excitation of the heavy hidden quark pair, which may easily decay to $\psi(2S)$ rather that J/ψ . Exsplicity , $Y(4320)$ might be the radial excited state of the $Y(4260)$ and $Y(4664)$ the radial excited state of the C-spin singlet see table 2.2.

To summarize in this extended baryonium picture four classes of baryonium states are predicted, three in triplet and one in singlet. This model predict two vector-like structures one around 4560 MeV (neutral) and one around 4330MeV (charged).

Chapter 3

The *BABAR* experiment

3.1 Introduction

The *BABAR* detector was designed to study the CP-violation, together with the study of several B and D meson decays. B factories are designed to produce copious number of B meson in the pursuit of this quest. The cross section of $e^+e^- \to c\bar{c}$ events is of the same order of magnitude as the one of $e^+e^- \to b\bar{b}$ events. Therefore, high statistics charmed mesons and baryons are expected. The B factory, located at Stanford Linear Accelerator Center in Menlo Park, CA, comprising the PEP-II accelerator complex [53] will be described here.
In order to produced the hundreds of millions of B mesons necessary to study CP-sensitive rare decays, the B mesons must be produced at high luminosity in a relatively clean environment. To this end, the SLAC B factory studies electron-positron collisions at a center-of-mass (C.M.) energy of 10.58 GeV. This energy corresponds to the mass of the $\Upsilon(4S)$ resonance, which is a spin-1 bound state of a b quark and a b antiquark (a member of the "bottomonium" family of mesons). The $\Upsilon(4S)$ mass is just above the $B\bar{B}$ production threshold, and this resonance decays almost exclusively through the strong interaction to approximately equal numbers of $B^0\bar{B}^0$and $B^+\bar{B}^-$ pairs. (The two branching fractions are measured to be equal to high precision [54]

Furthermore, at this energy approximately 20% of the hadronic e^+e^- cross-section is $b\bar{b}$ production (almost exclusively through the $\Upsilon(4S)$), resulting in a clean environment (Table 3.1). A typical $\Upsilon(4S) \to B\bar{B}$ events has on average ten charged particles and twenty photons, as compared with hundreds of charged particles in events recorded at hadronic colliders, which can also be used to study b-hadron decays.

Table 3.1: Production cross-sections at $\sqrt{s}$=M($\Upsilon(4S)$)

$e^+e^- \rightarrow$	Cross-section (nb)
$b\bar{b}$	1.10
$c\bar{c}$	1.30
$s\bar{s}$	0.35
$u\bar{u}$	1.39
$d\bar{d}$	0.35
$\tau^+\tau^-$	0.94
$\mu^+\mu^-$	1.16
e^+e^-	≈ 40

As B mesons are pseudoscalars, the $B\bar{B}$ pair from the $\Upsilon(4S)$ decay evolves in a coherent p-wave and the two mesons have opposite flavor before one of them decays, in accordance with bose statistics. Thus, the experimenter can infer the flavor of a reconstructed B candidate (B_{rec}) from the flavor of the other B in the $\Upsilon(4S)$ event (B_{tag}) at the time of its decay. This can be done through charge correlations of the B_{tag} daughters without fully reconstructing its decay. Such flavor "tagging" of the other B in turn allows the measurement of time-dependent CP asymmetries in reconstructed final states to which both B^0 and $\bar{B}^0$ can decay.[1] The decay rate of B_{rec} is measured as a function of the difference in decay times of the two B's $\Delta t \equiv t_{B_{rec}} - t_{B_{tag}}$.

The Δt difference is calculated from the distance between the decay vertices of the two B mesons. However in $\Upsilon(4S)$ decay the B's are produced almost at rest in the CM frame ($p^*_B = 340 MeV/c, \beta\gamma \approx 0.06$), resulting in a vertex separation of only about 30 $\mu m$by the time they decay. Such a distance cannot be resolved by typical silicon-vertex detectors, which have a spatial vertex resolution of about 50 μm. The B factories solve this problem by colliding electron and positron beams of unequal energies, thus boosting the e^+e^- system in the laboratory frame. PEP-II collides a 8.9 GeV electron beam with a 3.1 GeV positron beam, with a boost of $\beta\gamma = 0.56$. The resulting Lorentz time dilation of the B-meson lifetime elongates the average decay-vertex separation in the lab frame to about 250 μm in the beam direction, which is well within the resolution reach of silicon-detector tecnology. (The B mesons have negligible displacements in the plane transverse to the beam.) Nevertheless, the detector must have excellent vertex and tracking capabilities to enable

[1]This would be impossible otherwise, as the flavor of the reconstructed B cannot be inferred from its final-state daughters in this case.

this measurement and must accomodate the asymmetric nature of the collisions. The *BABAR* detector and PEP-II accelerator will be described more in detail.

3.2 The PEP-II Asymmetric Collider

The PEP-II B factory is part of the accelerator complex at SLAC, show in Fig 3.1. The electron beam is produced by the electron gun near the beginning of the two-mile long linear accelerator (the "linac"). The gun consists of a thermally heated cathode filament held under high voltage. Large numbers of electrons are "boiled off" the cathode, accelerated by the electric field, collected into bunches, and ejected out of the gun into the linac. The electron bunches are accelerated in the linac with synchronized radio-frequency (RF) electromagnetic pulses generated in RF cavities through which the beam passes by a series of 50 Megawatt klystron tubes. (Klystrons generate the pulses with their lower energy electron beams' passing through resonanant cavities). The steering, bending, and focusing of the beam is carried out with magnets throughout the acceleration cycle.

After acceleration to an energy of approximately 1GeV, the electron beam is directed to a damping ring, where the beam is stored for some time. As it circulates in the ring, it loses energy through synchroton radiation and is continuously re-accelerated by RF cavities. The radiation and careful re-acceleration has the effect of reducing the emittance, or spatial and momentum spread of the beam, a necessary step in high-luminosity collisions. The "damped" beam is then re-directed to the linac and accelerated to 8.9GeV.

Half of the generated electron bunches are used for the generation of the positron beam. They are accelerated to approximately 30GeV, extracted from the linac, and directed onto a tungsten target, producing electromagnetic showers that contain a large numbers of electron-positron pairs. The positrons are separated electromagnetically from the electrons, collected into bunches, accelereted, and sent through the return line to the source end of the linac. The positron beam is then accelerated and shaped like the electron beam through the linac and its own damping ring, culminating in an energy of 3.1 GeV. After reaching their respective collision energies, the electron and positron beams are extracted from the linac and directed to the PEP-II storage rings, the High Energy Ring (HER) for electrons and the Low-Energy Ring (LER) for the positrons, both housed in the same tunnel of 2.2 km circumference. As they circulate, they are focused further by a complex of magnets and accelereted by RF cavities to compensate the synchroton-radiation losses. In the

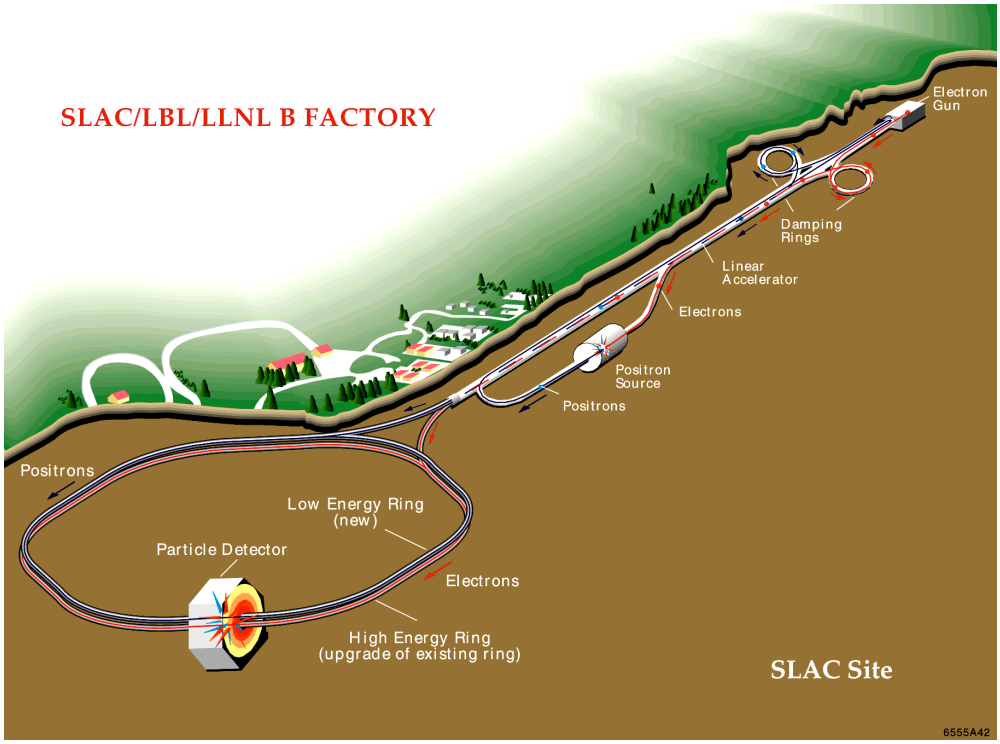

Figure 3.1: A schematic depiction of the B factory accelerator complex at SLAC

interaction region IR-2 (one of the twelve such regions), where the *BABAR* detector is located, they are brought to a collision after a final-focus system squeeze the beams to the smallest possible emittance. During data taking, each ring contains about 1600 circulating bunches colliding every 5 ns. The collisions are then analyzed by the *BABAR* detector . About 10% of the time the beams are collided at an energy 40 MeV below the $\Upsilon(4S)$ resonance for calibration of the backgrounds, as no B mesons are produced then since this energy is below the $B\bar{B}$ threshold. As data is collected, the collisions and other losses reduce the currents in the rings, necessitating re-injection of electron and positron bunches. Initially in the life of the B factory from 1999-2002, data was taken for about an hour or two while the currents diminished, and then additional current was injected into the rings for a few minutes. Data could not be taken during the injection due to the large backgrounds in the detector and the resulting danger to instrumentation. (The detector would have to be put into a "safe" but non-operational state during injection, with, for example, all high-voltage components ramped down to a lower, safer potential.) Starting in 2003 a new scheme for injection, called "trickle" injection, was developed, wherein new bunches are continuously injected at a rate large enough to replenish beam losses but low enough to not damage the detector. This has allowed more efficient operation of the B-factory with 30% more integrated luminosity for a given highest instantaneous luminosity.

The PEP-II collider was designed for an instantaneous luminosity of $3 \times 10^{33}\ cm^{-2}s^{-1}$, but has reached values of $1.2 \times 10^{34}\ cm^{-2}s^{-1}$ due to improvements in the RF cavities, beam-shaping cavities, and magnet systems. The increased luminosity comes from larger beam currents (up to 3 A in the LER and 2 A in the HER) and a reduced emittance. With these specifications and trickle injection, the machine generated hundreds of pb^{-1} of integrated luminosity daily during normal operations, and has integrated hundred of fb^{-1} throughout its operating lifetime.Figure 3.2 shows the integrated luminosity provided by PEP-II collider in the period October 1999 -April 2008, along with the integrated luminosity recorded by *BABAR* detector, that is 432.89 fb^{-1} collected at the $\Upsilon(4S)$ resonance, plus 53.85 fb^{-1} *off-resonance*, 30.23 fb^{-1} at the $\Upsilon(3S)$ resonance and 14.45 fb^{-1} at the $\Upsilon(2S)$ resonance. This analysis uses the $\Upsilon(4S)$ data sample plus the *off-resonance* data sample.

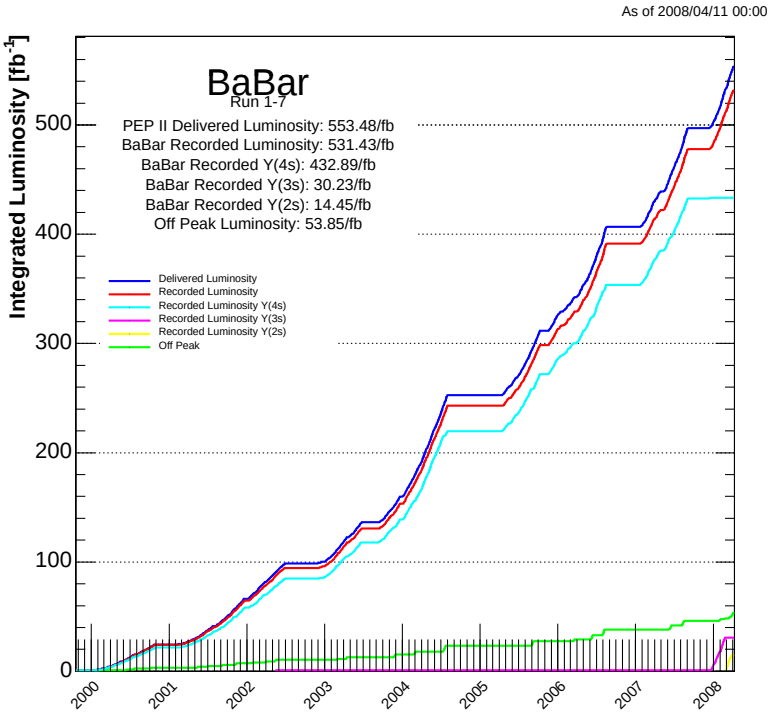

Figure 3.2: Total integrated luminosity delivered by PEP-II and recorded by the *BABAR* detector.

3.3 The *BABAR* detector

In accordance with B-factory-enviroment and program, the detector must satisfy the following requirements:

- Excellent vertex reconstruction in the tracker, in both the parallel and transverse directions to the beam boost;
- Large acceptance, including at small polar angles relative to the boost direction in the lab frame;
- Excellent reconstruction efficiency and good momentum resolution for charged particles and photons from below 100 MeV to 5 GeV;
- Good charged-particle identification to separate lepton, pions and kaon candidates;
- Radiation hardness, particularly for the inner tracking sub-detectors

The *BABAR* detector is a large, multi purpose hermetic detector with several components that together satisfy these requirements [55] As shown in Fig. 3.3 the detector consists of the endcaps and a cylindrical barrel hugging the beam pipe along the z direction and roughly symmetric in the azimuth ϕ. The right-handed coordinate system is defined with the z axis pointing in the e^- direction, x pointing horizontally away from the center of the PEP-II rings, and y pointing upwards. The geometrical center is offset from the beam-beam interaction point towards forward polar angle to maximize the geometric acceptance for the boosted $\Upsilon(4S)$ decays.
The sub-detectors are arranged in layers of increasing distance from the beampipe. The silicon vertex tracker (SVT), the innermost detector, is used for vertexing particle decays and is the main source of information on the polar angle of charged particles. The drift chamber (DCH) is the main device for measuring charged-particle momenta with good resolution through gaseous wire-chamber technology. A Detector of Internally Reflected Cherenkov Light (DIRC) is used to separate pions from kaons, while a crystal Electromagnetic Calorimeter (EMC) is used for energy measurement of photons and electrons and for electron identification. These components are placed within a 1.5 Tesla solenoidal magnet that provides the magnetic bending of charged particles needed to measure their momenta. Outside the magnet is the Instrumented Flux Return (IFR), which is used for the identification of muons

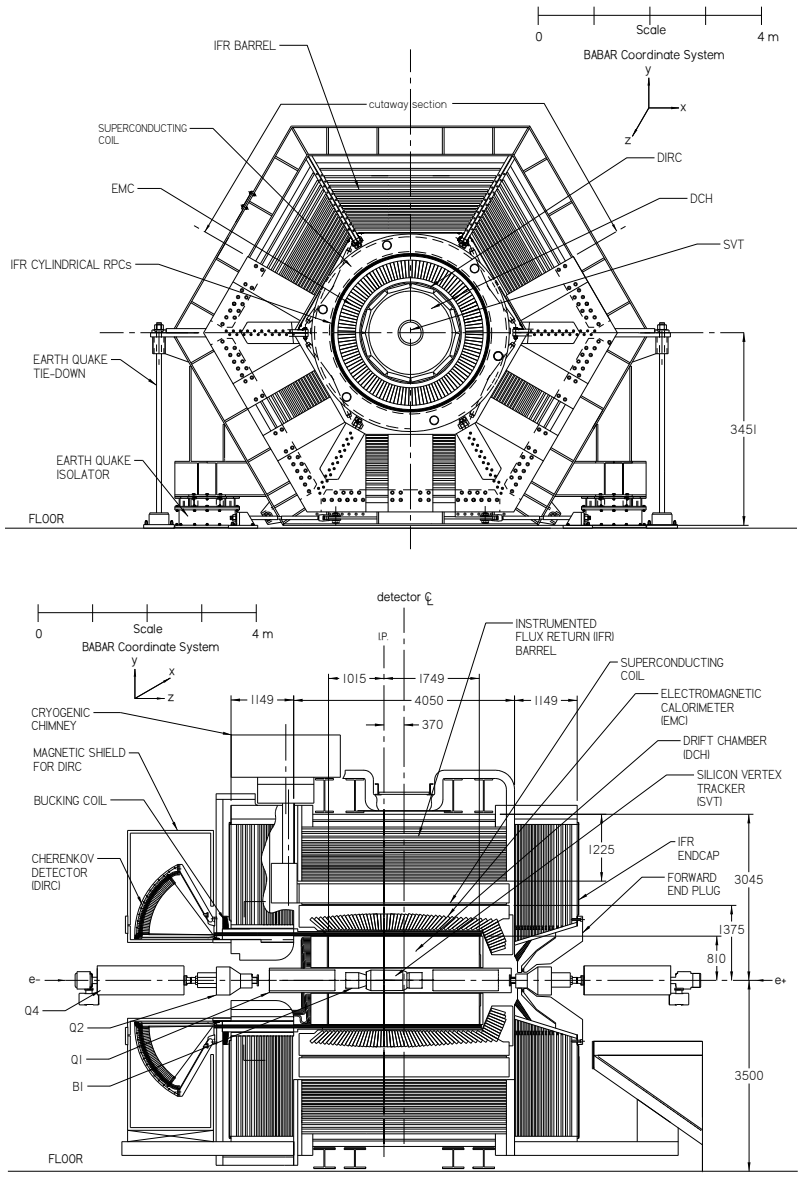

Figure 3.3: Longitudinal cross section of the *BABAR* detector (top) and transverse cross-section of the barrel of the *BABAR* detector (bottom).

and long-lived neutral hadrons. The detector signals are processed through detector electronics, and examined by a trigger system that selects physically interesting collisions data to be stored. Various online and offline reconstruction procedure are employed to convert the data into a format amenable to analysis for the study of relevant B decays and other process.

3.3.1 The Silicon Vertex Tracker

The SVT consists of five layers of double-sided silicon sensors segmented in both the z and ϕ directions, designed to measure accurately the positions and decay vertices of B mesons and other particle 3.4. This measurement is most accurate at small distances from the interaction, as the trajectory

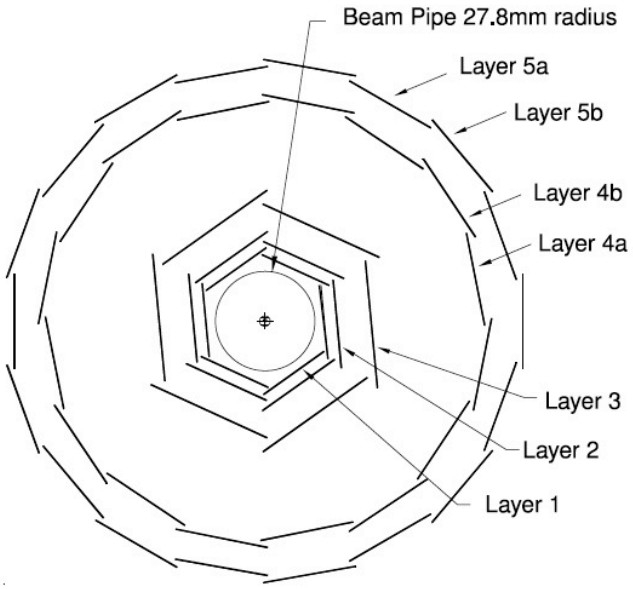

Figure 3.4: Transverse cross section of the SVT.

. of the particles farther away is affected by multiple scattering within the detector. Thus, the first three layers are located as close to the beam pipe as possible. The outer two layers are closer to the drift chamber to facilitate matching SVT tracks with DCH tracks. They also provide pattern recognition in track reconstruction, and the only tracking information for charged particle with transverse momenta below 120MeV/c, as these may not reach the drift chamber.

The SVT covers 90% of the solid angle in the CM frame (Fig3.5).

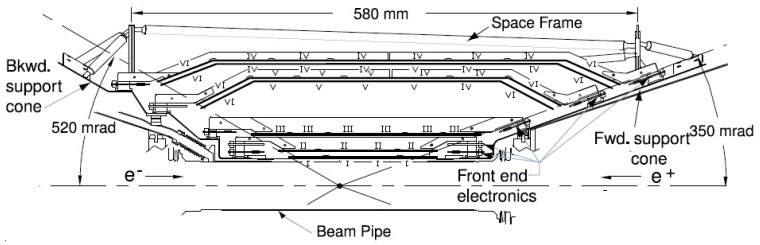

Figure 3.5: Side view of the SVT.

The silicon sensors are $300\mu m$-thick-high-resistivity n-type silicon wafers, with n^+ and p^+ strips running orthogonally on opposite sides. As high-energy particles pass through the sensors they displace orbital electrons, producing conducting electrons and positive holes that then migrate under the influence of an applied depletion voltage. The resulting electrical signal is read- off from the strips, amplified, and discriminated with respect to a signal threshold by front-end electronics. The time over threshold of the signal is related to the charge of the signal and is read out by the data acquisition system for triggered events. The position resolution is in the $10\ \mu m - 50\mu m$ range, depending on the orientation of the strip (ϕ or z) and the layer number.
The SVT is water-cooled and monitored for temperature, humidity, and position variations. Local and global position alignment is performed frequently in the online reconstruction software. As the SVT has to withstand a lifetime integrated radiation dose of 2 Mrad, the sensors have a high threshold for radiation damage. Nevertheless, they are easily damaged by high instantaneous or integrated doses, and an extensive system of radiation monitoring with PIN and diamond diodes can abort the beams if dangerous background levels develop. Up to 2007 the monitoring systems have prevented any significant damage from occurring and the SVT has performed extremely well, with an average track reconstruction efficiency of 97% (Fig 3.6).

3.3.2 Drift Chamber

The Drift Chamber (DCH), a gaseous wire detector, is the main tracking device on the *BABAR* detector. It is used for the measurement of the momenta of charged

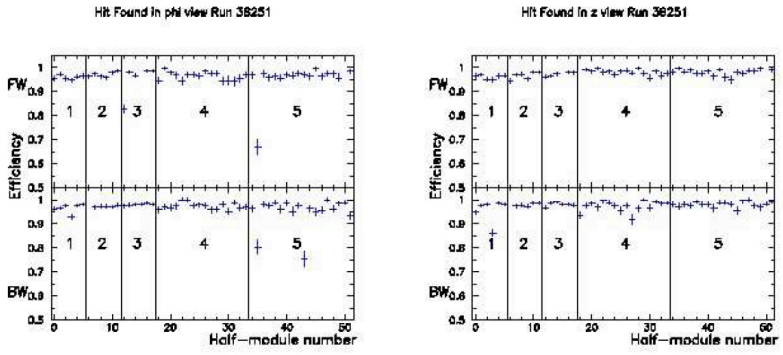

Figure 3.6: SVT reconstruction efficiency in the ϕ view (left) and the z view (right) as measured in $e^+e^- \to \mu^+\mu^-$.

particles, as well as it is the only tracker for the subset of long-lived particles such as K^0, that decay outside of the SVT. In addition, the DCH provides particle-identification capability by measuring track ionization losses as a function of position (dE/dx), particularly for tracks with momenta less than 700 MeV/c. The inner wall of the drift chamber is placed close to the SVT outer wall to facilitate track-matching between the two devices.

The specific requirements for the drift chamber, which operates in a 1.5 T magnetic field, are to provide a spatial resolution better then 140 μm averaged over the cell and to supply identification for low momentum tracks through dE/dx with a resolution of 7% (40 measurements). In addition the drift chamber provides one of the principal triggers for the experiment. These requirements are met through the use of a small-cell design, low density gas and light materials. The choice of the gas mixture (mixture of 80% helium and 20% isobutane) is motivated by considerations of aging and avalanche size as well as minimizing multiple scattering in the chamber, which is accomplished by choosing helium as the primary gas component and aluminum as the lightweight material for the multiple field wires. A schematic side view of the BaBar drift chamber is shown in figure 3.7.

The *BABAR* drift chamber is a 280 cm long cylinder, with an inner radius of 23.6 cm and an outer radius of 81 cm. Since the *BABAR* events will be boosted in the forward direction, the design of the detector is optimized to reduce the material in the forward end. The forward end-plate is therefore made thinner in the acceptance region of the detector (12 mm thick) compared to the rear end-plate (24 mm thick), and all the electronics is mounted on the rear end-plate.

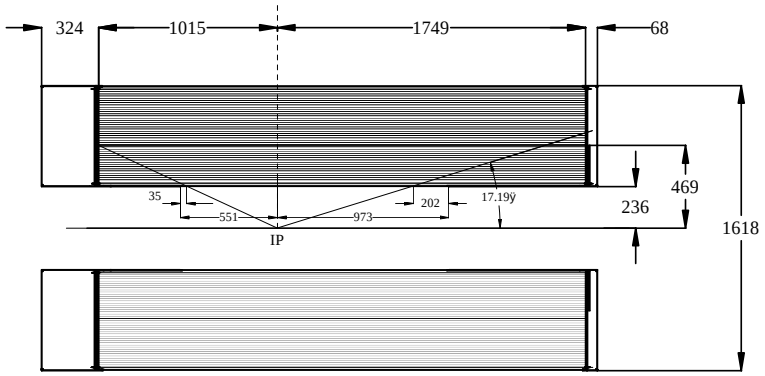

Figure 3.7: Side view of the BaBar drift chamber. The dimensions are expressed in mm.

The cells are arranged in 10 super-layers of 4 layers each, for a total of 40 layers. Axial (A) and stereo (U, V) super-layers are alternated following the pattern AUVAUVAUVA as shown in figure 3.8. The stereo angle varies from a minimum of 40 mrad in the innermost stereo super-layer, to a maximum of 70 mrad in the outermost stereo super-layer.

The field wires are grounded, while the sense wire is held at high voltage, typically around 1900 V. The space around the wires is filled with the gas mixture. High-energy particles ionize the gas as they traverse it, and the liberated electrons are then accelerated toward the sense wires, ionizing additional electrons, which are in turn accelerated themselves and result in the formation of a gas avalanche of electric charge. The avalanche collects on the sense wire with drift times of 10-500 ns and the charge and timing information of the signal is read-off through electronic circuits AC-coupled to the wire. The gain relative to the charge of the primary ionization is about 5×10^4. The grounded field wires produce a uniform electric field in the cell with evenly distributed isochrones, or contours of equal drift time.

The 7104 cells are hexagonal with typical dimension 1.2×1.8 cm^2. Figure 3.8 shows the 50 ns isochrones in a typical cell in a 1.5 T magnetic field.

The DCH has demonstrated excellent performance throughout the life of BABAR with track-reconstruction efficiencies at the 95% level. This includes the effect of disconnecting a fraction of the wires in superlayers 5 and 6 that were damaged during the commissioning phase. The dE/dx response, with a resolution of about 7%, is shown in Figure 3.9, and a new calibration in 2006 has improved the PID potential of this capability for high-energy tracks. The achieved resolution on transverse

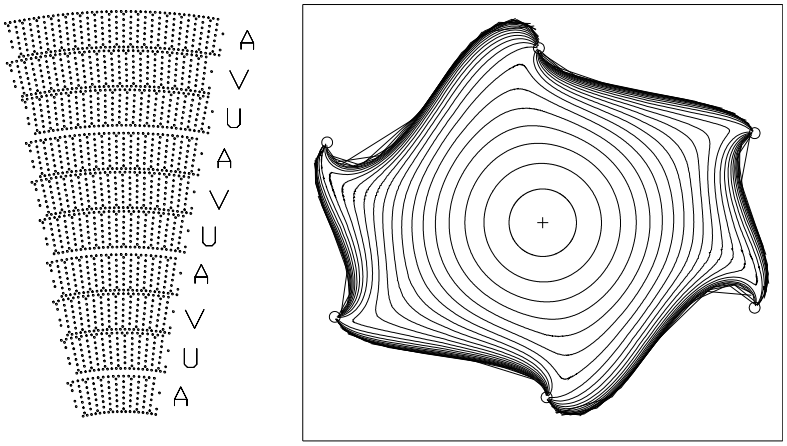

(a) (b)

Figure 3.8: (a) Cell layout in the BaBar Drift Chamber; (b) 50 ns isochrones in a typical BaBar drift chamber cell.

momentum is $\sigma_{p_t}/p_t = (0.13 \pm 0.01)\% \dot{p}_t + (0 : 45 \pm 0 : 03)\%$, where p_t is given in units of GeV/c.

3.3.3 Cherenkov detector

Since the inner drift chamber tracker can provide sufficient $\pi - K$ separation up to only about 700 MeV/c, the dedicated Particle Identification (PID) system must perform well over a range from about 0.7 to 4.2 GeV/c, where the challenging upper end of this range must be achieved in the forward region of *BABAR* . *BABAR* has therefore a dedicated PID subdetector: the $DIRC$ (Detector of Internally Reflection Cherenkov light) [56].

The phenomenon of the Cherenkov light emission is widely used in particle detectors technology. A charged particle traversing a medium with a velocity of β greater than the speed of light in that medium - that is $\beta > 1/n$, where n is the medium refraction index - emits directional electromagnetic radiation, called Cherenkov light. The angle of emission θ_C of the photons with respect to the track direction is called Cherenkov angle and is determined by the velocity of the particle with the relation

$$cos\theta_C = \frac{1}{n\beta} \tag{3.1}$$

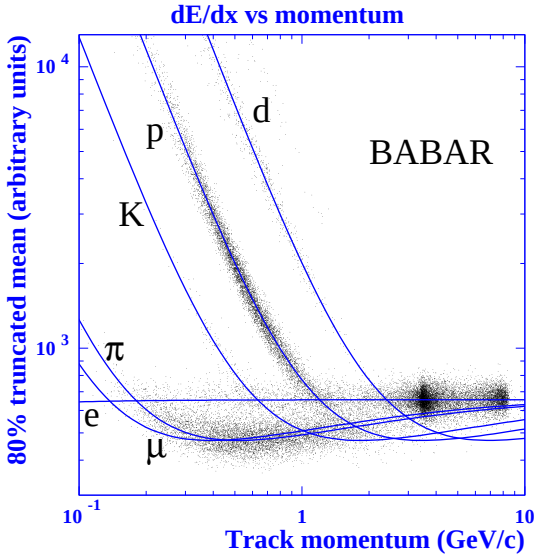

Figure 3.9: 50 ns isochrones in a typical BaBar drift chamber cell.

where $\beta = \frac{v}{c}$ is the particle velocity, and c the light velocity.

Thus, the measurement of θ_C determines β and, given the momentum of the particle, already measured in the DCH, the mass of the particle can be obtained. In fact, the $DIRC$ is placed between the charged particle tracking detectors (Drift Chamber) and the electromagnetic calorimeter. In order to minimize the worsening of the energy resolution and volume, and hence cost, of the electromagnetic calorimeter, the $DIRC$ has been designed to be thin and uniform in terms of radiation lengths. Moreover, for operation at high luminosity, it needs fast signal response, and should be able to tolerate high background.

In figure 3.10 a schematic view of DIRC geometry and basic principles of Cheerenkov light production, transport and image reconstruction.

The DIRC inverts the traditional concept of ring-imaging Cherenkov counters (RICH) in that it relies on the detection of Cherenkov photons trapped in the radiator due to total internal reflection. The DIRC radiator consists of 144 long, straight bars of synthetic quartz with rectangular section, arranged in a 12-sided polygonal barrel. The bars have transverse dimensions of 1.7 cm thick by 3.5 cm wide, and are 4.9 m long (see figure 3.11). The DIRC radiator extends through the steel of the solenoid flux return in the backward direction, to bring the Cherenkov light, through successive total internal reflections, outside the tracking and magnetic volumes. Only this end of the bars is instrumented. A mirror placed at the other end

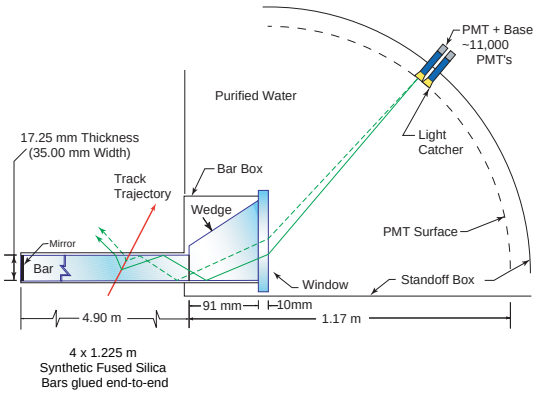

Figure 3.10: Schema of the DIRC working principle.

on each bar reflects forward-going photons to the instrumented end. The Cherenkov angle at which a photon was produced is preserved in the propagation, modulo a certain number of discrete ambiguities, some of which can be resolved by the photon arrival-time measurement. Remaining ambiguities are dealt with by the pattern recognition during Cherenkov angle reconstruction.

The radiator material used for the bars is synthetic fused silica (n = 1.474): the bars serve both as radiators and as light pipes for the portion of the light trapped in the radiator by total internal reflection. Synthetic silica has been chosen because of its resistance to ionizing radiation, its long attenuation length, its large index of refraction, its low chromatic dispersion within its wavelength acceptance.

At the instrumented end, the Cherenkov image is allowed to expand. The expansion medium is purified water, whose refractive index matches reasonably well that of the bars, thus minimizing the total internal reflection at the quartz-water interface. The region containing water is called the Standoff Box. Cherenkov photons are detected in the visible and near-UV range by a close-packed array of linear focused 2.82 cm diameter photomultiplier tubes (PMTs), lying on an approximately toroidal surface. A small piece of quartz with a trapezoidal profile glued at the back end of each bar allows for significant reduction in the area requiring instrumentation because it folds one half of the image onto the other half, while also reflecting photons with large angles in the radial direction back into the detection array. The dimensions of the Standoff Box are such that geometrical errors on angle measurements due to the finite size of bars and PMTs are of the order of the irreducible error due to quartz achromaticity. Six m^3 of water are needed to fill the Standoff Box, and about 11,000 PMTs to cover the detection area. The PMTs are operated

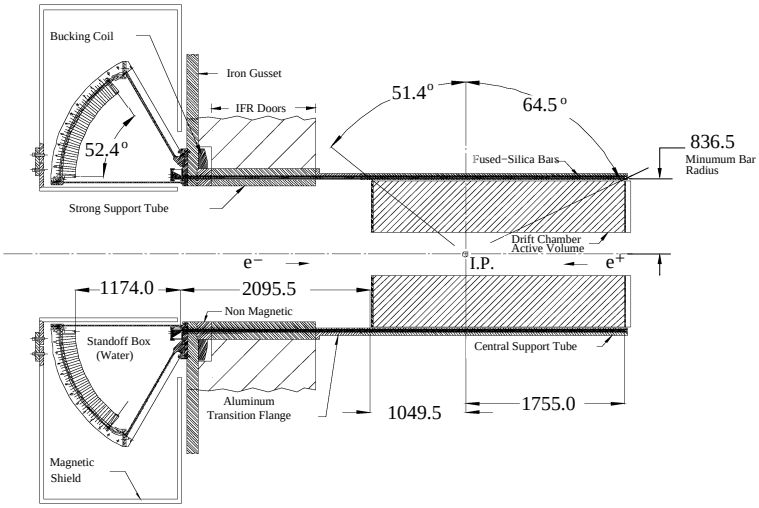

Figure 3.11: Elevation view of the nominal DIRC system geometry. All dimensions are given in millimeters.

directly in water, and are equipped with light concentrators. The PMTs are about 1.2 m away from the end of the quartz bar. Magnetic shielding around the Standoff Box is further needed to maintain the magnetic fringe field at an acceptable level for PMT operation.

The DIRC is intrinsically a three-dimensional imaging device, giving the position and arrival time of the PMT signals. The three-dimensional vector pointing from the center of the bar end to the center of the PMT is computed, and then is extrapolated (using Snell's law) into the radiator bar in order to extract, given the direction of the charged particle, the Cherenkov angle. Timing information is used to suppress background hits and to correctly identify the track emitting the photons.

The discrimination between π and K due to the separation between the corresponding Cherenkov angles is greater then 3 standard deviation at about 3 GeV, as shown in figure 3.12, and higher for lower momenta. Due to the fact that the photons inside the quartz are totally reflected, the association between phototube hits and single track can have more than one solution. These possible ambiguities are solved by measuring the time difference between the hits in phototubes and the expected arrival time of each track with a precision of 1.7 ns, which allows to estimate the propagation time for a given Cherenkov angle, and therefore to reduce the background from uncorrelated photons.

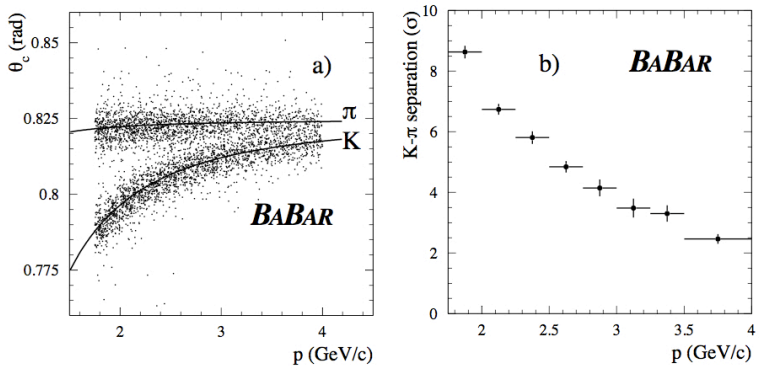

Figure 3.12: (a) Cherenkov angle and (b) K - π discrimination power as a function of the momentum for single tracks. Discrimination quoted is computed performing the mean over all the polar angles.

3.3.4 Electromagnetic calorimeter

The electromagnetic calorimeter (EMC) [57] is designed to measure electromagnetic showers with excellent efficiency, energy and angular resolution over the energy range from 20 MeV to 9 GeV.

This functionality is necessary to reconstruct π^0 and η^0 mesons that decay to two photons, as well as for identification of high-energy photons from rare radiative B decays. The electron ID is necessary for J/ψ reconstruction, for tagging the flavor of the non-signal B in the event through semileptonic decays, as well as for reconstruction of semileptonic and rare B decays. The detector must be hermetic and operate within the 1.5 Tesla magnetic field. The amount of material in front of the EMC has been kept to a minimum in the design of the*BABAR* detector in order to allow for the detection of photons and electrons down to energies of 20 MeV.

The EMC is composed of 6580 Thallium-doped Cesium iodide (CsI(Tl)) scintillating crystals (Fig. 3.13), separated into a cylindrical barrel of 48 rings and a forward endcap of eight rings (Fig. 3.14). The EMC covers 90% of the CM acceptance and does not contain a backward endcap as the CM acceptance is low at backward polar angles. CsI(Tl) was chosen for its high light yield of 50,000 γ/MeV, allowing for excellent energy resolution, and its small Molière radius of 3.8 cm[2],

[2]The Molière radius is the intrinsic limit of the position resolution of electromagnetic showers in a crystal.

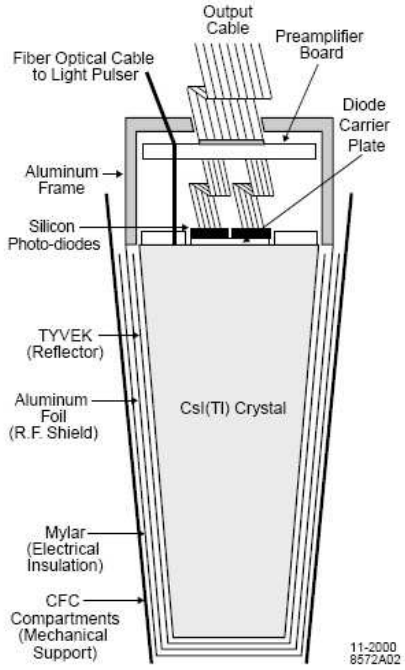

Figure 3.13: Schematic view of the CsI(Tl) crystal with the front-end readout package mounted on the rear face (not to scale).

which allows e for excellent angular resolution. The transverse segmentation is at the scale of the Molière radius in order to optimize the angular resolution while limiting the number of crystals and readout channels.

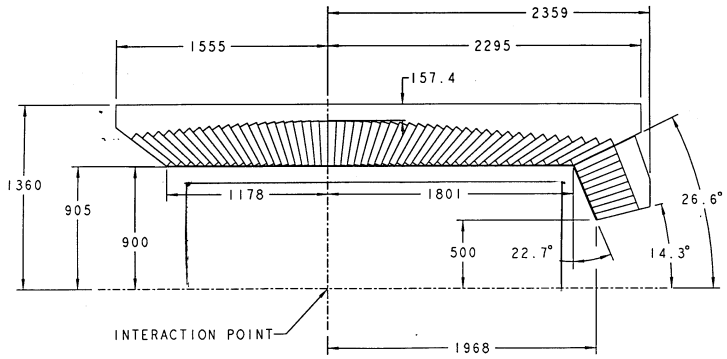

Figure 3.14: Side view showing dimensions (in mm) of the calorimeter barrel and forward endcap.

The crystals serve as radiators for the traversing electrons and photons, with a short radiation length of 1.85 cm. The crystals scintillate under the influence of the showers, and the light is then passed through total internal reflection to the outer face of the crystal, where it is read out by silicon PIN diodes. As these diodes are well suited for operation in the high magnetic fields in the EMC, part of the motivation for the crystal choice was that the frequency spectrum of CsI(Tl) is detected by silicon PIN sensors with the high quantum efficiency of 85%. The EMC is cooled by water and Fluorinert coolant and monitored for changes in the environmental and radiation conditions and for changes in the light response of individual crystals.

The energy response of the EMC is calibrated using low-energy photons from a radioactive source and high-energy photons from radiative e^+e^- Bhabha events. As electromagnetic showers spread throughout several crystals, a reconstruction algorithm is used to associate activated crystals into clusters and either to identify them as photon candidates or to match individual maxima of deposited energy to extrapolated tracks from the DCH-SVT tracker. Additional PID is obtained from the spatial shape of the shower.

The designed energy resolution for EMC is given by:

$$\frac{\sigma(E)}{E(GeV)} = \frac{\sigma_1}{(E(GeV))^{1/4}} + \sigma_2 \tag{3.2}$$

where the expected $\sigma_1 \sim 1\%$ and $\sigma_2 \sim 1.2\%$ result to be higher when fitting the results from different methods of calibration as shown in Fig., in fact they result to be: $\sigma_1 = (2.32 \pm 0.03)\%$ and $\sigma_2 = (1.850.07)\%$. These differences come from cross talk effects on the electronic readout. As it is possible to see from Fig. 3.15(a), the energy resolution ranges between 2% and 6%. The designed angular resolution is:

$$\frac{\sigma_{\theta,\phi}}{E(GeV)} = \frac{\sigma_1}{\sqrt{E(GeV)}} + \sigma_2 \tag{3.3}$$

ranging between 3 and 10 mrad (Fig. 3.15(b)).

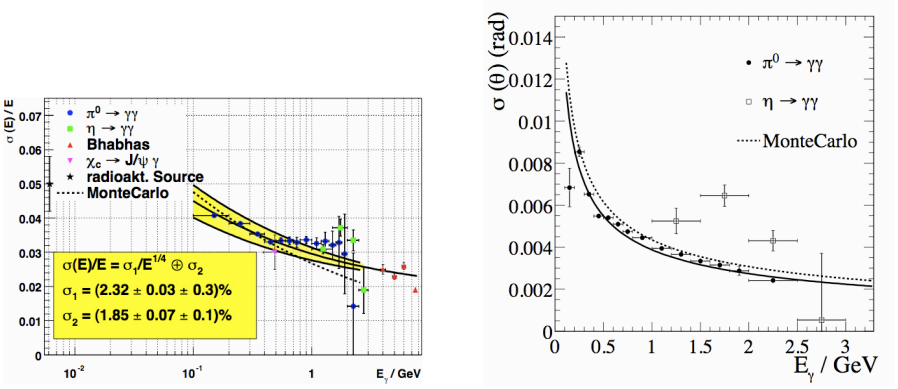

(a) (b)

Figure 3.15: (a) Energy resolution versus energy photon for different calibrations. (b) Angular resolution versus energy photon.

3.3.5 The Instrumented Flux Return

The IFR is the primary muon detector at *BABAR* and is also used for the identification of long-lived neutral hadrons (primarily K_L^0's). The IFR is divided into a hexagonal barrel, which covers 50% of the solid-angle in the CM frame, and two endcaps (Fig. 3.16). Originally, it consisted of layers of steel of varying thickness interspersed with Resistive Plate Chambers (RPCs), 19 layers in the barrel and 18 in each endcap. The steel serves as a flux return for the soledail magnet as well as an hadron absorber, limiting pion contamination in muon ID. RPC's were chosen as they were believed to be a reliable, inexpensive option to cover the $2000m^2$ of instrumented area in this outermost region of *BABAR* with the desired acceptance,

efficiency, and background rejection for muons down to momenta of 1GeV/c.

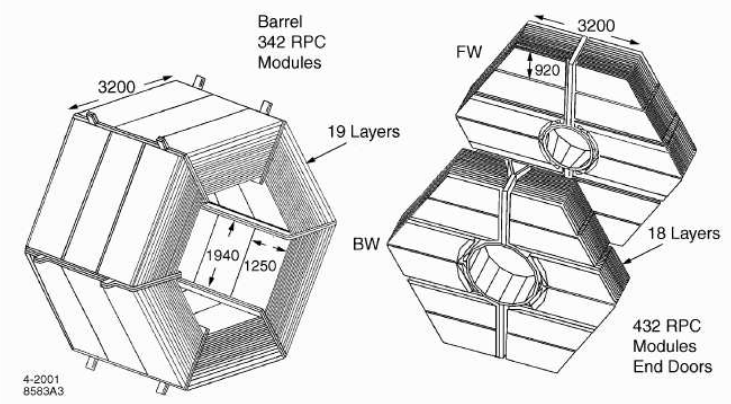

Figure 3.16: Drawing of the IFR barrel and endcaps

The RPC's detect high-energy particles through gas-avalanche formation in a high electric field. The chambers consist of 2mm-thin bakelite sheet kept 2 mm apart by an array of spacers located every 10 cm (Fig 3.17). The space in between is filled with a non-flammable gas mixture of 56.7% argon, 38.8% freon 134a, and 4.5% isobutane, while the sheets are held at a potential of 8000 V. The inside surface of the bakelite is smoothed with a linseed-oil coating so that the electric field is uniform, thus preventing discharges in the gas and large dark currents. The RPC's operate in streamer mode, wherein the avalanche grows into a streamer, a mild, controlled form of electrical discharge in the gas. The streamer change is read out in both the ϕ and z directions by aluminum strips located outside and capacitively coupled to the chamber. The streamer is kept from producing electrical breakdown of the gas by the quenching action of the freon and isobutane molecules. Isobutane has large molecules with rotational degrees of freedom that can absorb electrical energy.

In streamer mode, the gas gain is at the 10^8 level. The factor of 10-1000 increase in gain over avalanche mode greatly simplifies the readout electronics. Moreover, the charge of the streamer is independent of the primary-ionization charge, resulting in an effectively digital signal with high efficiency . Initially, the RPCs performed at over 90% efficiency as expected geometrically from inactive space in the detector,

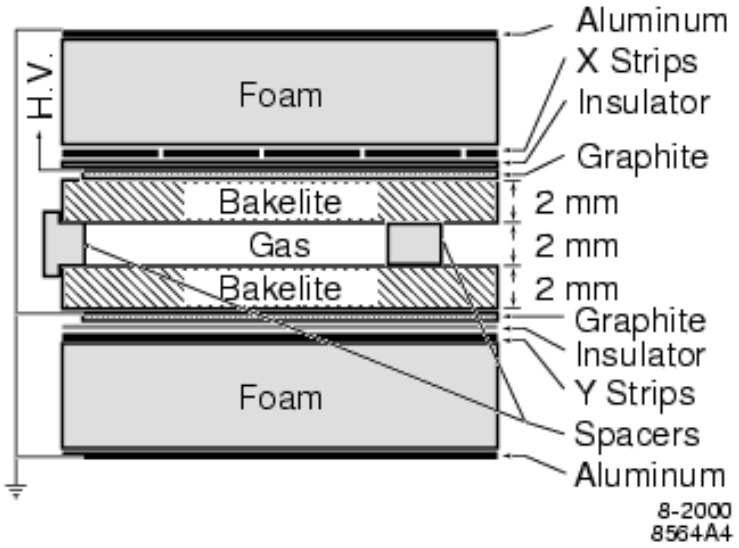

Figure 3.17: Cross section of *BABAR* RPC

resulting in a muon detection efficiency of 90% for a pion misidentification rate of 6-8% in the momentum range of $1.5 < p < 3.0$ GeV/c.
Shortly after the start of data-taking with *BABAR* in 1999, the performance of the RPCs started to deteriorate rapidly. Numerous chambers began drawing dark currents and develop large areas of low efficiency. The overall efficiency of the RPC's started to drop and the number of non-functional chambers (with efficiency less than 10%) rose dramatically (Fig. 3.18), deteriorating muon ID. The problem was traced to insufficient curing on R&D of the linseed-oil-coating and to the high temperature at which the RPC's were operated initially. Uncured oil droplets would form columns under the action of the strong electric field and the high temperature (up to 37 deg C), bridging the bakelite gap and resulting in large currents and dead space (Fig 3.19)

Various remediation measures were attempted, including flowing oxygen through the chambers to cure the oil and introducing water cooling on IFR, but they did not solve the problem. Extrapolating the efficiency trend showed a clear path towards muon ID capability at *BABAR* within a couple of years of operations, so an upgrade of the IFR detector was deemed necessary by the collaboration.

The forward endcap was retrofitted with new improved RPCs in 2002. The new

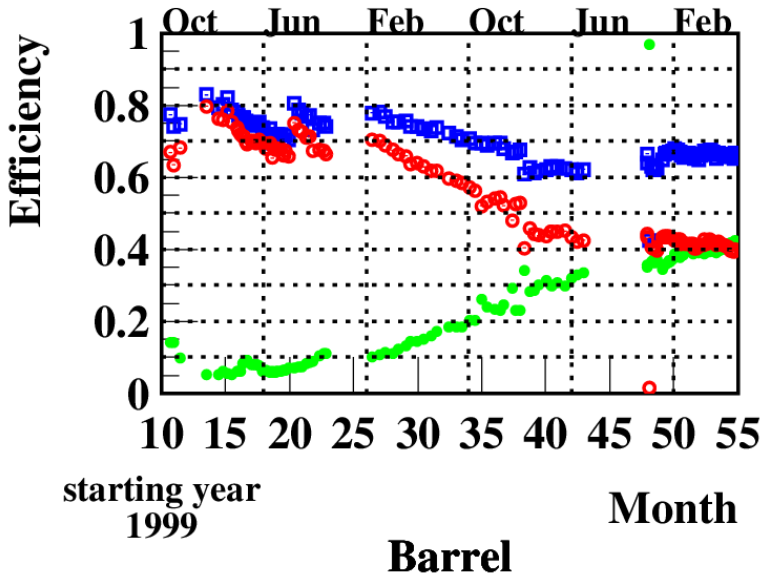

Figure 3.18: Deterioration with time of the average RPC efficiency (red). The green dots show the fraction of RPC's with efficiency lower than 10 %, and the blue dots show the fraction of RPC's with efficiency greater than 10%.

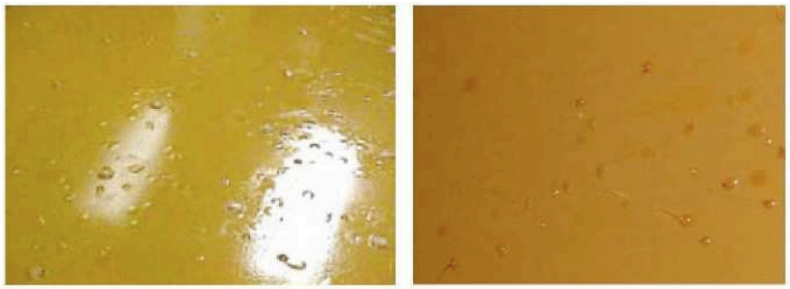

Figure 3.19: Photographs of defects on the linseed oil coating of a malfunctioning RPC.

chambers were screened much more stringently with QC test and had a much thinner linseed-oil coating that was properly cured and tested. They have performed well since then. The backward endcap was not retrofitted, as its acceptance in the CM frame is small. In the barrel, the collaboration decided to upgrade the detector with Limited Streamer Tube (LST) technology. The RPCs were removed and replaced by 12 layers of LSTs and 6 layers of brass to improve hadron absorption. (The last layer of RPCs is inaccessible, so the old chamber there were disconnected from all utilities but kept in place). As the author was heavily involved in this upgrade and as the project was a laborious and careful but time-sensitive project undertaken at a mature age of the experiment, it will be described in more detail than the other components of the detector.
The LST consist of a PVC comb of eight 15mm by 17m cells about 3.5m in length, encase in a PVC sleeve, with a $100\mu m$ gold-plated beryllium-copper wire running down the center of each cell (Fig 3.20). The cells in the comb are covered with graphite, which is grounded, while the wires are held at 5500 V and held in place by wire holders located every 50cm.

Figure 3.20: The mechanical structure of *BABAR* LST.

The gas mixture consist of 3.5 % argon, 8% isobutane, and 88.5 % carbon dioxide. Like the RPCs and as their name implies, the LSTs are operated in streamer mode. The signal is read off directly from the wires through AC-coupled electronics (granularity of two wires per channel in the ϕ direction) and from strips running perpendicular to the tubes and capacitively coupled to the wires (35mm pith in the z direction).

Experience with the RPCs underscored the crucial role of R&D and QC at every level of development of the new technology. Thus, during R&D a stringent QC methodology was developed after the final design of the tubes was chosen. During construction, the mechanical quality of the graphite surface was inspected and the resistivity tested. The chambers were strung with wires tested for thickness and tested for gas leaks after sealing. The tubes were then conditioned under progressively higher applied voltage to burn off any dirt accumulated during construction. Only tubes that could hold the operational voltage without drawing excessive currents were accepted. One of the crucial performance characteristics was the "singles' rate", or counting-rate, plateau. As the streamer signals are effectively digital, given a constant incident flux of particles, the chamber should show a counting-rate plateau over a range of applied voltage where the charge of every streamer is above the read-out threshold (Fig. 3.21).

The plateau provides operational tolerance of the applied HV, allowing operations of the LSTs at the middle of the plateau to safeguard against fluctuations in efficiency due to changes in the gas gain from pressure or voltage fluctuations. Defects in the surface of the graphite or dirt accumulated on the wire can result in large discharges in the tube (including the Malter effect) that raise the singles' rate and spoil the plateau (Fig. 3.21). In addition, a short plateau is an indication of poor aging behavior. Thus, the quality of the plateau is a powerful QC test. [3]

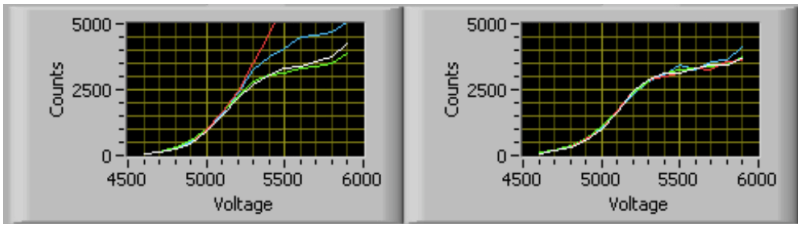

Figure 3.21: A singles' rate plateau seen versus applied voltage for several LST channels (right). Defects in the chamber can spoil the plateau (left)

Another powerful QC procedure is scanning the tube with a localized, focused

[3]The plateau eventually fails at 5900V or higher due to multiple streamers formed from electrons photoelectrically ejected from the graphite by UV photons radiated by the original streamer. At high voltages, enough UV photons are produced to overwhelm any signal dead-time imposed by the electronics, thus raising the singles' rate.

radioactive source, subjecting small regions of the tube to intense radiation rates. Although the incident flux is then much higher than what the tube would experience in the experiment, the stress reveal weak points in the tube, where the source initiates a self-substaining discharge of high current that continues even when the source is removed while the high voltage is applied (Fig 3.22) [4]. Only tubes that do not exhibit this behavior are accepted for installation.

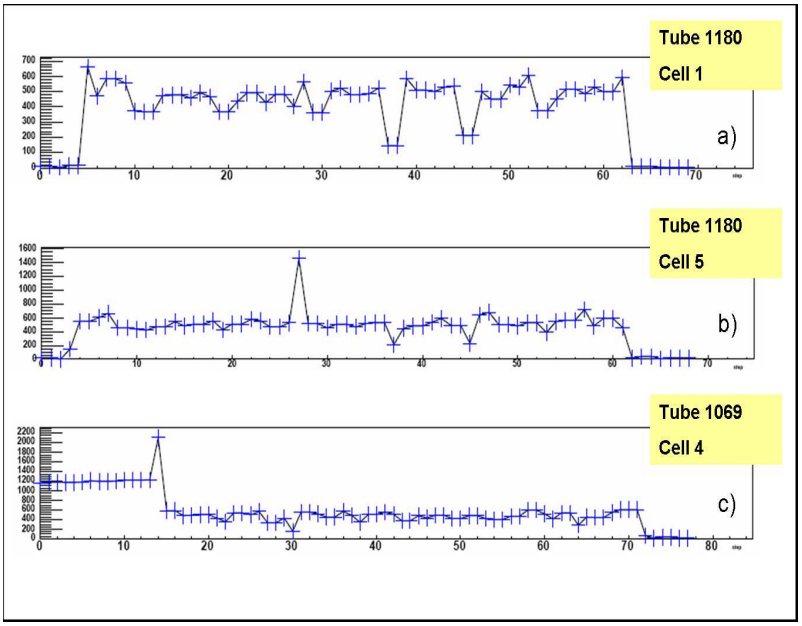

Figure 3.22: Plots of the current drawn by an LST versus position of the source as it scan along the length of the chamber. Channel without any problem (top). Channel with a spike (center). Channel with a self-substaining discharge (bottom)

The LSTs were constructed at PolHiTech, an Italian company that was located in Carsoli, outside of Rome. The construction and QC procedures outlined above were conducted under the supervision of *BABAR* personnel. After all QC tests, the tubes were held under high voltage for a month to verify that no premature aging behavior occurred. Thereafter, they were assembled into modules of two to three tubes at Princeton University an The Ohio State University and then shipped to SLAC for installation, which occurred in two stages: two sextants of hexagonal

[4]This happens when a conductive channel is formed in the gas around a mechanical defect.

barrel in the Summer 2004 and the remaining in the Fall of 2006 [5]. QC procedures were performed at every step to make sure that only the best tubes were installed in the detector.
The project involved the manufacture of 1500 LSTs including contingency, with more than 1200 installed in the detector. It also necessitated the design and fabrication of custom read-out electronics, HV power supplies and gas system. The project was completed successfully, safely, and ahead of schedule. After installation, the tubes have been performed extremely well since 2005 in two sextants and since the beginning of 2007 in all sextants, with failures rates below 0.5% for both the tubes and z-strip. The efficiencies of all layers are at the geometrically expected level of 90%. Regular testing of singles' rates with cosmic rays has verified continuing excellent behavior with long singles'-rate plateau.

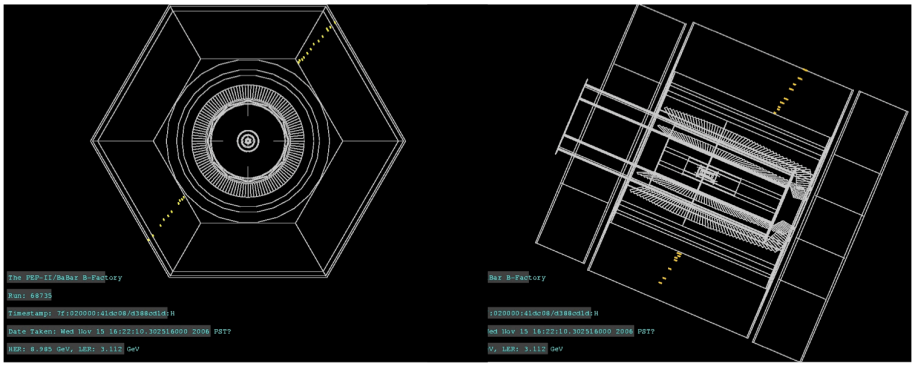

Figure 3.23: Cosmic -ray muon ϕ view (left) and z view (right)

Figure 3.23 shows muon tracks in the LST part of the IFR.

3.3.6 Trigger, Data Acquisition and Reconstruction

Data relevant for B physics is selected for storage from the flow of collision information collected by the detector by a two-level trigger system. The Level 1 (L1) trigger is hardware-based, consisting of several dedicated microprocessor systems that analyze data from the front-end electronics (FEEs) of the DCH, EMC, and IFR to form primitive physics object used to make the trigger decision. These include tracks of minimum transverse momentum that penetrate to a particular depth into the DCH and energy clusters in the EMC above the thresholds. The selection are optimized

[5]The delay of the second phase was due to an electrical accident at SLAC in the Fall of 2004 that shut down the lab for a half of a year.

to maintain nearly $B\bar{B}$ efficiency while removing most of the beam-induced backgrounds in the process of reducing the data collection rate from about 20kHz to a few kHz, which can be processed by the next trigger level. Some "prescaled" events of random bem-beam crossing and special events types are also collected for efficiency, diagnostic, and background studies. The trigger decision is made and communicated within the 12.8 μs buffer limit of the FEEs. The L1 trigger has greater than 99.5% efficiency for $B\bar{B}$processes.

After an L1 accept decision, the L1 output is passed on to the Level3 (L3) trigger, which consists of software-based algorithms run on a farm of commercial PCs.[6] The L3 trigger also has access to the complete event data and refines the L1 decision with more sophisticated selections, such as requirements on a track's distance of closest approach to the interaction point or the total invariant mass of an event. It maintains the $B\bar{B}$ selection efficiency at more than 99% while reducing the data rate to about 200Hz. Each event corresponds to about 30kB of detector information. An event that results in an L3 accept decision is processed by the data-acquisition electronics and event-building software. In this process, charged tracks are reconstructed from DCH and SVT information and extrapolated to the outer part of the detector incorporating knowledge of the distribution of material in the detector and magnetic field. The momenta of tracks is measured from the sagitta in the curves of the tracks [7]. PID is refined with DIRC, EMC, and IFR information as well as with attempts to match objects in those sub-detectors with tracks in the DCH. Fundamental physical objects reconstructed in the detectors are also used to assemble candidates for composite particles, such as π^0's from two photon candidates and K^0_S's from two charged tracks candidates (from the $K^0_S \to \pi^+\pi^-$ process.) List of particle candidates as well as the original digitized data is stored on tape in collections that are retrieved later for high-level analysis by individual groups of users.

Throughout event reconstruction various calibration such as alignment constants and energy-scale adjustments in the EMC are applied to detector information to refine reconstruction performance. Calibration information were updated frequently during data taking to keep it consistent with running conditions. Data-quality

[6]The numbering scheme is historical and based on trigger systems with two-hardaware based levels and a third, software-base level, as commonly implemented in hadron colliders. *BABAR* requires only one hardware-based level, but the first software-based level maintains the tertiary designation.

[7]Charged particles are deflected by the magnetic field of the solenoidal and propagate in helices around the magnetic field lines with the radius of curvature $R \sim p/B$, where p is the momentum of the particle and B is the magnetic field. The orientation of bending depends on the charge of the particle

scripts monitor detector behavior and various physics processes to verify that the collected data was not compromised by deviations from expected behavior of the detector or accelerator. A parallel system based on the EPICS slow-control environment was used to monitor and control the detector elements for all subsystems. Detector, accelerator, and environmental conditions were recorded in another ambient database. The entire data-taking process was supervised at all times by at least two BABAR shifters on the detector side and several accelerator operators on the PEP-II side.

Chapter 4

Study of the $J/\psi\pi^+\pi^-$ final state after ISR

4.1 Event Selection

4.1.1 ISR cross section

The ISR process [58] provides access to e^+e^- annihilations to vector mesons for a continuous spectrum of energies below the nominal beam energy. The corresponding cross section has been studied in reference [59, 60] and is given by:

$$\frac{d\sigma(s,x)}{dx} = W(s,x) \times \sigma_0(s(1-x)), \tag{4.1}$$

where $W(s,x)$ is the photon emission probability density function, and s is the nominal collision energy, $x \equiv 2E_\gamma/\sqrt{s}$, is the photon energy relative to the beam energy in the Center-of-Mass (CM) frame. The Born cross section of a narrow vector resonance V production is given by the standard Breit-Wigner formula

$$\sigma_0(s) = \frac{12\pi\mathcal{B}_{ee}}{m_V^2} \times \frac{m_V^2\Gamma_V^2}{(s-m_V^2)^2 + m_V^2\Gamma_V^2} \tag{4.2}$$

where m_V and Γ_V are the resonance mass and width respectively, $\mathcal{B}_{ee}$ is the branching fraction of $V \to e^+e^-$ decay. For a narrow resonance, the total cross section $\sigma_V(s)$ is found to be

$$\sigma_{\gamma V}(s) = \frac{12\pi^2\,\Gamma_{V\to ee}}{m_V \cdot s}\, W(s,x_V) \tag{4.3}$$

where $x_V = 1 - m_V^2/s$ and $\Gamma_{V\to ee}$ is the partial width of $V \to e^+e^-$. The $W(s,x_V)$ values for the $\psi(2S)$, $\psi(2S)\pi^+\pi^-$ and $X(3872)$ at $\sqrt{s} = 10.58\,GeV$ are listed in Table 4.1.1.

	x_V	$W(s,x_V)^I$	$W(s,x_V)^{II}$	$\Gamma_{V\to ee}(\,\mathrm{keV})$	$\sigma^I_{\gamma V}(pb)$	$\sigma^{II}_{\gamma V}(pb)$
ISR $\psi(2S)$	0.8786	0.0506	0.0543	2.12 ± 0.12	14.0 ± 0.7	14.5 ± 0.7
ISR $\psi(2S)\pi^+\pi^-$	0.8730	0.0510	0.0547	0.26 ± 0.04	1.45 ± 0.22	1.55 ± 0.24
ISR $Y(4260)$	0.8379	0.0537	0.0572			

Table 4.1: The $W(s,x)$ and $\sigma_{\gamma V}(s)$ values for ISR $\psi(2S)$, $\psi(2S)\pi^+\pi^-$ and $X(3872)$. $W(s,x)^I$ and $\sigma_{\gamma V}(s)^I$ are the photon emission probability density and cross section at first order, and $W(s,x)^{II}$ and $\sigma_{\gamma V}(s)^{II}$ are with leading second order corrections.

In principle, only vector charmonium states (such as $^3S_1$ and $^3D_1$) can be directly produced in e^+e^- single virtual photon interactions regardless whether ISR has occurred. Currently all known charmonia with masses above $4\,\mathrm{GeV}/c^2$ such as $\psi(4040$, $\psi(4160)$ and $\psi(4415)$ are vector charmonium states, and have mainly been studied with $R(\sqrt{s})$ (the ratio of the hadronic cross section to the di-muon cross section in e^+e^- annihilations) measurements. Their masses and widths are not well established [61]. The observation of such non-$D\bar{D}$ decay of charmonia above the charm threshold itself is very interesting.

The expected number of observed vector meson produced via ISR is

$$N(\gamma\, V) = \mathcal{L}\cdot W(s,x_V)\,\frac{12\pi^2\,\Gamma_{V\to ee}}{m_V\cdot s}\,\mathcal{B}(V{\to}J/\psi\pi^+\pi^-)\cdot\mathcal{B}(J/\psi{\to}\ell^+\ell^-)\cdot\varepsilon \qquad (4.4)$$

where ε is the selection acceptance, $\mathcal{L}$ the integrated luminosity, and $\ell^+\ell^-$ stands for e^+e^- or $\mu^+\mu^-$. Given a number of observed ISR V, we can determine the product of $\Gamma_{V\to ee}\cdot\mathcal{B}(V{\to}J/\psi\pi^+\pi^-)$ by

$$\Gamma_{V\to ee}\cdot\mathcal{B}(V{\to}J/\psi\pi^+\pi^-) = \frac{N(\gamma\, V)\cdot m_V}{\varepsilon\cdot W(s,x_V)}\times\frac{s}{\mathcal{L}\cdot 12\pi^2\,\mathcal{B}(J/\psi{\to}\ell^+\ell^-)} \qquad (4.5)$$

where only the first part $\frac{N(\gamma\, V)\cdot m_V}{\varepsilon\cdot W(s,x_V)}$ on the equation right side depends on a specific vector meson.

4.1.2 Analysis strategy

The main kinematics features of the ISR $J/\psi\pi^+\pi^-$ with the $J/\psi\to\ell^+\ell^-$ are the following:

- simple topology: one energetic photon plus 2 pairs of back-to-back charged tracks

- the ISR photon and thus the $J/\psi\pi^+\pi^-$ state momenta are mainly oriented at small polar angle: the ISR photon escapes through the beam pipe around the 85% of the times, while the combined acceptance for the four charged tracks is about 22%
- a reconstructed J/ψ in the final state

Therefore the analysis strategy can be summarized as follow:

- look for a small recoiling mass against the final state
- look for small transfer momentum of the entire event
- the ISR photon will not be required.

4.1.3 Data and Monte Carlo samples

Datasets

The data sample consists of BaBar Runs 1-6 data listed below:

	$\mathcal{L}(OnPeak)$	$\mathcal{L}(OffPeak)$	$\mathcal{L}(sum)$
Run 1:	$20.41\,\text{fb}^{-1}$,	$2.62\,\text{fb}^{-1}$,	$23.03\,\text{fb}^{-1}$
Run 2:	$61.14\,\text{fb}^{-1}$,	$6.92\,\text{fb}^{-1}$,	$68.06\,\text{fb}^{-1}$
Run 3:	$32.28\,\text{fb}^{-1}$,	$2.47\,\text{fb}^{-1}$,	$34.75\,\text{fb}^{-1}$
Run 4:	$100.28\,\text{fb}^{-1}$,	$10.12\,\text{fb}^{-1}$,	$110.40\,\text{fb}^{-1}$
Run 5:	$132.87\,\text{fb}^{-1}$,	$14.49\,\text{fb}^{-1}$,	$147.36\,\text{fb}^{-1}$
Run 6:	$66.11\,\text{fb}^{-1}$,	$4.51\,\text{fb}^{-1}$,	$70.62\,\text{fb}^{-1}$
Total:	$413.09\,\text{fb}^{-1}$,	$41.13\,\text{fb}^{-1}$,	$454.22\,\text{fb}^{-1}$

Monte Carlo samples

We generate ISR Monte Carlo (MC) events for the following processes:

- $e^+e^-\to\gamma_{ISR}\psi(2S)(\to J/\psi\pi^+\pi^-)$ (VVPIPI)
- $e^+e^-\to\gamma_{ISR}\psi(2S)(\to J/\psi\pi^+\pi^-)$ (PHSP)
- $e^+e^-\to\gamma_{ISR}\psi(3770)(\to J/\psi\pi^+\pi^-)$ (PHSP)
- $e^+e^-\to\gamma_{ISR}X(3872)(\to J/\psi\pi^+\pi^-)$ (PHSP)

- $e^+e^- \to \gamma_{ISR} Y(4260)(\to J/\psi\pi^+\pi^-)$ (PHSP)
- $e^+e^- \to \gamma_{ISR}\psi(4330)(\to J/\psi\pi^+\pi^-)$ (PHSP)

All $e^+e^- \to \gamma_{ISR}V$ processes are generated using the $VECTORISR$ model, with the ISR gamma produced over the full solid angle. Two models are used to model the decay $V \to J/\psi\pi^+\pi^-$: phase space and $VVPIPI$ (*i.e.* multipole model). In the latter model, $m_{\pi\pi}$, the mass of the di-pion system, is distributed as (phase space)$\times(m^2_{\pi\pi} - 4m^2_\pi)^2$. The $\psi(2S)\to J/\psi\pi^+\pi^-$ decay has already been demonstrated by other experiments to be well described by the $VVPIPI$ model. Both $VVPIPI$ and phase space were generated for the $\psi(2S)$, but only phase space was used for the other samples. Model dependence for the reconstruction efficiency of the Y is determined by the two $\psi(2S)$ samples. In all cases, the J/ψ decays into $\ell^+\ell^-$ in VLL model, where $\ell^+\ell^- = e^+e^-$ or $\mu^+\mu^-$. The polarization has been properly considered in the generation.

In addition the following generic Monte Carlo are used for the background study:

- generic uds
- generic $c\bar{c}$
- $e^+e^- \to \Upsilon(4S) \to b\bar{b}$
- $\tau^+\tau^-$

4.1.4 Event reconstruction

Reconstruction of $J/\psi \to \ell^+\ell^-$.

In the events, J/ψ candidates are reconstructed via their decays to e^+e^- or $\mu^+\mu^-$. For e^+e^- one electron is required to be $eLHBremAndGTL$ [1] (i.e. a $GoodTracksLoose$ [2] satisfying $PidLHElectrons$ and with bremsstrahlung radiation recovery) and the other is required to be $eBremReco$ (a $ChargedTracks$ with bremsstrahlung radiation recovery). For the $\mu^+\mu^-$ one muon is required to be a $muNNVeryLoose$ and the other a $GoodTracksLoose$. A geometric fit of the J/ψ candidate is conduced using an algorithm with beam-spot constraint and the fit probability is required to be $> 10^{-3}$.

[1] All the *BABAR* Particle Identification selectors are described in Appendix A
[2] All the *BABAR* Tracks lists are described in Appendix A

Reconstruction of the final state.

The J/ψ candidate is then combined with two $piLHVeryLoose$ tracks to reconstruct the final state. A geometric fit of the final state candidate is performed with the a fitter algorithm with beam spot constraint and requiring a minimum fit probability of 10^{-3} before the mass constraint on its grand daughter J/ψ . The $J/\psi\pi^+\pi^-$ invariant mass and momentum are calculated with the J/ψ candidate mass constrained to the nominal J/ψ value.

4.2 The selection criteria

Given the basic features of the ISR $J/\psi\pi^+\pi^-$ events discussed earlier the following variables have been evaluated for use as selection criteria:

- $cosP$: cosine of the angle between the π^+ momentum direction in the di-pion rest frame and the di-pion momentum direction in the $J/\psi\pi^+\pi^-$ rest frame.
- $nGTk$: number of $GoodTracksLoose$.
- p^*_{miss}, $\cos\theta^*_{miss}$ and pt^*_{miss}: the magnitude, the cosine of the polar angle and the transverse component of the missing momentum vector of the entire event in the C. M. frame, respectively. All charged and neutral tracks (which is defined in the item of N_γ) including the ISR gamma if detected are used in the calculation.
- $m(\ell^+\ell^-)$: the invariant mass of the J/ψ candidate.
- $\cos\theta_l$: Cosine of the helicity angle of the J/ψ decay, which is the angle between ℓ momentum direction in J/ψ rest frame and the J/ψ momentum direction in the C.M. frame. Please notice the difference of this angle definition from the "*normal*" helicity angle definition.
- m_{rec}: The mass recoiling against the $J/\psi\pi^+\pi^-$ system. It is calculated from the following formula,

$$m^2_{rec} = (\sqrt{s} - E^*_{J/\psi\pi^+\pi^-})^2 - p^{*2}_{J/\psi\pi^+\pi^-} \tag{4.6}$$

  where $E^*_{J/\psi\pi^+\pi^-}$ and $p^*_{J/\psi\pi^+\pi^-}$ are the energy and momentum of $J/\psi\pi^+\pi^-$ in the e^+e^- C.M. frame, respectively.

- N_γ: Number of neutral tracks from the *GoodPhotonLoose* (appendix **??**) list.
- E^*_γ: Energy of the most energetic gamma in the C.M. frame.

4.3 Selection optimization

The optimization goal is to maximize the significance of potential signals in an unbiased manner. Because background sources are not well known and we do not have good generators to produce the background, the selection optimization makes use of the Run 1-6 data samples, taking the nearly background-free ISR $\psi(2S)$ events as signal, and considering as background the $\psi(2S)$ sideband events within the mass regions: [3.8,4.2] GeV/c^2 ("$\psi(2S)$ sidebands"). Fig. 4.1 show the $m(J/\psi\pi^+\pi^-)$ invariant mass distributions of the $J/\psi\pi^+\pi^-$ candidates between 3.6 and 4.2 GeV/c^2, the most of the events are under the $\psi(2S)$ peak which is the region we use as signal in the optimization. Nevertheless we also checked that using signal MC events in the optimization gives similar results in the optimization.

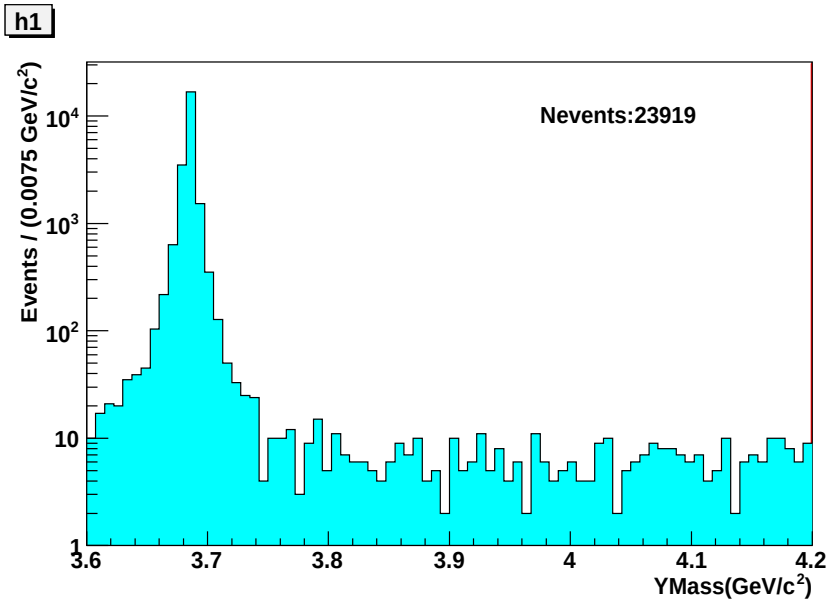

Figure 4.1: Invariant mass distribution of the $J/\psi\pi^+\pi^-$ candidates between 3.6 and 4.2 GeV/c^2.

The $m(J/\psi\pi^+\pi^-)$ region [4.2,5.0] GeV/c^2 is considered as the ISR Y signal region, and thus is blinded during the optimization. It is assumed in the optimization

that the ISR $\psi(2S)$ events behave in the same way as the ISR Y signal events, and most of the ISR $\psi(2S)$ sidebands events are backgrounds. This assumption may not be strictly true, but we know of no better alternative.

The selection was optimized with a method developed for other charmonium analyses.

We have optimized the sensitivity $s = S/(a/2 + \sqrt{B})$, where

- a=5 (see article [62]), which means the optimization is performed in search for a signal with a significance of 5 σ.
- B is the number of background events which will be evaluated counting the number of the ISR $\psi(2S)$ sidebands events. Given the values of the $\psi(2S)$ peak region of 20 MeV/c^2 and the mass range of 400 MeV/c^2 for the sidebands, the scaling factor is F=400 MeV/20 MeV =20.
- S is the number of the ISR $\psi(2S)$ data events within the $m(J/\psi\pi^+\pi^-)$ region: $|m(J/\psi\pi^+\pi^-) - 3.6861| < 0.010\,\mathrm{GeV}/c^2$ ("$\psi(2S)$ mass window").

Some of these variables are strongly correlated like m_{rec}, E^*_γ and p^*_{miss} so they are redundant, others $cosP$, N_γ and $\cos\theta^*_{miss}$ are less useful discriminators and are not used in the final selection.

Figures 4.2 and 4.3 show the distribution of the variables used in the selection for events under the $\psi(2S)$ peak and the $\psi(2S)$ sidebands events in the data, the ISR $\psi(2S)$ and ISR Y signal MC samples.

- The lepton helicity angle ($\cos\theta_l$) in Figure 4.2(a) and 4.2(b) is distributed as $1+\cos^2\theta$ at the generation level, but it peaks in the center due to the detector acceptance and the predominance along the beam direction of the $J/\psi\pi^+\pi^-$ momentum for the ISR $J/\psi\pi^+\pi^-$ events. The $\mu^+\mu^-$ distribution is sightly wider than the e^+e^- distribution because the geometric (especially in forward direction) acceptance of the IFR is larger than the EMC, nevertheless the cut on this variable is the same for the two J/ψ decay mode: $|\cos\theta_l| < 0.925$.
- The mass recoiling against the $J/\psi\pi^+\pi^-$ system peaks at zero for the ISR $J/\psi\pi^+\pi^-$ events, m_{rec} is required to be between [-0.5, +0.75] GeV/c^2 (Fig.

4.2(c) and 4.2(d)). The enhancement at zero, visible for the ISR $\psi(2S)$ sidebands events, will be addressed later with the study of the J/ψ sideband events.

- The di-lepton mass minus the J/ψ nominal mass (Fig. 4.2(e) and 4.2(f)) peaks at zero for true $J/\psi \to \ell^+\ell^-$ events. Different cuts have been chosen for $J/\psi \to e^+e^-$ and $J/\psi \to \mu^+\mu^-$ events as different are the distributions: [-75, +55] MeV/c^2 for $J/\psi \to e^+e^-$ and [-55, +55] MeV/c^2 for $J/\psi \to \mu^+\mu^-$. The peak at zero, visible for the ISR $\psi(2S)$ sidebands events, will be discussed later in this section.

- $nGTk$: the number of $GoodTrkLoose$ tracks is expected to be 4 for $J/\psi\pi^+\pi^-$ ($J/\psi \to \ell^+\ell^-$) events. From figure 4.3(a) the $nGTk$ doesn't appear a variable with a big discriminating power, nevertheless we decide to reject the events with more than 4 $GoodTrkLoose$ to contain the number of multiple candidates.

- the transverse component of the missing momentum vector of the entire event in the C. M. frame, pt^*_{miss}, is small for good ISR $J/\psi\pi^+\pi^-$ events. We select events with $pt^*_{miss} < 2.25\,\mathrm{GeV}/c^2$ (Fig. 4.3(b)).

Electron pairs contamination. Figure 4.4 shows the electron micro selector distribution for the pions of the selected events for signal and background: many of them are identified as Tight or VeryTight electrons, they are mostly electron pairs. To avoid such a contamination we reject pions identified as Tight or VeryTight electrons.

$\cos\alpha$ **cut.** Alpha is the angle between the J/ψ and the π^+ in the di-pion rest frame. The cut on the cosine of this angle has been added later in the analysis to improve the reduction of the electron pair contamination in our data sample. In figure 4.5 are reported the distributions of this variable for data and Y(4260) MC, while figure 4.6 shows the same distribution for data in the Y(4260) region for $J/\psi \to e^+e^-$ and $J/\psi \to \mu^+\mu^-$. A cut at 0.9 has been applied only for $J/\psi \to e^+e^-$. This cut is not included in the results presented at ICHEP 08 and published in Ref. [64].
The final selection criteria are summarized in Table 4.2.

For comparison we report the cut of the old analysis in table 4.3.

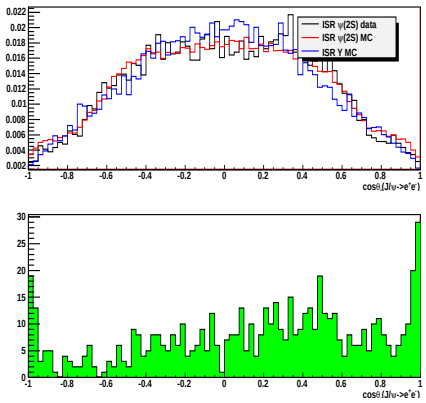

(a) $\cos\theta_l$ distribution for $J/\psi \to e^+e^-$

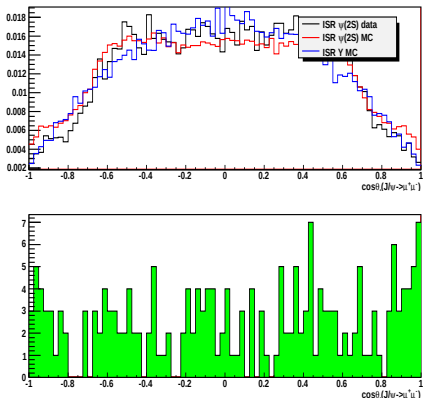

(b) $\cos\theta_l$ distribution for $J/\psi \to \mu^+\mu^-$

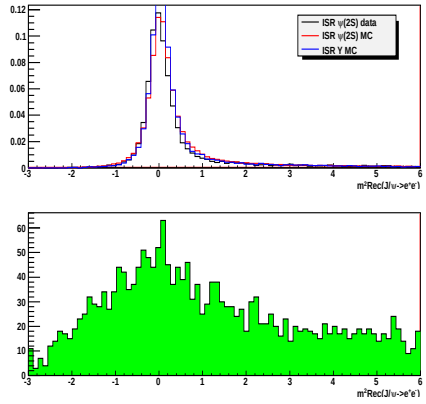

(c) m_{rec} distribution for $J/\psi \to e^+e^-$

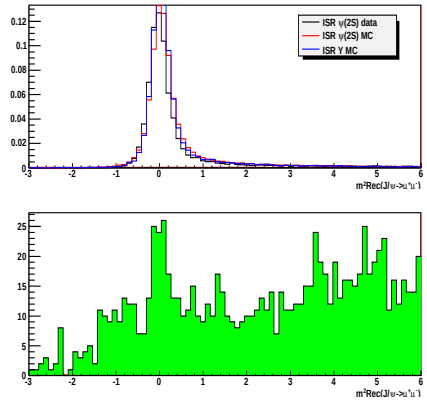

(d) m_{rec} distribution for $J/\psi \to \mu^+\mu^-$

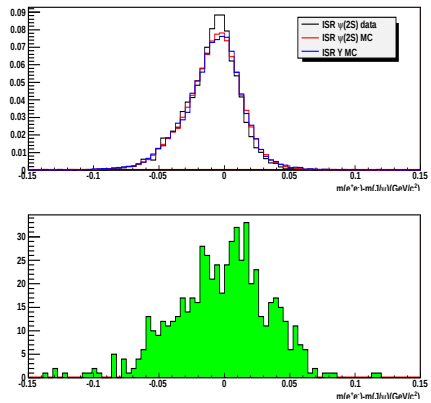

(e) $m(\ell^+\ell^-) - m(J/\psi)$ distribution for $J/\psi \to e^+e^-$

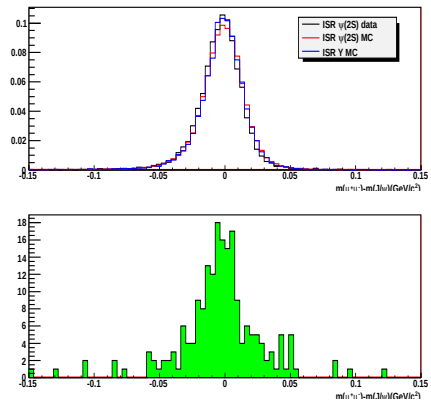

(f) $m(\ell^+\ell^-) - m(J/\psi)$ distribution for $J/\psi \to \mu^+\mu^-$

Figure 4.2: Distributions of $\cos\theta_l$, m_{rec} and $m(\ell^+\ell^-) - m(J/\psi)$ after all cuts except the one shown in the plot have been applied, where the black line is for the ISR $\psi(2S)$ data, the red line for the ISR $\psi(2S)$ MC, the blue line for the ISR Y MC, and the green histogram for the ISR $\psi(2S)$ sidebands data.

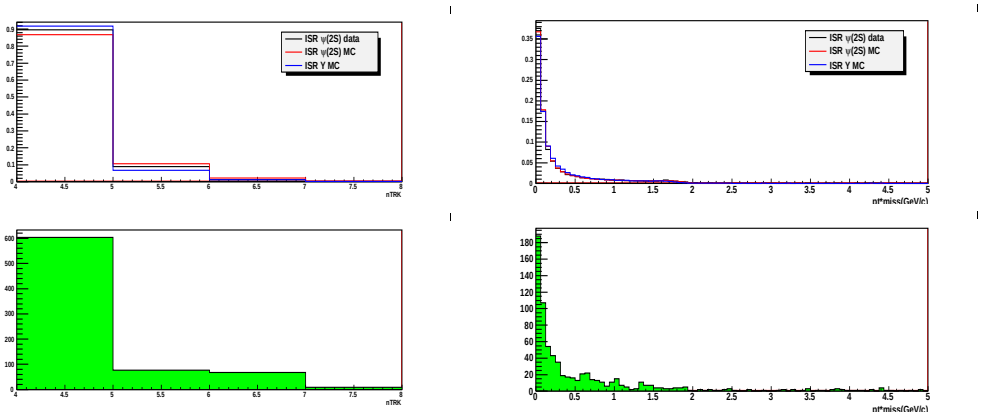

(a) $nTrks$ distribution (b) pt^*_{miss} distribution

Figure 4.3: Distributions of $nTrks$ and pt^*_{miss} after all cuts except the one shown in the plot have been applied, where the black line is for the ISR $\psi(2S)$ data, the red line for the ISR $\psi(2S)$ MC, the blue line for the ISR Y MC, and the green histogram for the ISR $\psi(2S)$ sidebands data.

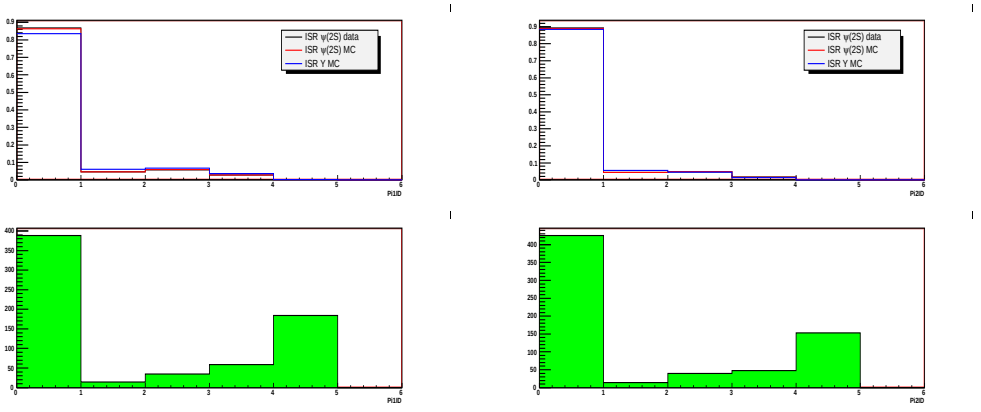

(a) First pion (b) Second pion

Figure 4.4: Electron micro selector values for the pions of the selected events: 4 is when a pion is identified as VeryTight electron, 3 Tight, 2 Loose and 1 VeryLoose. 0 is when the pion is not identified as an electron. On top distribution for signal events, at the bottom for $\psi(2S)$ sideband events.

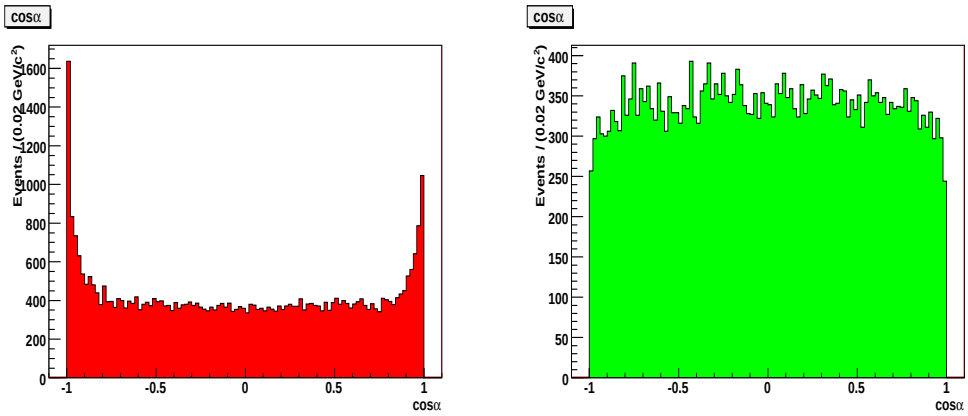

(a) All the data (b) Y(4260 M.C.

Figure 4.5: Distribution of the cosine of the angle between the J/ψ and the π^+ in the di-pion rest frame for data and M.C.

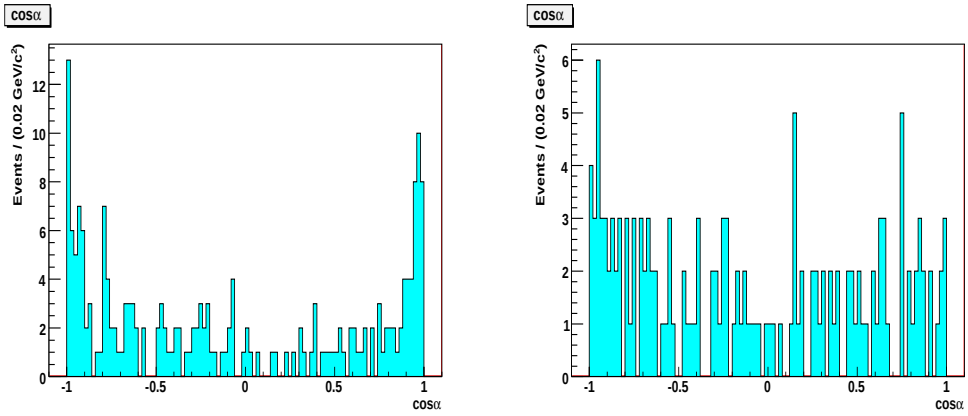

(a) $J/\psi \to e^+e^-$ (b) $J/\psi \to \mu^+\mu^-$

Figure 4.6: Distribution of the cosine of the angle between the J/ψ and the π^+ in the di-pion rest frame for data in the Y(4260) region for $J/\psi \to e^+e^-$ and $J/\psi \to \mu^+\mu^-$.

Table 4.2: The final selection criteria for ISR $J/\psi\pi^+\pi^-$.

	$J/\psi \to e^+e^-$	$J/\psi \to \mu^+\mu^-$
Lepton PID	at least one tight $eLHPid$	at least one tight $muNNPid$
$m(\ell^+\ell^-) - m(J/\psi)$	[-75, +55] MeV/c^2	[-55, +55] MeV/c^2
m_{rec}	[-0.5, +0.75] GeV/c^2	
Lepton tracks	both are $GoodTrkLoose$	
$\pi^+\pi^-$ tracks	both are $GoodTrkVeryLoose$	
$nGTk$	4	
pt^*_{miss}	< 2.25 GeV/c^2	
$\pi^+\pi^-$ PID	very loose $piLHPid$ for both $\pi^+\pi^-$ and not Tight electron	
$\lvert\cos\theta_l\rvert$	< 0.925	
$cos\alpha$	< 0.9	-

Table 4.3: The final selection criteria of the old *BABAR* analysis and not used here.

	$J/\psi \to e^+e^-$	$J/\psi \to \mu^+\mu^-$
$m(\ell^+\ell^-) - m(J/\psi)$	[-95, +33] MeV/c^2	[-40, +33] MeV/c^2
$\cos(Pi)$	<0.90	no cut
m_{rec}	[-1.012, +1.807] GeV/c^2	[-1.029, +1.119] GeV/c^2
$nGTk$	4	
pt^*_{miss}	< 2.5 GeV/c^2	
$\lvert\cos\theta_l\rvert$	< 0.9	

Background evaluation

There are two sorts of backgrounds contaminating the ISR $J/\psi\pi^+\pi^-$ events: events with a genuine J/ψ or a fake J/ψ (combinatorial). Lepton PID, J/ψ mass window, lepton helicity angle and lepton track quality are used to remove the fake J/ψ background. In order to remove the genuine J/ψ background, we applied the ISR nature requirements: low missing transverse momentum and small recoil mass against $J/\psi\pi^+\pi^-$. The fake J/ψ background can be estimated by J/ψ sidebands events.

Figure 4.7 shows the invariant mass distribution for the $J/\psi\pi^+\pi^-$ candidates in the $\psi(2S)$ background region (i.e. for $3.8 < m(J/\psi\pi^+\pi^-) < 4.2$) which is an estimation of the final background level.

The following lists the possible backgrounds and how they are removed some Monte Carlo sample have been used as cross-check for the background rejection of our analysis.

- *uds* continuum events are likely to have more than 4 charged tracks. Their recoil mass are usually large. The kind of contamination is quite significant. 22 events survived our selection over 100fb^{-1} of Monte Carlo in the region [3.8-4.2] GeV/c^2 which will be roughly 25% of the background events remaining after the selection.

- $b\bar{b}$ events are removed by the requirement on the number of *GoodTrkLoose* tracks and small recoil mass. 0 events passed our selection in 200fb^{-1} of Monte Carlo processed so far.

- Generic $c\bar{c}$ events contamination is negligible: 0 events passed our selection in 175fb^{-1} of Monte Carlo.

- $\tau^+\tau^-$: a large fraction of $\tau^+\tau^-$ events have 4 charged tracks in the final states. But they do not have a J/ψ and are likely to have large missing transfer momentum and large recoil mass: 3 $\tau^+\tau^-$ events passed our selection over 75fb^{-1} of Monte Carlo in the region [3.8-4.2] GeV/c^2.

- Bhabhas, di-muons and other sources of background can be easily suppressed and can be ignored.

- Non-resonant ISR $J/\psi\pi^+\pi^-$ production will be estimated by fitting to the $m(J/\psi\pi^+\pi^-)$ spectrum.

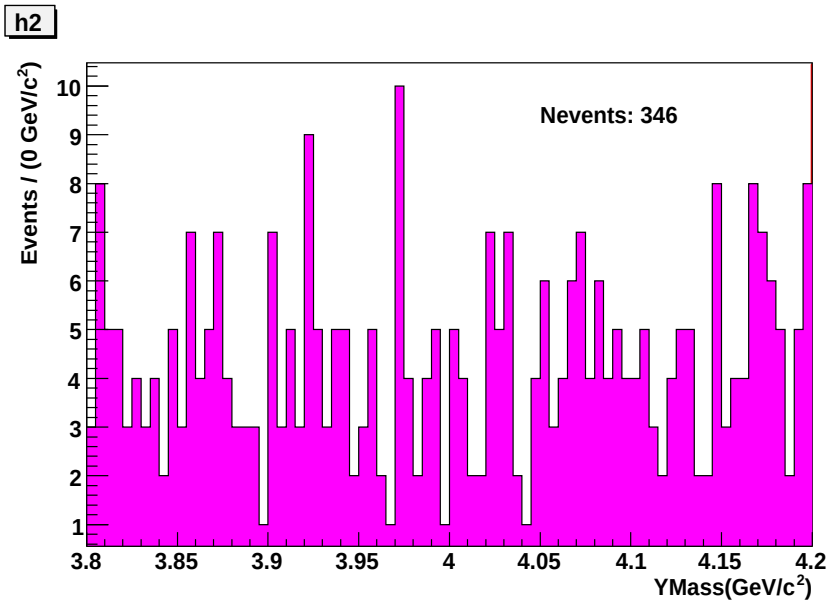

Figure 4.7: Invariant mass distribution of the $J/\psi\pi^+\pi^-$ candidates in the $\psi(2S)$ background region (i.e. between 3.8 and 4.2 GeV/c^2).

4.3.1 Checks on the selected events

Features of the selected events

Figure 4.8 shows the number of photons, the energy of the most energetic photon, the polar angle of the $J/\psi\pi^+\pi^-$ system in the C.M. frame for $\psi(2S)$ peak data and Monte Carlo signal events as well for the $\psi(2S)$ sideband data (background events): all the distributions look very similar this means that all the selected events including the ISR $\psi(2S)$ sidebands (background) events are ISR-like events. All the samples peak along the beam direction. As shown in Figure 4.8(d), the $J/\psi\pi^+\pi^-$ momentum points to the beam direction when the ISR gamma is undetected. There are a few events with the $J/\psi\pi^+\pi^-$ momentum pointing to within the acceptance region because the ISR gamma entering the barrel was not reconstructed. About one fourth of the selected ISR events in the data have a gamma detected as a neutral cluster with the energy greater than 3 GeV.

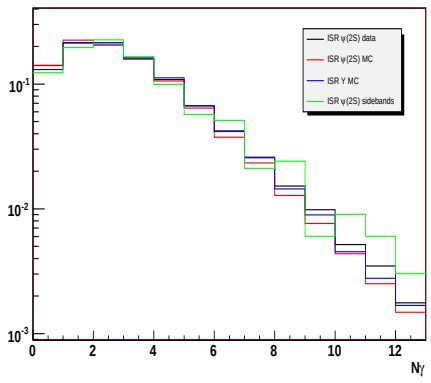

(a) Normalized distribution of number of gammas.

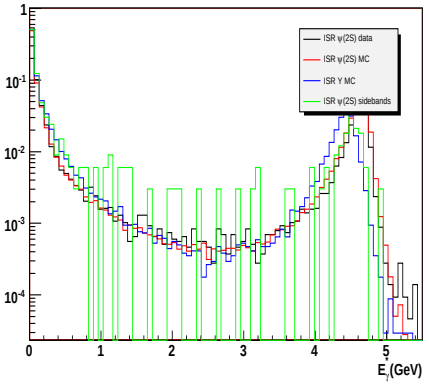

(b) Normalized E^*_γ distribution.

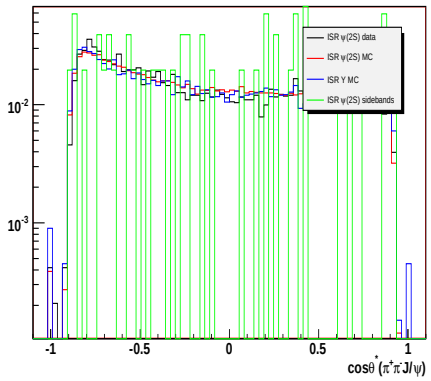

(c) Normalized $\cos\theta^*(J/\psi\pi^+\pi^-)$ distribution with the ISR gamma detected.

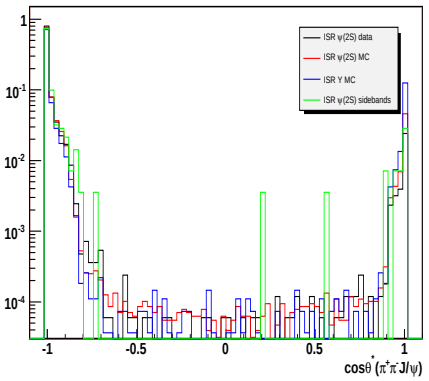

(d) Normalized $\cos\theta^*(J/\psi\pi^+\pi^-)$ distribution with the ISR gamma undetected.

Figure 4.8: The distributions of number of gammas N_γ, the energy of the most energetic gamma E^*_γ, and $\cos\theta^*(J/\psi\pi^+\pi^-)$ for ISR $J/\psi\pi^+\pi^-$ candidates. Black is ISR $\psi(2S)$ data, red is ISR $\psi(2S)$ MC, blue is ISR Y(4260) MC and green is $\psi(2S)$ sideband region.

Features of the J/ψ sidebands

Another crosscheck has been done looking at the J/ψ sidebands events with $m(\ell^+\ell^-) - m(J/\psi)$ within the regions:

- [-190,-125] MeV/c^2 plus [+105,+160] MeV/c^2 for $J/\psi \to e^+e^-$,
- [-160,-105] MeV/c^2 plus [+105,+160] MeV/c^2 for $J/\psi \to \mu^+\mu^-$.

The corresponding distributions of discriminating variables for these events are shown in Figure 4.9 (the distributions of the same variables for the $J/\psi\pi^+\pi^-$ candidates are shown in figures 4.2 and 4.3). The angular distribution, pt^*_{miss} and the number of tracks are quite similar to the J/ψ peak events, the m_{rec} distribution shows a peak close to 0 for $\mu^+\mu^-$ events probably due to muon/pion mis-ID.

J/ψ sideband contribution to the ISR $J/\psi\pi^+\pi^-$ events

Figure 4.10 shows the $m(J/\psi\pi^+\pi^-)$ distribution for J/ψ sidebands events and for the final ISR $J/\psi\pi^+\pi^-$ sample. The $\psi(2S)$ peak is still visible in Figure 4.10(a) and 4.10(b) for the J/ψ sidebands events because there are still some real J/ψ events within the J/ψ sidebands, mostly to $\mu^+\mu^-$ in agreement with the m_{rec} distribution shown before. Figure 4.10(e) and 4.10(f), which show the $m(J/\psi\pi^+\pi^-)$ distribution in the region [3.8-4.2] GeV/c^2 for $J/\psi \to e^+e^-$ and $J/\psi \to \mu^+\mu^-$ respectively, indicate that our final background level is quite low: less than two events per MeV/c^2 and it can be well estimate by the J/ψ sidebands.

Δp^* distribution

As another cross-check, we also studied the distribution of the variable Δp^*, the difference between the measured $J/\psi\pi^+\pi^-$ momentum in the CM frame and the predicted momentum for the V in an ISR process $e^+e^- \to \gamma_{ISR}V$ by the formula $p^*_V = E_{cm}/2 - m^2_V/(2E_{cm})$. It is strongly correlated to m_{rec}, the recoil mass against $J/\psi\pi^+\pi^-$, because both of them are calculated from the two physical variables $p^*(J/\psi\pi^+\pi^-)$ and $m(J/\psi\pi^+\pi^-)$. The Δp^* distributions are shown in Figure 4.11 for $\psi(2S)$ peak and for $\psi(2S)$ sideband events. A peak around zero is visible in both Figure 4.11(a) and 4.11(b) for the ISR $\psi(2S)$ sidebands events. This peak also indicates that there are ISR events even within the ISR $\psi(2S)$ sidebands.

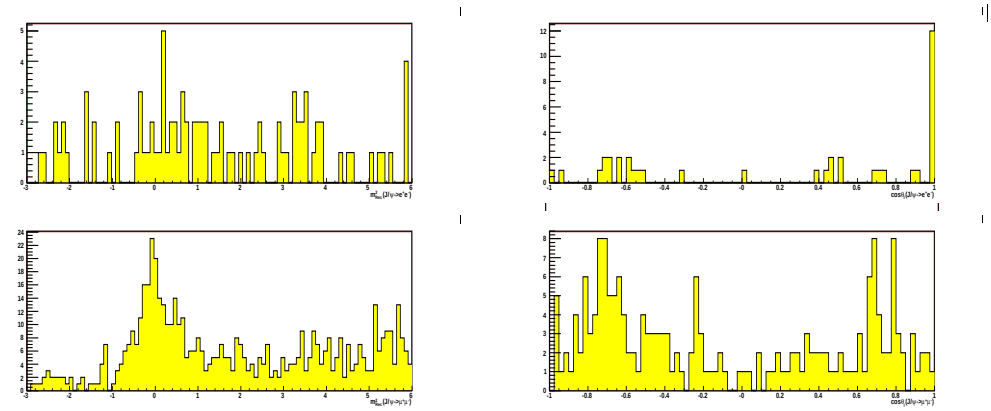

(a) m_{rec} (b) $\cos\theta_l$

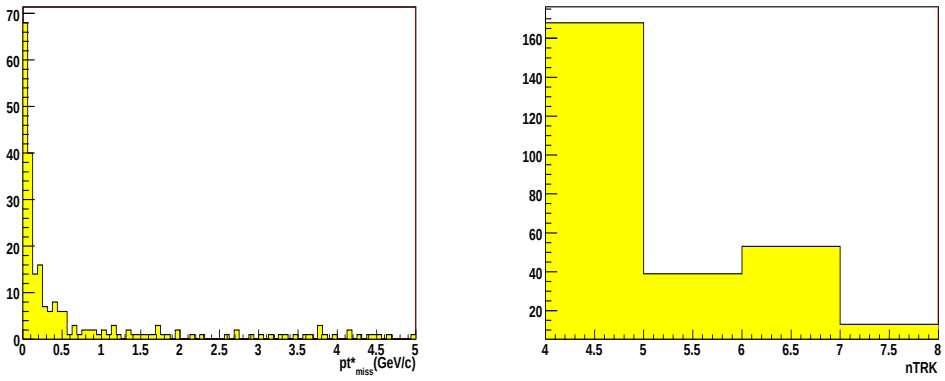

(c) pt^*_{miss} (d) $nTrks$

Figure 4.9: Distributions of discriminating variables for the J/ψ sidebands events after all cuts except the one shown here have been applied.

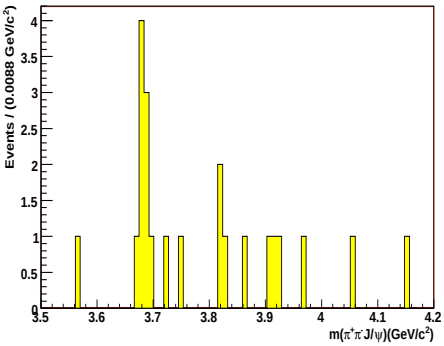

(a) $m(J/\psi\pi^+\pi^-)$ distribution ($J/\psi\to e^+e^-$) for the J/ψ sideband: few good events are present under the $\psi(2S)$ peak.

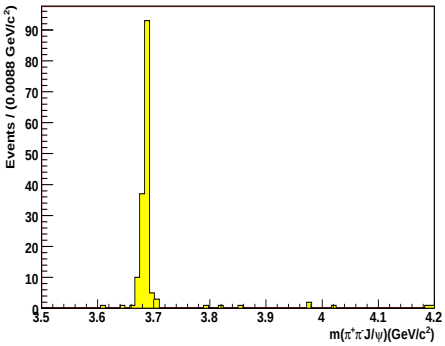

(b) $m(J/\psi\pi^+\pi^-)$ distribution ($J/\psi\to\mu^+\mu^-$) for the J/ψ sideband: some good events are present under the $\psi(2S)$ peak.

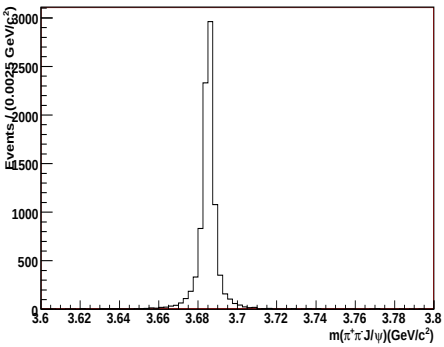

(c) $m(J/\psi\pi^+\pi^-)$ distribution ($J/\psi\to e^+e^-$) on the $\psi(2S)$ peak (signal events).

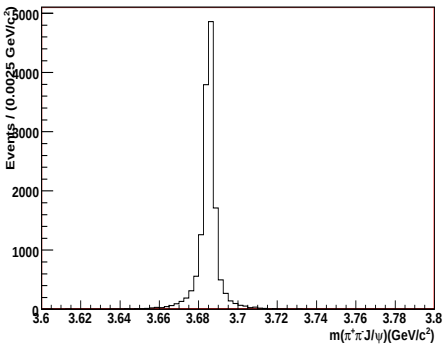

(d) $m(J/\psi\pi^+\pi^-)$ distribution ($J/\psi\to\mu^+\mu^-$) on the $\psi(2S)$ peak (signal events).

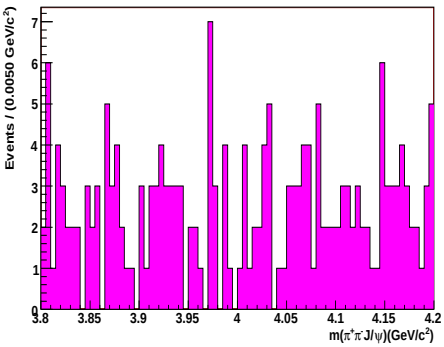

(e) $m(J/\psi\pi^+\pi^-)$ distribution ($J/\psi\to e^+e^-$) on the $\psi(2S)$ sideband (3.8-4.2 GeV/c^2).

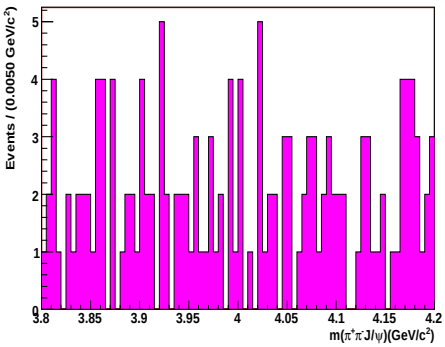

(f) $m(J/\psi\pi^+\pi^-)$ distribution ($J/\psi\to\mu^+\mu^-$) on the $\psi(2S)$ sideband (3.8-4.2 GeV/c^2).

Figure 4.10: Distribution of $m(J/\psi\pi^+\pi^-)$ for the J/ψ sidebands events (top) compared with the $J/\psi\pi^+\pi^-$ candidates under the $\psi(2S)$ peak (middle) and on the $\psi(2S)$ sideband (bottom).

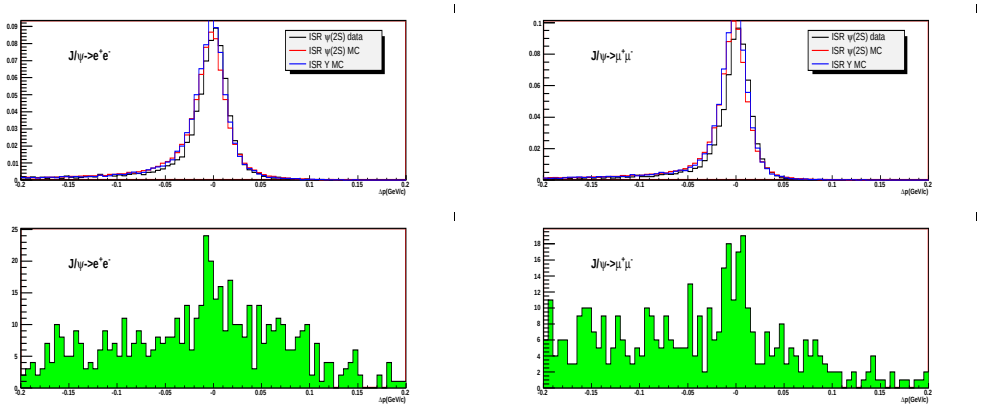

(a) Δp^* for $J/\psi \to e^+e^-$ under the J/ψ peak. (b) Δp^* for $J/\psi \to \mu^+\mu^-$ under the J/ψ peak.

Figure 4.11: The Δp^* distribution for $J/\psi\pi^+\pi^-$ events before the cut on m_{rec}: signal events on top, the green histogram stands for the $\psi(2S)$ sideband events.

4.3.2 Multiple candidates

There are 24034 events and 24117 candidates in run 1-6 data with $m(J/\psi\pi^+\pi^-)$ in the mass region [3.5 GeV/c^2- 5 GeV/c^2] that pass the final selection; this number is in agreement with the number of multiple candidate found in the MC events and it of the same order of magnitude of the one found in the old analysis. Two causes can contribute to the multiple candidates: the first one is that one $\ell^+\ell^-$ combination was reconstructed as both $J/\psi \to e^+e^-$ and $J/\psi \to \mu^+\mu^-$ candidates because only one lepton was required to be identified, the second cause is multiple different $\pi^+\pi^-$ combinations in an event. Anyway these multiple candidate events do not produce any bump other than the $\psi(2S)$ peak as shown in figure 4.12 and their contribution is negligible.

4.3.3 Di-pion invariant mass distribution

The invariant mass and the cosine of the polar angle of the $\pi^+\pi^-$ system is reported in figure 4.13, no cut has been applied since the Monte Carlo events for the $Y(4260) \to J/\psi\pi^+\pi^-$ have been generated with a phase space distribution because there's no established model for this decay.

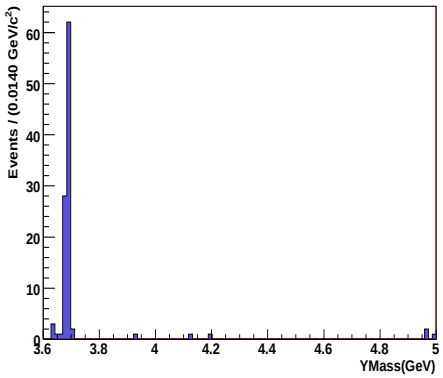

Figure 4.12: $m(J/\psi\pi^+\pi^-)$ distribution for multiple candidates.

4.4 Fit procedure and validation

4.4.1 Resolution studies

In order to obtain the mass, width and yield of resonances in the $m(J/\psi\pi^+\pi^-)$ mass spectrum, the mass resolution shape and mass shift must be determined. An unbinned maximum likelihood fit has been performed either on the data at the $\psi(2S)$ peak and on Monte Carlo samples to extract the mass resolution and the efficiency of the analysis. A *Gaussian*, a $Breit-Wigner$, a $Voigtian$ (*i.e.* a B-W convoluted with a *Gaussian*) and a B-W convoluted with two *Gaussians* have been used to describe the shape of the $m(J/\psi\pi^+\pi^-)$ spectrum.

Fit on Monte Carlo. The $m(J/\psi\pi^+\pi^-)$ shape (as shown in Figure 4.14) is well described by a B-W convoluted with two *Gaussians*. The $\psi(2S)$ natural width is below our experimental resolution (4.14(b)) therefore we will use the measured $\Gamma_{\psi(2S)}$ as mass resolution to fit broader resonances. For broader resonances the fit with a $Voigtian$ PDF gives a good description of the mass spectrum. As an example we fit the $m(J/\psi\pi^+\pi^-)$ spectrum for $Y(4260)$ Monte Carlo (fig. 4.15): mass and width of the resonance are in agreement with the generated values and the χ^2 is close to 1. Then, from an extended maximum likelihood fit we extract the number of $J/\psi\pi^+\pi^-$ candidate to calculate the efficiency of the selection.
We fit different Monte Carlo samples to study the dependence of the resolution and the efficiency from the mass of the $J/\psi\pi^+\pi^-$) state, all the results are summarized in Table 4.4. The efficiencies ranges in the same interval than in the old BaBar

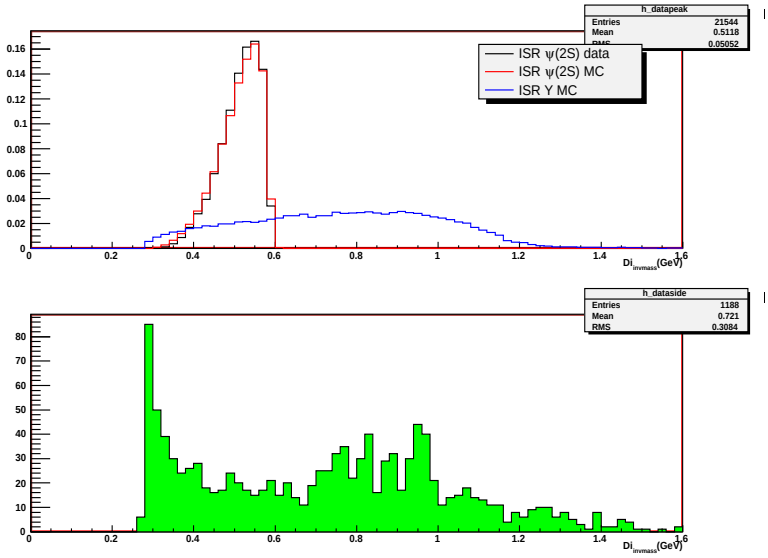

(a) Di-pion invariant mass

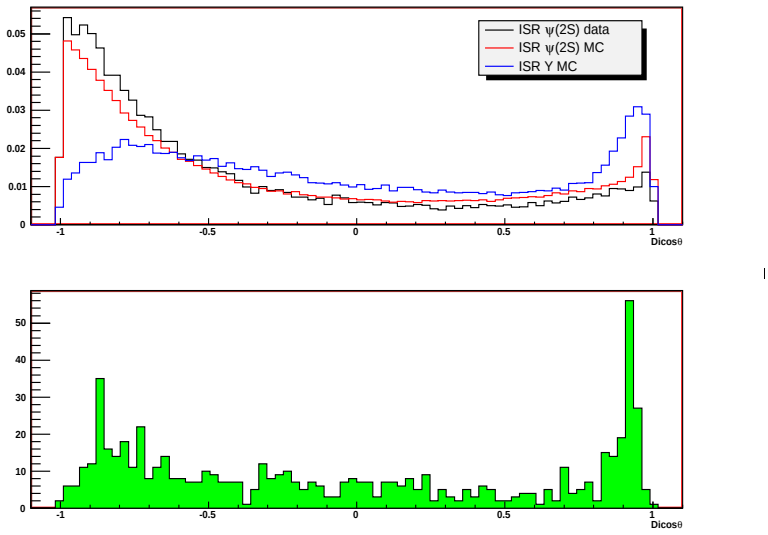

(b) Di-pion $\cos\theta$

Figure 4.13: Distributions of the invariant mass and the cosine of the polar angle of the dipions. The green histograms correspond to the $\psi(2S)$ sidebands.

analysis.

Table 4.4: Efficiency and resolution from Monte Carlo.

Resonance	Input Mass (MeV/c^2)	Output Mass (MeV/c^2)	Input width MeV/c	Γ (width) MeV/c	Efficiency (%)
$\psi(2S)(VVPIPI)$	3685.96	3685.99 ± 0.01	0.3	3.57 ± 0.06	9.03±0.02
$\psi(2S)(PHSP)$	3685.96	3686.02 ± 0.02	0.3	2.75 ± 0.06	9.96±0.06
$\psi(3770)$	3770	3769.90 ± 0.12	23	25.38 ± 0.43	10.54±0.07
$X(3872)$	3872	3871.91 ± 0.02	0	3.00 ± 0.07	11.54±0.07
$Y(4250)$	4250.0	4249.58 ± 0.10	20.0	21.62 ± 0.22	15.05 ± 0.08
$Y(4260)$	4260.0	4260.99 ± 0.35	90.0	91.56 ± 0.73	15.09 ± 0.08
$Y(4330)$	4330.0	4329.73 ± 0.09	20.0	21.94 ± 0.19	15.80±0.08

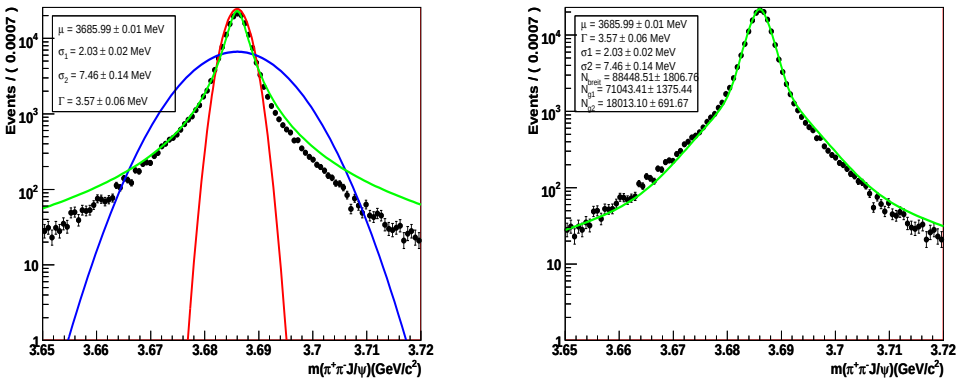

(a) $\psi(2S)$ MC fit

(b) $\psi(2S)$ MC fit with a B-W convoluted with two *Gaussians*

Figure 4.14: Unbinned maximum likelihood fit to $m(J/\psi\pi^+\pi^-)$ for $\psi(2S)$ Monte Carlo events with various PDFs. In the left plot the black points are the data, the blue line is the Gaussian, red is the Breit-Wigner and green is the Voigtian in the right plot a fit with a B-W convoluted with two *Gaussians* is shown.

4.4.2 Fit to the $\psi(2S)$ data

Figure 4.16 shows the fit at the $m(J/\psi\pi^+\pi^-)$ distribution for the data at $\psi(2S)$ energy. As it was for the Monte Carlo the *Voigtian* is the function which better describes the data. Fit outputs are summarized in table 4.5 and are referred to the fit shown in fig 4.17 (bottom). A mass shift of $-0.77 \pm 0.04\,\mathrm{MeV}/c^2$ relative to the

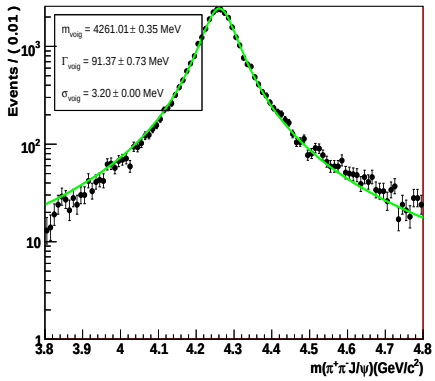

(a) $Y(4260)$ MC fit

Figure 4.15: Maximum likelihood fit to $m(J/\psi\pi^+\pi^-)$ for $Y(4260)$ Monte Carlo events with a B-W convoluted with a *Gaussian* PDFs.

PDG08 [63] value for the $\psi(2S)$ is observed in the data. This mass shift will be considered as systematic error in the mass determination.

Table 4.5: Fit results from $\psi(2S)$ data and Monte Carlo

Parameter	Data	Monte Carlo	PDG08
Mass (MeV/c^2)	3685.33± 0.02	3685.99 ± 0.01	3686.09 ± 0.04
Γ (MeV/c)	4.08 ± 0.20	3.57 ± 0.06	0.32 ± 0.01
evts. from ext. M.L. fit	23259 ± 154 $[3.6-3.9]$ GeV/c^2	-	-
background evts. from fit	124 ± 24 $[3.6-3.9]$ GeV/c^2	-	-

Fig. 4.17 we see the fit with signal PDF + linear background, used to extract the number of signal events and the resonance parameters: on the top plot is shown the fit to the $\psi(2S)$ data with a Voigtian + linear background, on the bottom one we used a Breith-Wigner convoluted with a double goussian which describes a slightly better the slopes of the distribution. Anyway both fits work very well and gives the same results.

Test of the analysis at the ψ(2S)

A test of the analysis selection has been done on the $\psi(2S)$ resonance which is the benchmark channel for this analysis: from a Maximum Likelihood fit to $m(J/\psi\pi^+\pi^-)$ reported in Fig. 4.17(b) , in the mass region $[3.6,3.9]$ GeV/c^2 for the

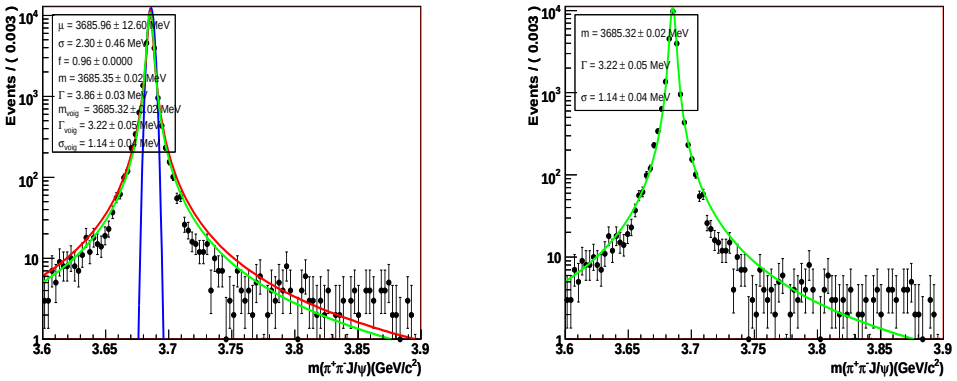

(a) Fit to $\psi(2S)$ data (b) $\psi(2S)$ fit with a Voigtian

Figure 4.16: Unbinned maximum likelihood fit to $m(J/\psi\pi^+\pi^-)$ with various PDFs. The black points are the data, the blue line is the Gaussian, red is the Breit-Wigner and green is the Voigtian.

ISR $\psi(2S)$ MC sample (see Table 4.5), we get the acceptance of the analysis:

$$\varepsilon = (9.03 \pm 0.02)\%,$$

Using the branching fraction of $\mathcal{B}(\psi(2S) \to J/\psi\pi^+\pi^-)$ and $\mathcal{B}(J/\psi \to \ell^+\ell^-)$ in PDG08 and the number of events extracted from a Maximum Likelihood fit to $\psi(2S)$ data, we expect:

$$\begin{aligned}\sigma_{meas}(e^+e^- \to \gamma\,\psi(2S)) &= \frac{N(\gamma\,\psi(2S))}{\mathcal{L} \times \varepsilon \times \times \mathcal{B}(\psi(2S) \to J/\psi\pi^+\pi^-) \times \mathcal{B}(J/\psi \to \ell^+\ell^-)} \\ &= \frac{(23134 \pm 152)}{(454 \pm 5)fb^{-1} \times (9.03 \pm 0.02)\% \times (32.6 \pm 0.5)\% \times (2 \times 5.93 \pm 0.06)\%} \\ &= 14.9 \pm 0.4\end{aligned}$$

Which is in good agreement with the theoretical expectation reported in table 4.1.1: $\sigma_{theo}(e^+e^- \to \gamma\,\psi(2S)) = 14.5 \pm 0.7$, and in quite good agreement with the result reported by Belle in [5]: $\sigma(\psi(2S)) = (15.42 \pm 0.12 \pm 0.89)$ pb Anyway we can conclude that our selection and fit procedure are working properly.

Fit validation with toy Monte Carlo.

We performed toy MC studies to test if the fit procedure will work also on the Y(4260) signal region with the expected number of signal and background events.

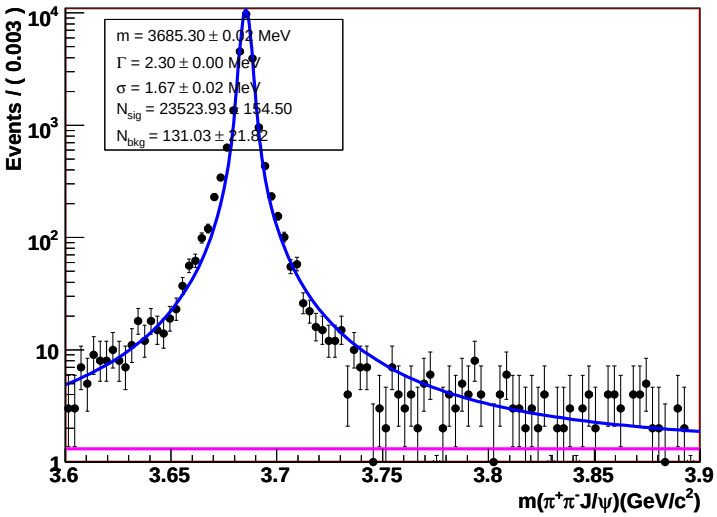

(a) Fit to $\psi(2S)$ data with a Voigtian

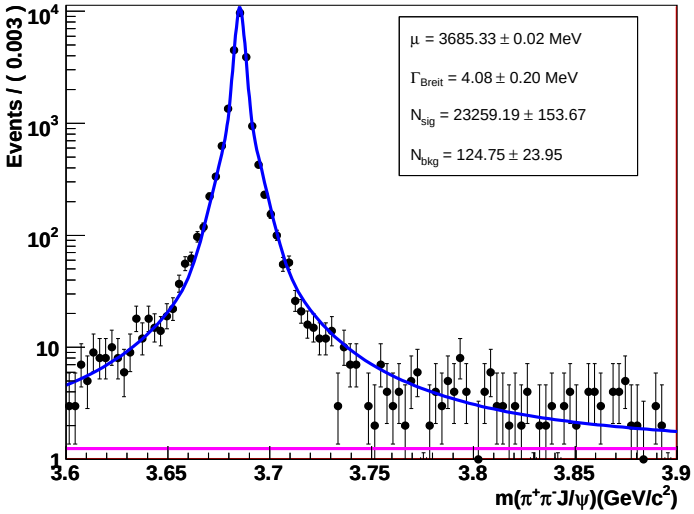

(b) Fit to $\psi(2S)$ data with a Breith-Wigner convoluted with a double goussian

Figure 4.17: Unbinned maximum likelihood fit to $m(J/\psi\pi^+\pi^-)$ with various PDFs. The black points are the data, the blue line is the signal PDF, the purple line is background PDF.

We estimate the number background events from what we called $\psi(2S)$ sideband in the optimization section (i.e. $m(J/\psi\pi^+\pi^-)$ [3.8-4.2] GeV/c^2) and the signal events from the previous Babar analysis scaled by the luminosity and the different efficiency. In the region between 4 and 5 GeV/c^2 we expect to have about 850 background events and around 250 $Y(4260)$ events.
One thousand experiments have been generated with such numbers of signal and background events: the background PDF has been taken from the a fit to the $m(J/\psi\pi^+\pi^-)$ distribution in the $\psi(2S)$ sideband region and the signal PDF is a Voigtian function with mass equal to 4.260 GeV/c^2, width 90 GeV/c and resolution fixed to the value find from the fit to the $\psi(2S)$ data. To evaluate the goodness of the fit, the significance is calculated as $\sqrt{-2\ln(\mathcal{L}_0/\mathcal{L}_{max})}$, where $\mathcal{L}_{max}$ and $\mathcal{L}_0$ is the maximum likelihood returned by the fit and by a null signal fit. The $m(J/\psi\pi^+\pi^-)$ distribution of each experiment has been fitted, with a P1+Voigtian PDF with floating mass and width. to evaluate the number of signal events, the resonance mass and width and the significance of the signal. Figure 4.18 shows some example of the fit to some experiments while 4.19 show the distributions for the number of signal events, mass, width and significance of all the one thousand experiment. So the fit for the $Y(4260)$ is working properly and with such a background level we can aim to a $10-13\sigma$ signal. Pull distributions for mass, width number of signal and background events are shown in Fig 4.20.

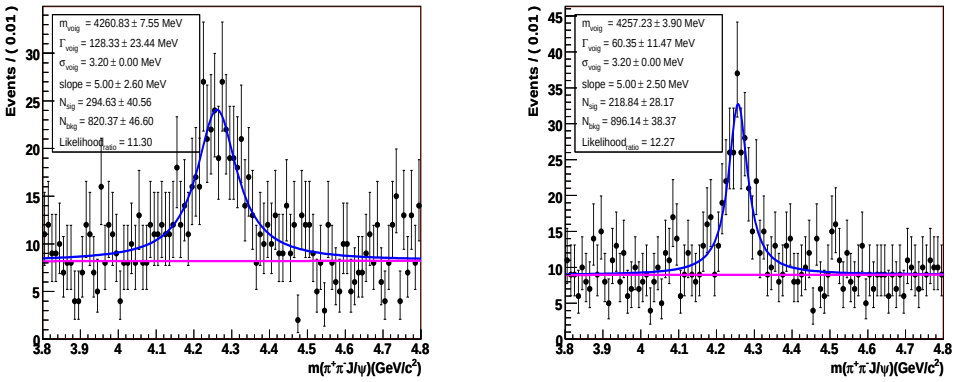

(a) (b)

Figure 4.18: Examples of Maximum Likelihood fit to toy MC experiments with 250 $Y(4260)$ signal events and 850 background events.

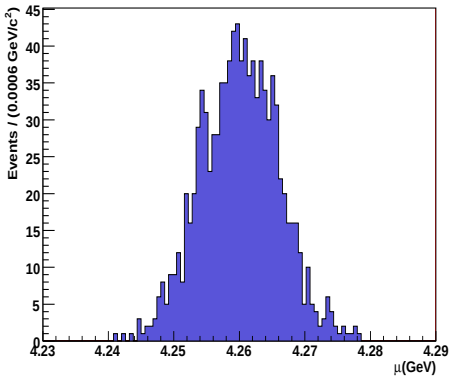

(a) Fit output: $Y(4260)$ mass.

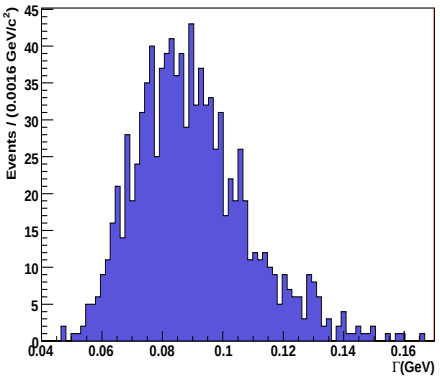

(b) Fit output: $Y(4260)$ width.

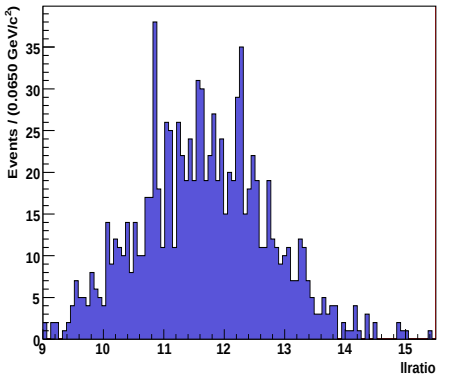

(c) Fit output: significance (number of σ).

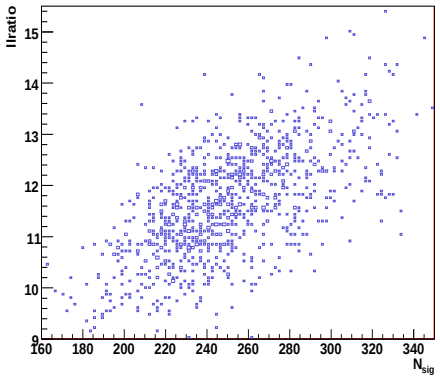

(d) Fit output: significance versus number of signal events found by the fit.

Figure 4.19: Results of one thousand toy MC experiments at the $Y(4260)$ with 850 background events and 250 signal events.

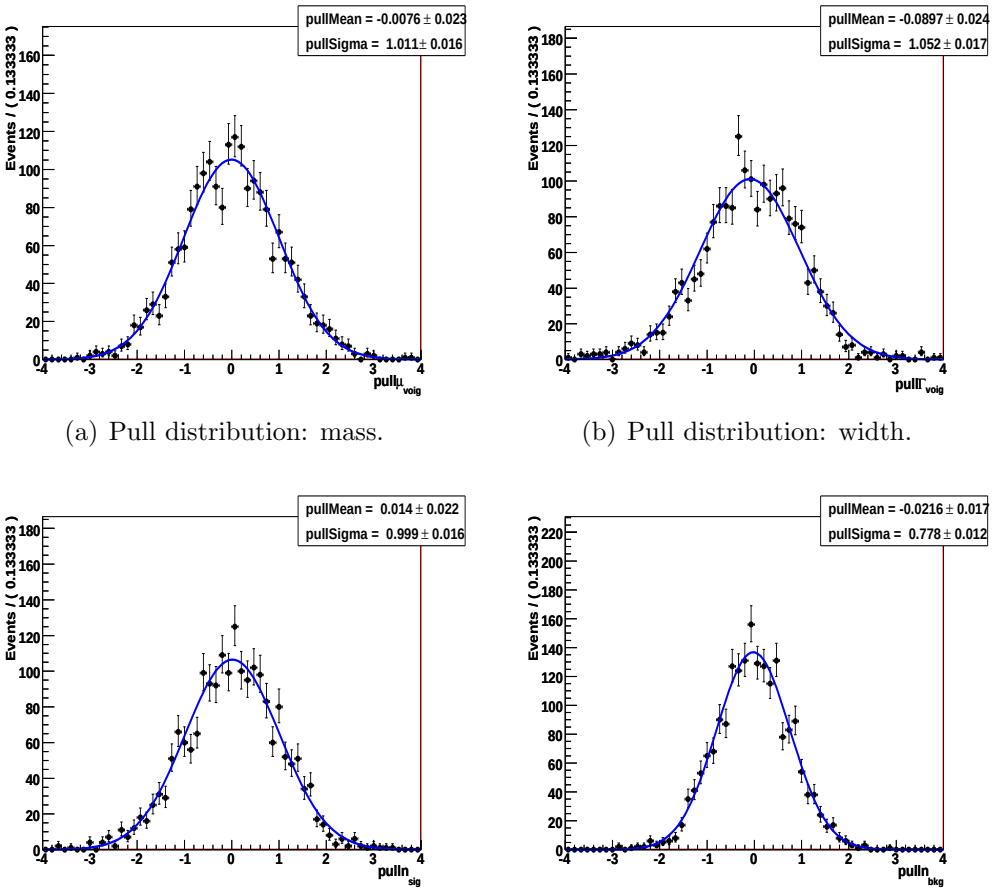

(a) Pull distribution: mass.

(b) Pull distribution: width.

(c) Pull distribution: number of signal events.

(d) Pull distribution: number of background events.

Figure 4.20: Pull distribution of some of the variables used in the Voigtian + linear background fit.

4.5 Study of the $J/\psi\pi^+\pi^-$ mass spectrum

4.5.1 Study of resonance lineshape

In the fits of the previous section a non-Relativistic Breit-Wigner was adapted, and phase space factor was not taken into account as well as the other corrections that may distort the resonance line-shape. These contribution are not included in the M.C. therefore they have been neglected so far. The mass dependence in a resonance line-shape in ISR production is attribute to:

- Breit-Wigner shape;
- energy dependance of the e^+e^- annihilation rate: proportional to $1/s = 1/m^2$;
- mass dependance of the ISR emission PDF $W(s,x) \times |dx/dm| = W(s, 1 - m^2/s) \times 2m/s$;
- mass dependence phase space factor;
- mass dependence of the efficiency: in our case is the efficiency increases linearly with the mass.

The first two factor decrease with the mass above the resonance mass, while the other three factors increase with the mass.

Phase-space factor

One general expression for n-body decay is

$$d\Gamma = \frac{(2\pi)^4}{2M}|\mathcal{M}|^2 d\Phi_n(P; p_1, \cdots, p_n) \tag{4.7}$$

where

$$d\Phi_n(P; p_1, \cdots, p_n) = \delta^4\big(P - \sum_i p_i\big) \prod_i \frac{d^3 p_i}{(2\pi)^3 2E_i} \tag{4.8}$$

We can get for a 3-body decay

$$d\Gamma = \frac{1}{(2\pi)^5}\frac{1}{16M^2}|\mathcal{M}|^2 |p_1^*|\,|p_3|\,dm_{12}\,d\Omega_1^*\,d\Omega_3 \tag{4.9}$$

where p_1^* is the momentum of particle-1 in the rest frame of particles $(1,2)$ system whose invariant mass is m_{12}. Assuming isotropic decay and a constant interaction matrix $\mathcal{M}$, the phase space factor is an integral of $d\Gamma$ over m_{12}, which is $m_{\pi^+\pi^-}$ for our case $Y \to J/\psi\pi^+\pi^-$.

Interference between two resonances

In general there would be an interference for two resonances with same quantum number and with the same final states. The full PDF function for two resonances can be written in

$$PDF = \left| c_1 \cdot BW(m; m_1, \Gamma_1) \sqrt{\frac{PS(m)}{PS(m_1)}} + c_2 \cdot BW(m; m_2, \Gamma_2) \sqrt{\frac{PS(m)}{PS(m_2)}} \times e^{i\phi} \right|^2 \tag{4.10}$$

where $BW(m; m_n, \Gamma_n) = m_n \Gamma_n / (m^2 - m_n^2 + i\, m_n \Gamma_n)$, $PS(m)$ is the phase space factor, and $c_n = \sqrt{N_n/\Gamma_n}$ with N_n being the number of signal events. When fitting with 2 or more resonances an interference term will be taken into account.

4.5.2 Validation of the analysis on Run 1 to Run 4 data

We first unblind the Y(4260) region for the Run 1 to Run 4 data in order to validate our analysis with the same amount of luminosity of the old one. Fig. 4.21 shows our fit to the data with the PDF described at the beginning of this section + linear background. The results are summarized in Table 4.6 and compared with the old analysis and with Belle's most recent results based on 548 fb^{-1} [5]. Our fit for the Y(4260) is quite in agreement with both the other measurements, while no evidence of the broad state around 4 GeV/c^2 claimed by Belle can be seen in the Run 1-4 data.

Table 4.6: Summary of Run 1 to Run 4 validation

	Run 1-4 data	Old analysis	Belle's results [5]
Mass (MeV/c^2)	4235 ± 4	$4259 \pm 8\ ^{+2}_{-6}$	$4247 \pm 12\ ^{+17}_{-32}$
Width (MeV/c^2)	54 ± 14	$88 \pm 23\ ^{+6}_{-4}$	$108 \pm 19 \pm 10$
N_{sig}	147 ± 22	131 ± 21	324 ± 21
N_{bkg}/ GeV/c^2	342 ± 28	322 ± 18	-

4.6 Unblind the full dataset

The Y(4260)

In figure 4.22 we show the $J/\psi\pi^+\pi^-$ mass spectrum for the Run1-4 and Run5-6: the total number of events scaled by the luminosity is consistent within the two datasets, see also Table 4.7.

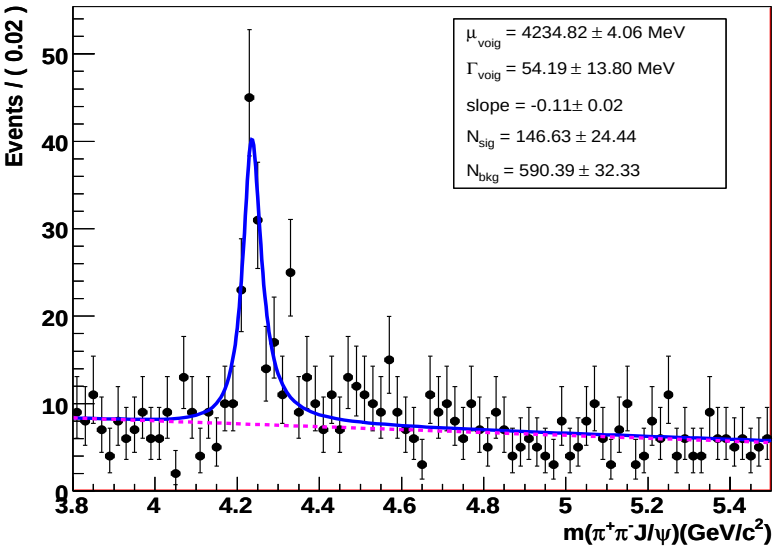

Figure 4.21: Invariant mass distribution of the $J/\psi\pi^+\pi^-$ candidates between 3.8 and 5 GeV/c^2 for Run 1 to Run 4 data. Dots are the data, the blue line is the signal PDF fit and the purple line is the linear fit to the background.

Table 4.7: Events number for different datasets.

	Run 1-4 data	Run 5-6	Run 1-6
N events	653	583	1236
Luminosity (/fb)	236	218	545
Ratio (ev/lumi)	2.77	2.67	2.72

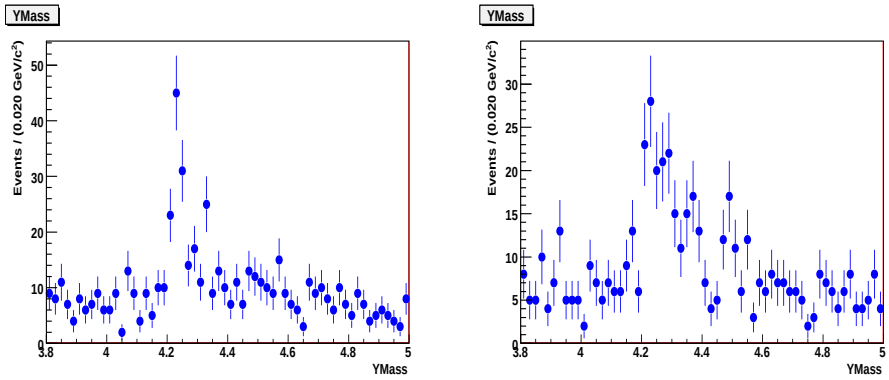

(a) $J/\psi\pi^+\pi^-$ mass spectrum for the Run1-4

(b) $J/\psi\pi^+\pi^-$ mass spectrum for the Run5-6

Figure 4.22: $J/\psi\pi^+\pi^-$ invariant mass distribution for Run1-4 and Run5-6.

We breakdown the full dataset in four parts: run1-3, run4, run5 and run6 and fit them separately. Fig. 4.23 report the fit results: some spread of the resonance parameters can be observed, but on average there's good agreement within the different datasets.

As additional check we plot the $J/\psi\pi^+\pi^-$ invariant mass distribution for $J/\psi\to e^+e^-$ and $J/\psi\to\mu^+\mu^-$ respectively: no particular differences can be observed between the two distributions as shown in Fig. 4.24.

For a background evaluation as mentioned before we use the J/ψ sidebands as mentioned before.

For the full dataset we first report a fit done using a single resonance hypothesis to be compared with the results of the old BaBar analysis and with BELLE results, the fit outputs are shown in Fig. 4.25 and summarized in table 4.8, the agreement within the different analysis is good, nevertheless the quality of the fit of Fig. 4.25 is still poor and the signal PDF cannot describe the data properly. Therefor, we fit the $J/\psi\pi^+\pi^-$ mass spectrum under different hypothesis, adding to the signal PDF the other new states found by BaBar and BELLE either in $J/\psi\pi^+\pi^-$ and in $\pi^+\pi^-\psi(2S)$ and an additional B-W to describe the bump we see around $4.5\,\mathrm{GeV}/c^2$.

Among the many different combination we took into account here we report the following five hypothesis:

- **H1:** one resonance: Y(4260);
- **H2:** Y(4260) + the bump around $4.5\,\mathrm{GeV}/c^2$;

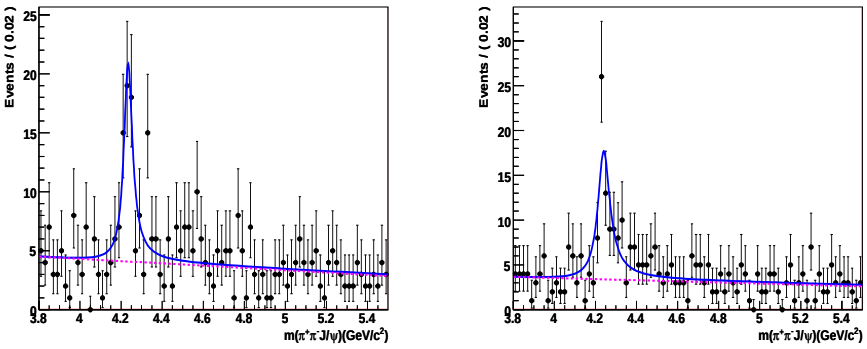

(a) $J/\psi\pi^+\pi^-$ mass spectrum for the Run1-3

(b) $J/\psi\pi^+\pi^-$ mass spectrum for the Run4

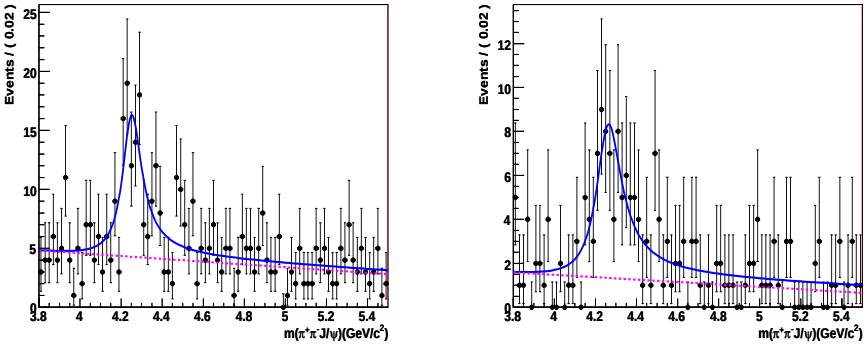

(c) $J/\psi\pi^+\pi^-$ mass spectrum for the Run5

(d) $J/\psi\pi^+\pi^-$ mass spectrum for the Run6

Figure 4.23: Fit to the $J/\psi\pi^+\pi^-$ invariant mass distribution for different datasets.

Table 4.8: Summary of run 1-6 results with one resonance hypothesis.

	Run 1-6 data	Old analysis	Belle's results [5]
Mass (MeV/c^2)	4242 ± 5	4259 ± 8 $^{+2}_{-6}$	4247 ± 12 $^{+17}_{-32}$
Width (MeV/c^2)	108 ± 18	88 ± 23 $^{+6}_{-4}$	108 ± 19 ± 10
N_{sig}	395 ± 49	131 ± 21	324 ± 21
$N_{bkg}/gevcc$	545 ± 32	322 ± 18	-
Luminosity (/fb)	454	232	548
Significance	15 σ	8.2 σ	$> 15\sigma$

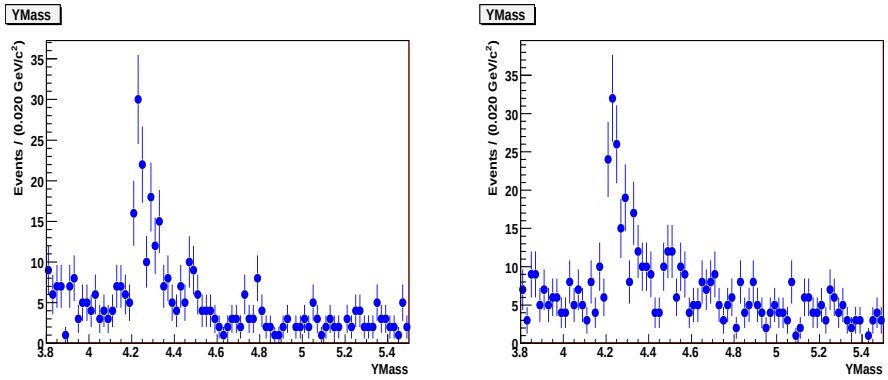

(a) $J/\psi\to e^+e^-$ (b) $J/\psi\to\mu^+\mu^-$

Figure 4.24: $J/\psi\pi^+\pi^-$ invariant mass distribution for $J/\psi\to e^+e^-$ and $J/\psi\to\mu^+\mu^-$.

- **H3:** Y(4260) + Y(4330);
- **H4:** Y(4260) + Y(4330) + the bump around 4.5 GeV/c^2;
- **H5:** Y(4260) + Y(4330) + the bump around 4.5 GeV/c^2 + Y(4008) + Y(4660);

χ^2/dof are reported in table 4.9 for the different hypothesis, while the fits to the data are shown in Fig. 4.25 and 4.26. When using hypothesis H5, no significant evidence of the resonances Y(4008) and Y(4660) is found. Therefore we use hypothesis H4 to extract the resonance parameters summarized in table, 4.10. The significance has been evaluated from $\sqrt{-2ln(L_{max}/L_0)}$ where L_{max} and L_0 are the maximum likelihood returned by the fit and the null hypothesis.

Table 4.9: χ^2/dof in the interval [4.0-4.6] GeV/c^2 for different hypothesis.

Hypothesis	χ^2/dof (10 MeV/c^2 bin)
H1	1.34
H2	1.23
H3	1.21
H4	1.15
H5	0.87

Then we use equation 4.11 to extract the the product $\mathcal{B}(Y\to\pi^+\pi^- J/\psi)\cdot\Gamma_{Y\to e^+e^-}$ for Y(4260), Y(4350) and Y(4500) and the upper limits at 90% C.L. on the Y(4008) and Y(4660). The upper limits have been calculated by looking at the point where

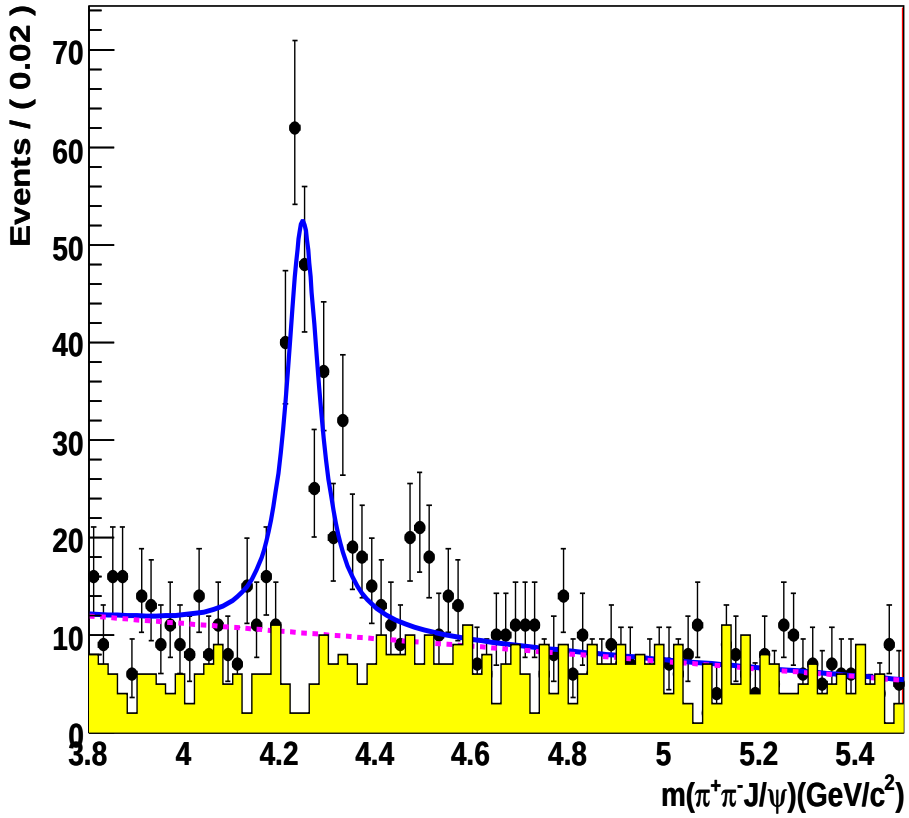

Figure 4.25: Invariant mass distribution of the $J/\psi\pi^+\pi^-$ candidates between 3.8 and 5 GeV/c^2 for Run 1 to Run 6 data. Dots are the data, the blue line is the signal PDF fit and the purple line is the linear fit to the background. (The background from the J/ψ sidebands is the yellow histograms)

Table 4.10: Resonances parameters for the fit with H5 hypothesis - Statistical significance only.

Resonance	mass (MeV/c^2)	width (MeV/c^2)	n. of events	significance (σ)
Y(4260)	4242 ± 5	61 ± 11	238 ± 33	15.2
Y(4350)	4360 (fixed)	75 (fixed)	72 ± 20	4.5
Y(4500)	4489 ± 8	41 ± 23	53 ± 20	4.2

the logarithm of the likelihood exceeds the value of the minimum of by 1.35, corresponding to a yield of 44 and 33 respectively. The selection efficiencies at values of $J/\psi\pi^+\pi^-$ mass greater than 4350 MeV/c^2 have been linearly extrapolated from the MC samples is has been studied. For the final result it has been decided to fit with two different fit hypothesis, H2 and H4 since with our present statistics both are favored with the same χ^2. In the next section the final result is presented.

Table 4.11: BR

Resonance	$\mathcal{B}(Y\to\pi^+\pi^- J/\psi)\cdot\Gamma_{Y\to e^+e^-}$
Y(4008)	<0.31 eV at 90% C.L.
Y(4260)	6.64 ± 0.75 eV
Y(4350)	< 0.70 eV
Y(4500)	1.3 ± 0.6 eV
Y(4660)	<0.63 eV at 90% C.L.

Table 4.12: Y(4260) parameters for different analysis.

Analysis	mass (MeV/c^2)	width (MeV/c^2)
BaBar (old analysis)	$4259 \pm 8^{+2}_{-6}$	$88 \pm 23^{+6}_{-4}$
BELLE	$4247 \pm 12^{+17}_{-32}$	$108 \pm 19 \pm 10$
BaBar new (H1)	4242 ±5	108 ±18
BaBar new (H2)	4246 ±5	75 ±14
BaBar new (H4)	4242 ± 5	61 ± 11

Di-pion invariant mass

Fig 4.27 shows the distribution of the di-pion invariant mass for the $J/\psi\pi^+\pi^-$ candidate below the Y(4260) peak (i.e. between 4.1 GeV/c^2 and 4.4 GeV/c^2) in green and on the Y(4260) side bands (i.e. [3.95-4.1] GeV/c^2 and [4.4-4.55] GeV/c^2) in red: the enhancement a little bit below the $f^0(980)$ mass is evident.

We obtain the di-pion invariant mass distribution for the Y(4260) with the sidebands subtraction: the structure shown in 4.28 is similar to the one reported by Belle in [5].

Another way to obtain the di-pion invariant mass distribution for Y(4260) events is perform a scan of the final state invariant mass cutting on different regions (100 MeV/c^2 wide) of the di-pion mass and fit the $J/\psi\pi^+\pi^-$ spectrum with the

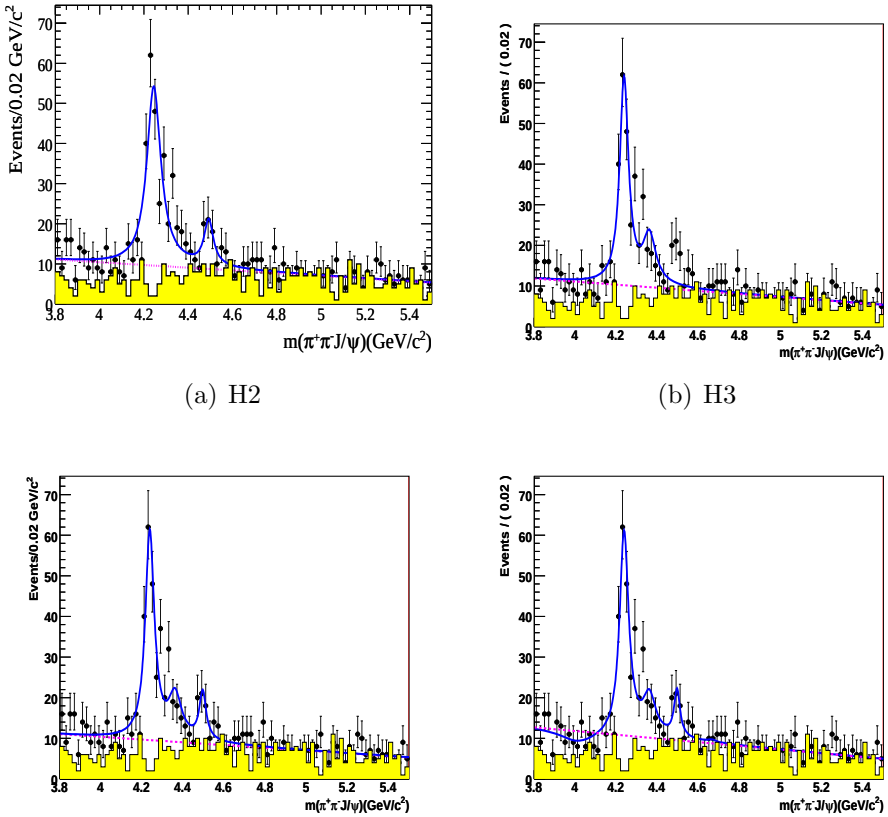

(a) H2 (b) H3

(c) H4 (d) H5

Figure 4.26: Fit to the $J/\psi\pi^+\pi^-$ invariant mass distribution for different hypothesis. (The background from the J/ψ sidebands is the yellow histograms)

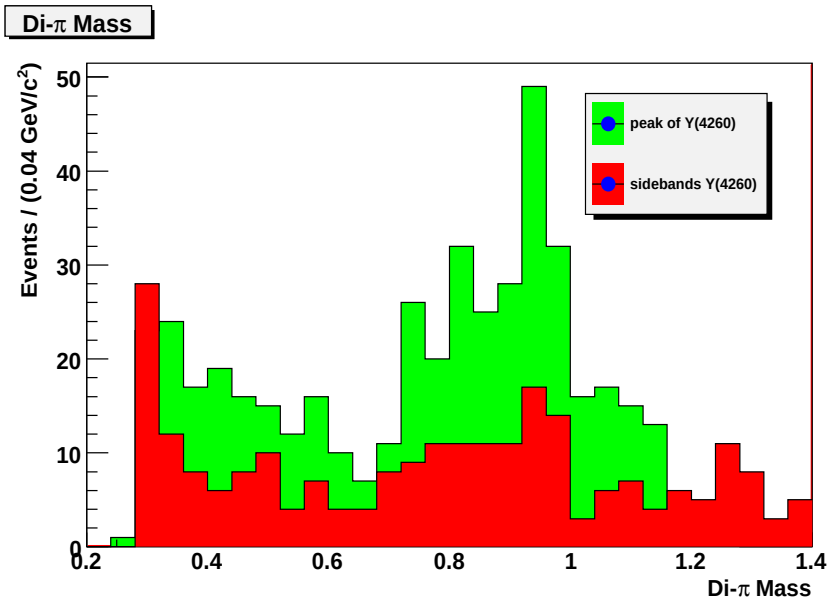

Figure 4.27: The di-pion invariant mass distribution for events under the Y(4260) peak (green) and sideband (red).

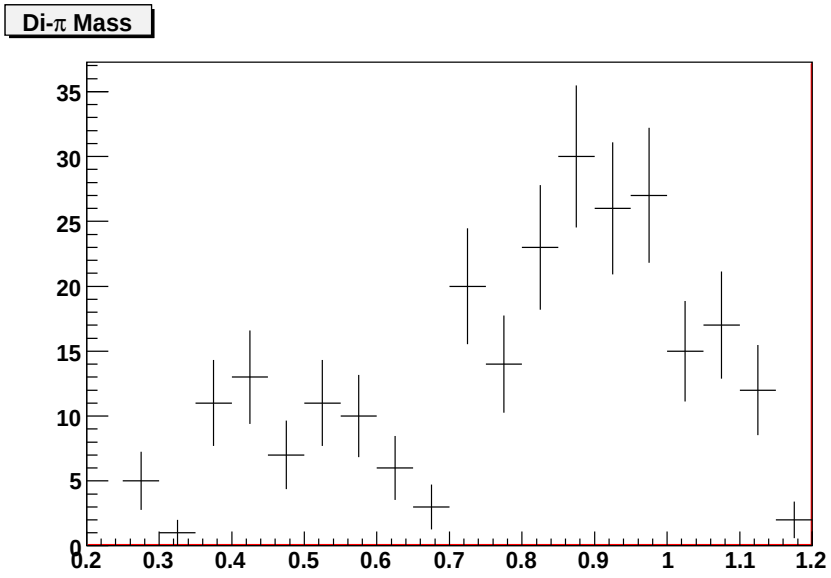

Figure 4.28: The di-pion invariant mass distribution for Y(4260) events with sidebands subtraction.

Y(4260) signal PDF fixing mass and width to the Y(4260) PDG value and leaving floating the number of events (see Fig. 4.29). In figure 4.30 we plot the number of signal events found by the previous fits versus the cut applied on the di-pion mass and we have a distribution which is consistent with the one found with the sideband subtraction.

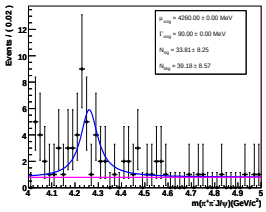

(a) Di-pion mass interval: 0.3 - 0.4 GeV/c^2

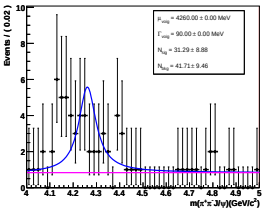

(b) Di-pion mass interval: 0.4 - 0.5 GeV/c^2

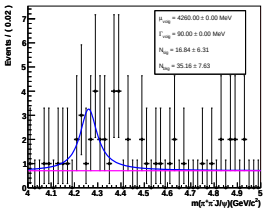

(c) Di-pion mass interval: 0.5 - 0.6 GeV/c^2

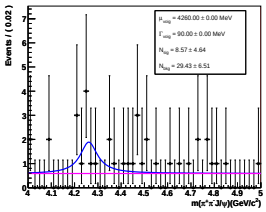

(d) Di-pion mass interval: 0.6 - 0.7 GeV/c^2

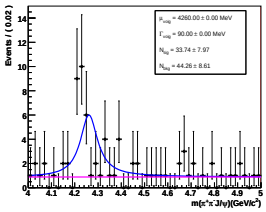

(e) Di-pion mass interval: 0.7 - 0.8 GeV/c^2

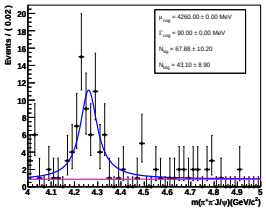

(f) Di-pion mass interval: 0.8 - 0.9 GeV/c^2

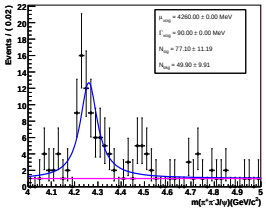

(g) Di-pion mass interval: 0.9 - 1.0 GeV/c^2

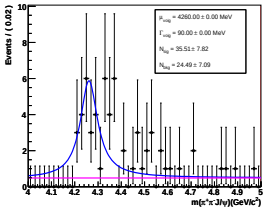

(h) Di-pion mass interval: 1.0 - 1.1 GeV/c^2

Figure 4.29: Fit to the $J/\psi\pi^+\pi^-$ invariant mass distribution for different values of the di-pion mass.

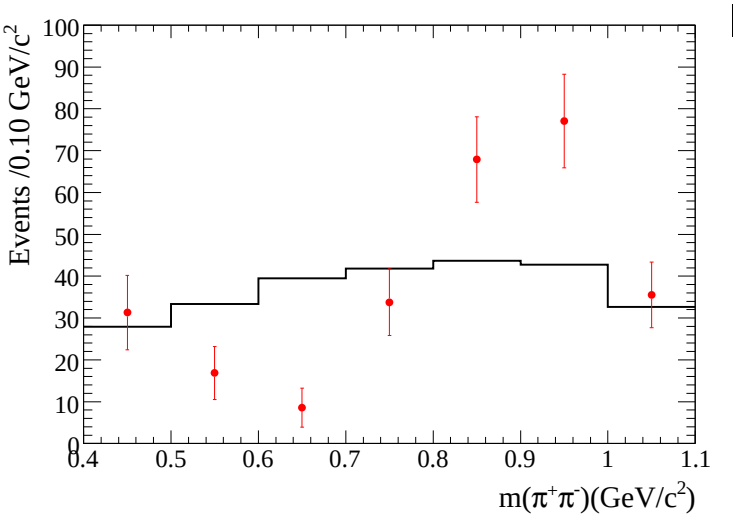

Figure 4.30: $\pi^+\pi^-$ invariant mass spectrum for $Y(4260)$ events (dots) from the fits shown in 4.29. (Number of events found by the fit versus the cut on the di-pion invariant mass). The black histogram refers to the phase space hypothesis from MC.

4.7 Systematic errors

Systematics errors will be evaluated for the measurement of the $\Gamma_{Y\to e^+e^-} \times \mathcal{B}_{Y\to J/\psi\pi^+\pi^-}$ $\Gamma_{V\to ee}\mathcal{B}_{\pi^+\pi^-}(Y))$, mass and width of a broad resonance. Main sources of systematics are listed below and summarized in table 4.14:

Systematics due to the fit procedure

The systematic uncertainties for the fit are evaluated by changing the fit range, background PDF and adding a X(3872) PDF to the fit. They are listed in table 4.13

Systematics from the selection

The uncertainty of the selection efficiency arises from the model dependence in generation in $Y\to J/\psi\pi^+\pi^-$ decay and the uncertainty of the Y width. From the $\psi(2S)$ Monte Carlo we estimate the model dependence systematics to be around 10.87% and the uncertainty coming from the Y width 1.6%. All in all 11%.

Table 4.13: Systematic errors due to the fit procedure.

Fitting condition	Variation of N(Signal)	Variation (MeV/c^2) of Mass	Variation (MeV/c^2) of Width
Pol2 Bkg	-1 %	-0.25	-1.2
Pol3 Bkg	-2.4 %	-1.0	-3.3
other Bkg. changes	2.0 %	0.1	+1.9
Fit Range [3.79,5.5]GeV/c^2	-1.5 %	-0.5	-3.2
Fit Range [3.9,4.9]GeV/c^2	-3.0 %	-1.5	-2.5
Incl. $X(3872)$	+3.0	0.7	2.78
Sum	$^{+7.2}_{-2.8}$ %	$^{+1.9}_{-5.7}$	$^{+6.3}_{-4.3}$

Mass shift

There is a mass shift of between our fit at the $\psi(2S)$ and the PDG value we will add it as systematic error to the mass measurement.

Mass resolution and mass calibration

We quote 1.5 MeV/c^2 error in the width measurement due to difference resolution between data and Monte Carlo and to take into account the different resolution at the Y(4260) energy with respect to the $\psi(2S)$.

Then we account 1.5 MeV/c^2 of mass calibration arising from the difference between the generated and fitted mass for our Monte Carlo samples.

Measurement of the $\Gamma_{Y\to e^+e^-} \times \mathcal{B}_{Y\to J/\psi\pi^+\pi^-}$

We will use Equation 4.5 to determine $\mathcal{B}(V\to J/\psi\pi^+\pi^-)$ for a resonance with a known $\Gamma_{V\to e^+e^-}$, or the product of $\mathcal{B}(V\to J/\psi\pi^+\pi^-)$ and $\Gamma_{V\to e^+e^-}$ for a resonance with an unknown $\Gamma_{V\to e^+e^-}$. Using Eq. 4.5, we can get the ratio of $\Gamma_{V\to ee}\,\mathcal{B}(V\to J/\psi\pi^+\pi^-)$ between the Y and the $\psi(2S)$:

$$\frac{\Gamma_{ee}(Y)\mathcal{B}(Y\to J/\psi\pi^+\pi^-)}{\Gamma_{ee}(\psi(2S))\mathcal{B}(\psi(2S)\to J/\psi\pi^+\pi^-)} = \Big(\frac{N(\gamma\, Y)}{N(\gamma\,\psi(2S))}\Big)\cdot\Big(\frac{m(Y)}{m(\psi(2S))}\Big)\cdot\Big(\frac{\varepsilon(\psi(2S))}{\varepsilon(Y)}\Big)\cdot\Big(\frac{W(s,x_{\psi(2S)})}{W(s,x_Y)}\Big) \quad (4.11)$$

In this way, the whole uncertainties of integrated luminosity and $\mathcal{B}(J/\psi\to\ell^+\ell^-)$ are canceled. Most uncertainties of the selection efficiency, PID efficiency, tracking

efficiency, and photon emission probability density $W(s,x)$ are canceled out. Meanwhile, we also introduce some new uncertainties pertaining to the ISR $\psi(2S)$ such as $\mathcal{B}(\psi(2S)\to J/\psi\pi^+\pi^-)$, $\Gamma_{\psi(2S)\to e^+e^-}$, and statistical uncertainty of the $N(\psi(2S))$.

Table 4.14: Summary of systematic errors that will affect $\Gamma_{Y(4260)\to e^+e^-}\times\mathcal{B}_{Y(4260)\to J/\psi\pi^+\pi^-}$ (denoted as $\Gamma_{V\to ee}\mathcal{B}_{\pi^+\pi^-}(Y)$), mass and width due to the fit procedure, selection efficiency, resolution uncertainty and mass calibration.

Source	Variation of $\Gamma_{V\to ee}\mathcal{B}_{\pi^+\pi^-}(Y)$	Variation of Mass	Variation of Width
Fit procedure	$^{+3.6}_{-4.2}\%$	$^{+0.71}_{-1.89}$	$^{+3.37}_{-5.4}$
Selection	$\pm 11\%$		
Mass calibration		± 1.5	
Resolution uncertainty			± 1.5
Mass shift		0.77	
$\Gamma_{ee}(\psi(2S))\mathcal{B}(\psi(2S)\to J/\psi\pi^+\pi^-)$	± 2.6		
Sum	$^{+11.86}_{-12.06}\%$	$^{+1.83}_{-2.41}$	$^{+3.69}_{-5.6}$

Chapter 5

Conclusions

It has been performed an unbinned maximum likelihood fit to the $J/\psi\pi^+\pi^-$ invariant mass distribution between $3.8\,\mathrm{GeV}/c^2$ and $5.5\,\mathrm{GeV}/c^2$ using the full *BABAR* data sample ($454\ fb^{-1}$). The signal probability density function (PDF) is a relativistic Breit-Wigner function convolved with a Gaussian resolution function. A first-order polynomial function is used to describe the background. All the fit parameters for the signal and the background PDF are free, except the Gaussian resolution which is fixed to the value corresponding to the resolution observed at the $\psi(2S)$ in data ($4.3\,\mathrm{MeV}/c^2$), but linearly scaled to the $Y(4260)$ mass ($5\,\mathrm{MeV}/c^2$). To get a better description of the observed invariant mass distribution, a second relativistic Breit-Wigner function has been added centered around $4.5\,\mathrm{GeV}/c^2$.

The results obtained using this model are shown in Fig. 5.1. The obtained parameters for the Y(4260) state are: $m_Y = 4246 \pm 5^{+3}_{-2}\,\mathrm{MeV}/c^2$ and $\Gamma_Y = 75 \pm 14^{+3}_{-4}\,\mathrm{MeV}$, where the first error is statical and the second one is systematic. For the structure around 4500 MeV/c^2 we obtain $m_Y = 4492 \pm 10^{+4}_{-2}\,\mathrm{MeV}/c^2$ and $\Gamma_Y = 63 \pm 24^{+24}_{-12}\,\mathrm{MeV}$. If the interference between the two states is included in the model, the fit does not converge to a stable solution because of the low statistic. Therefore we neglect a possible interference between the two states in this analysis. We also compute the statistical significance of the two states using the difference between the likelihood for the full model and the likelihood for a model assuming zero events, using the expression $\sqrt{-2\log\Delta L}$. We get a significance greater than 15σ for the $Y(4260)$ and 4.7 σ for the $Y(4500)$.

Using Monte-Carlo simulations we find that the selection efficiencies ε vary linearly with the $J/\psi\pi^+\pi^-$ mass. The number of events simulated for each sample is sufficiently large to keep the statistical error below 1% (Table 5.1). The selection efficiency depend also on the $\pi^+\pi^-$ invariant mass distribution. For the $Y(4260)$ the

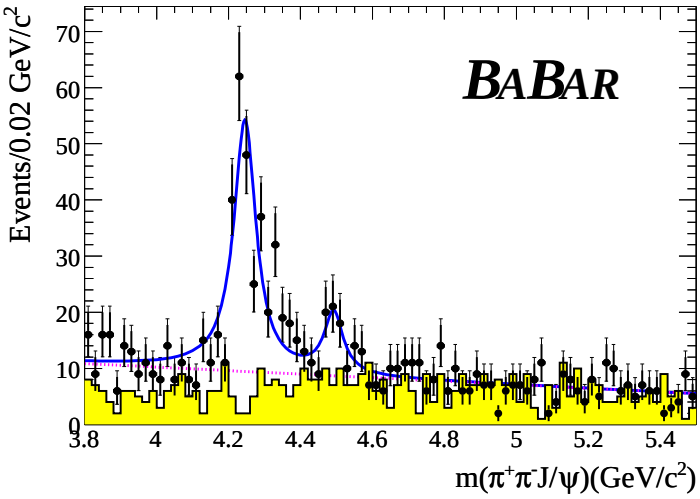

Figure 5.1: $J/\psi\pi^+\pi^-$ invariant mass spectrum for selected events in the mass range between 3.8 GeV/c^2 and 5.5 GeV/c^2. The background contribution is shown by the dotted line. The shaded histogram shows the expected background from the J/ψ sidebands.

number of events is sufficiently high to allow the measurement of this distribution, therefore ϵ is calculated taking into account the observed distribution. These efficiency values are used to compute the product of the decay width to e^+e^- multiplied by the branching fraction to $J/\psi\pi^+\pi^-$ ($\mathcal{B}(J/\psi\pi^+\pi^-)\Gamma_{e^+e^-}$) for each state analyzed.

In the model used to reproduce the observed distribution, we check for possible signals from all the $J^{PC} = 1^{--}$ states known in this region. To do this, we include possible contributions from $Y(4008)$, $Y(4360)$ and $Y(4660)$ in the model used to describe the observed data. Their masses and widths are fixed to the values measured in previous analyses [73, 75, 76]. We do not observe contributions from these states, and so we state upper limits. The efficiencies and the results are summarized in Table 5.1. To measure $\mathcal{B}(J/\psi\pi^+\pi^-)\Gamma_{e^+e^-}$ we compare the results for each state with that obtained for the $\psi(2S)$, using:

$$\frac{\Gamma_{ee}(Y)\mathcal{B}(Y\to J/\psi\pi^+\pi^-)}{\Gamma_{ee}(\psi(2S))\mathcal{B}(\psi(2S)\to J/\psi\pi^+\pi^-)} = \left(\frac{N_{\gamma Y}}{N_{\gamma\psi(2S)}}\right)\cdot\left(\frac{m_Y}{m_{\psi(2S)}}\right)\cdot\left(\frac{\varepsilon_{\psi(2S)}}{\varepsilon_Y}\right)\cdot\left(\frac{W_{\psi(2S)}}{W_Y}\right), \quad (5.1)$$

where $N_{\gamma\psi(2S)}$, $N_{\gamma Y}$, $m_{\psi(2S)}$, m_Y, $\varepsilon_{\psi(2S)}$, ε_Y, $W_{\psi(2S)}$ and W_Y are the numbers of

events, masses, selection efficiencies and the photon emission probability density functions for the $\psi(2S)$ for each state, as appropriate. In this way, the uncertainties of integrated luminosity and $\mathcal{B}(J/\psi \to \ell^+\ell^-)$ are entirely canceled, and most uncertainties of the selection efficiency, particle ID efficiency, tracking efficiency, and photon emission probability density $W(s,x)$ also cancel out. We introduce some new uncertainties pertaining to the ISR $\psi(2S)$ such as $\mathcal{B}(\psi(2S) \to J/\psi\pi^+\pi^-)$, $\Gamma_{\psi(2S)\to e^+e^-}$, and statistical uncertainty of the $N_{\gamma\,\psi(2S)}$.

Table 5.1: Selection efficiencies and products of the electron partial width times branching ratio to $J/\psi\pi^+\pi^-$ for 1^{--} states included in the model.

State	Efficency (%)	$\mathcal{B}(\pi^+\pi^- J/\psi)\cdot\Gamma_{e^+e^-}$ (eV)
$Y(4008)$	10.5	< 0.31 (90% C.L.)
$Y(4260)$	12.2	$6.64 \pm 0.75^{+0.3}_{-0.4}$
$Y(4360)$	12.4	< 0.70 (90% C.L.)
$Y(4500)$	13.4	$1.3 + 0.6 - 0.4^{+0.3}_{-0.2}$
$Y(4660)$	13.8	< 0.63 (90% C.L.)

These factors are also used to compute the $e^+e^- \to J/\psi\pi^+\pi^-$ cross section after background subtraction shown in Fig. 5.2. The selected data at the $\psi(2S)$ are used as a benchmark to evaluate possible systematic errors. The method used for the efficiency determination is checked at the $\psi(2S)$, where we used the efficiency value to evaluate the cross section, obtaining a result that is consistent with the measurement performed by previous experiments [73].

The $\psi(2S)$ mass is measured as $3685.35 \pm 0.02\,\mathrm{MeV}/c^2$ (statistical error only); the mass shift with respect to the PDG value [77] is taken into account as a systematic error in the $Y(4260)$ mass measurement. The Monte-Carlo simulation of the $J/\psi\pi^+\pi^-$ invariant mass resolution and mass scale have been calibrated by comparing the widths of $J/\psi\pi^+\pi^-$ invariant mass distributions from $\psi(2S)$ decays in data and Monte-Carlo events. We find that the Monte-Carlo simulation reproduces the observed resolution of the $J/\psi\pi^+\pi^-$ mass distribution for the $\psi(2S)$ state. The mass resolution is $\sim 5\,\mathrm{MeV}/c^2$ in the mass range $4.16\,\mathrm{GeV}/c^2 < m(J/\psi\pi^+\pi^-) < 4.36\,\mathrm{GeV}/c^2$

Systematic uncertainties on the measured values include contributions from the fitting procedure (evaluated by changing the fit range and the background PDF), the Monte-Carlo sample reconstructed mass differences (Δm), the mass-resolution function and the dependence on the model for the $\mathrm{Y}(4260) \to J/\psi\pi^+\pi^-$ decay. These uncertainties have been added in quadrature. The results of systematic uncertainty

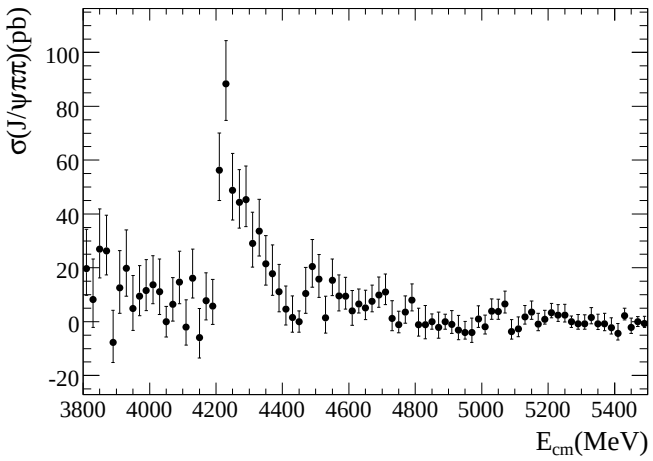

Figure 5.2: The measured $e^+e^- \to J/\psi\pi^+\pi^-$ cross section after background subtraction (error bars are only statistical.)

Table 5.2: Sources of systematic error contributions.

Source	$\mathcal{B}\cdot\Gamma_{e^+e^-}(\%)$	Mass (MeV/c^2)	Γ (MeV)
Fit procedure Y(4260)	$^{+2}_{-4}$	±1	$^{+2}_{-4}$
Fit procedure Y(4500)	$^{+19}_{-15}$	$^{+4}_{-1}$	$^{+24}_{-12}$
Mass shift	-	$+0.8$	-
MC Δm	-	±1.5	-
Mass res.	-	-	±1.5
$\mathcal{B}\cdot\Gamma_{e^+e^-}(\psi(2S))$	±2.6	-	-
MC model	±4	-	-

studies are summarized in Table 5.2. The possible $Y(4360) \to J/\psi\pi^+\pi^-$ contributions to the observed mass spectrum could have the effect of a distortion of the observed $Y(4260)$ lineshape and give a different event yield, leaving the $Y(4500)$ unaffected. Since we cannot exclude its presence, if we include the $Y(4360)$ in the model, the $Y(4260)$ parameters become $m_Y = 4242 \pm 5^{+3}_{-2}\,\mathrm{MeV}/c^2$, $\Gamma_Y = 61 \pm 11^{+3}_{-4}\,\mathrm{MeV}$, and $\mathcal{B} \times \Gamma_{e^+e^-} = 5.07 \pm 0.66 \pm 0.3\ eV$. We give two sets of parameters, instead of using the mass and width differences in the two fit hypothesis as systematic errors, to make easier the comparison of our results with other measurements.

For the $Y(4260)$ we measure the invariant mass distribution of the $\pi^+\pi^-$. To do this the total sample is divided into several dipion invariant mass regions, and in each region we count the number of $Y(4260)$ events by performing a fit of the $m(J/\psi\pi^+\pi^-)$ distribution, keeping its mass and width fixed at the measured values. The result shown in Fig. 4.30 indicates that in $Y(4260)$ decays, the $\pi^+\pi^-$ invariant mass distribution is not consistent with a simple phase space model, with the presence of a bigger contribution at large $\pi^+\pi^-$ invariant masses.

In summary, we have analyzed ISR events to study the process $e^+e^- \to J/\psi\pi^+\pi^-$ across the charmonium mass range. We observe 250 ± 27 Y(4260) events with $m_Y = 4246 \pm 5^{+3}_{-2}\,\mathrm{MeV}/c^2$ and $\Gamma_Y = 75 \pm 15^{+3}_{-4}\,\mathrm{MeV}$. For the Y(4260) region, the $\pi^+\pi^-$ invariant mass distribution, tends to peak at large values, consistent with other studies [70, 73]. There is no evidence for the broad enhancement reported by BELLE around $4.05\,\mathrm{GeV}/c^2$ [73]. We obtain an upper limit $\mathcal{B}(\pi^+\pi^- J/\psi)\Gamma_{e^+e^-} < 0.31$ eV at 90% C.L. for this state. In addition we report evidence for a new structure around $4.5\,\mathrm{GeV}/c^2$ observing $53 \pm 21^{+24}_{-17}$ events, which has the parameters: $m_Y = 4492 \pm 10\ ^{+4}_{-2}\,\mathrm{MeV}/c^2$ and $\Gamma_Y = 63 \pm 24^{+24}_{-12}\,\mathrm{MeV}$.

APPENDIX A

BABAR Tracks list

- **TaggingList:** Candidates with non-zero charge. Mass hypothesis, is assigned by the tagging algorithm.
- **ChargedTracks:** Same as Tagging List, but with pion mass hypothesis assigned.
- **CalorNeutral:** Candidates which are single EMC bumps not matched with any track. Photon mass hypothesis assigned. All single-bump neutral clusters show up in both the CalorNeutral and CalorClusterNeutral lists.
- **CalorClusterNeutral:** Candidates that are multi-bump neutral clusters or single bumps which are not part of a cluster which is matched with a track. These candidates may be embedded in charged candidates. All single-bump neutral clusters show up in both the CalorNeutral and CalorClusterNeutral lists.
- **NeutralHad:** Candidates with charge zero and no EMC information. (i.e. a neutral candidate with IFR info but has not been merged with a track or an EMC bump/cluster.)
- **SingleBumpNeutralClusters:** Single-Bump-Neutral-Clusters in the EMC.
- **GoodTracksVeryLoose:** Charged Tracks with Min Transverse Momentum: 0.0 GeV,Max Momentum: 10 GeV ,Min # of Dch Hits: 0, Min Fit Chi-Square Prob.: 0, Max DOCA (Distance of CLOSEST APPROACH) in XY plane: 1.5 cm, Min Z Doca: -10 cm, Max Z Doca: 10 cm.
- **GoodTracksLoose:** Same cuts as GoodTracksVeryLoose with Min Transverse Momentum: 0.1 GeV and Min # of Dch Hits: 12.
- **GoodPhotonLoose:** Candidates from CalorNeutral satisfying: Min Raw Energy: 0.030 GeV, Min Num of Crystals: 0, Max Lateral Moment: 0.8

BABAR Particle Identification (PID) selectors

The *BABAR* PID group provides several different types of PID selector:

- Cut-based selectors impose simple cuts on the PID variables. Different levels of selector - Loose, Tight, and so on - correspond to looser or tighter sets of cuts.
- Likelihbood selectors use the PID variables to compute Likelihood functions for different particle ID hypotheses. Different levels of selector correspond to tighter or looser cuts on the Likelihood functions. For example, the kaon likelihood selector requires that the likelihood for kaons be higher than the likelihood for pions.
- Neural network selectors use the PID variables as inputs to a neural network algorithm. Neural networks predict outcomes based on a large sample of previous examples. For PID, this means that they are given examples of how PID variables behave for different particles, and optimize the selection based on this training.

Electrons.

For electrons there are several Cut-based ("Micro") selector (eMicroNoCal, eMicroVeryLoose, eMicroLoose, eMicroTight, eMicroVeryTight) and a Likelihood ("LH") selector,PidLHElectrons. These selector use the following PID variable:

- E/p Ratio of energy deposited in the calorimeter, to track momentum.
- $Ncry$ Number of EMC crystals hit
- LAT Lateral energy distribution
- $A42$ Zernike moment
- dE/dx Energy loss in the DCH
- θ_c Cerenkov angle in the DRC
- N_γ Number of photons in DRC
- $N_{\gamma_{exp}}$ Number of photons expected
- Δ_ϕ Track-bump separation

Muons.

For muons there are several Cut-based ("Micro") selector (muMicroMinimumIonizing, muMicroVeryLoose, muMicroLoose, muMicroTight, muMicroVeryTight), a Likelihood ("LH") selector (muLikeTight) and several neural network selectors (muNNVeryLoose, muNNLoose, muNNTight, muNNVeryTight).

These selector use the following PID variable:

- $Ecand$ Energy released in the EMC.
- NL Number of IFR hit layers in a cluster
- Λ_{meas} Measured number of interaction lengths traversed.
- Δ_Λ Difference between the expected (for muons) and measured number of interaction lengths traversed.
- χ^2 fit χ^2/dof of IFR hit strips in a polynomial fit of the cluster.
- χ^2 mat χ^2/dof of the IFR hit strips in the track extrapolation.
- Tc Track continuity.
- m and σ_m Average multiplicity of hit strips per layer, and its standard deviation.

Pions.

For pions there are several Likelihood ("LH") selector (piLHVeryLoose, piLHLoose, piLHTight, piLHVeryTight).

- dE/dx Energy loss in the SVT and DCH
- θ_c Cerenkov angle in the DRC
- N_γ Number of photons in DRC
- TrkQual Track quality
- $iselectron$ Whether the track passes the LH electron selector
- $ismuon$ Whether the track passes the MicroVeryTight muon selector

Bibliography

[1] E. Swanson, *Conf. on the Intersections of Particle and Nuclear Physics (CIPANP 2006*, AIP Conf. Proc. **870**.

[2] S. Godfrey, *Proceedings of 4^{th} Int. Conf. of Flavor Physics and CP Violation 06*, eConf **C060409**, 221(2006).

[3] B. Aubert *et al.* [BaBar Collaboration], Phys. Rev. Lett. **95**, 142001 (2005).

[4] B. Aubert *et al.* [BaBar Collaboration], Phys. Rev. D **73**, 012005 (2006).

[5] C. Z. Yuan *et al.*, PRL 99, 182002 (2007)

[6] X. L. Wang *et al.*PRL 99, 142002 (2007)

[7] J.J. Aubert *et al. ,*, Phys. Rev. Lett. **33**, 1404 (1974);
J.E. Augustin *et al. ,* Phys. Rev. Lett. **33**, 1406 (1974);

[8] G.S. Abrams *et al. ,*, Phys. Rev. Lett. **33**, 1453 (1974);

[9] S.L. Glashow, J.Ilioupolos, L. Maiani, Phys. Rev. D2 1985 (1970) ;

[10] C. Amsler *et al. ,*, Phys. Letters B667, 1 (2008);

[11] E. Eichten, K. Gottfried, T. Kinoshita, K. D. Lane and T. M. Yan, Phys. Rev. D **17**, 3090 (1978) [Erratum-ibid. D **21**, 313 (1980)].

[12] W. Kwong, J. L. Rosner and C. Quigg, Ann. Rev. Nucl. Part. Sci. **37**, 325 (1987).

[13] R. McClary and N. Byers, Phys. Rev. D **28**, 1692 (1983).

[14] arXiv:hep-lat/9807028v1

[15] R. Partridge *et al.*, Phys. Rev. Lett. **45** (1980) 1150.

[16] S. K. Choi *et al.* [BELLE collaboration], Phys. Rev. Lett. **89**, 102001 (2002)

[17] S. K. Choi *et al.* [Belle Collaboration], Phys. Rev. Lett. **91**, 262001 (2003)

[18] K. Abe *et al.* [Belle Collaboration], Phys. Rev. Lett. **89**, 142001 (2002)

[19] P.Dalpiaz, in H. Poth(Ed.) Proceedings of the First LEAR Workshop, Karlsruhe, Germany,1979

[20] A. Abulencia *et al.* [CDF Collaboration], Phys. Rev. Lett. **98**, 132002 (2007)

[21] B. Aubert *et al.* [BaBar Collaboration], Phys. Rev. D **71**, 031501 (2005)

[22] K. Abe et al. [Belle Collab.], arXiv:hep-ex/0505037

[23] B. Aubert *et al.* [BABAR Collaboration], Phys. Rev. D **74**, 071101 (2006)

[24] K. Abe et al. [Belle Collab.], arXiv:hep-ex/0505038.

[25] B. Aubert *et al.* [BABAR Collaboration], Phys. Rev. D **77**, 111101 (2008)

[26] . G. Gokhroo *et al.*, Phys. Rev. Lett. **97**, 162002 (2006)

[27] B. Aubert *et al.* [BABAR Collaboration], Phys. Rev. D **77**, 011102 (2008)

[28] C. Quigg, in Proceedings of the 2004 La Thuile Rencontres Results and Perspectives in Particle Physics, edited by G. Bellettini, G. Chiarelli and M. Greco (I.N.F.N. 2004) and e-Print Archive: hep-ph/0403187; E. S. Swanson, Phys. Lett. B **598**, 197 (2004); C. Quigg, in Proceedings of the 6th International Conference on Hyperons, Charm and Beauty Hadrons, 2004, edited by N. Solomey (Elsevier 2004) and e-Print Archive: hep-ph/0407124.

[29] N. Tornqvist, Phys. Lett. B **590**, 209 (2004); M. B. Voloshin, Phys. Lett. B **579**, 316 (2004); F. Close and P. Page, Phys. Lett. B **578**, 119 (2004); C.Y. Wong, Phys. Rev. C **69**, 055202 (2004); E. Braaten and M. Kusunoki Phys. Rev. D **69**, 074005 (2004); E. Swanson, Phys. Lett. B **588**, 189 (2004).

[30] F. Close and S. Godfrey, Phys. Lett. B **574**, 210 (2003).

[31] L. Maiani, F. Piccinini, A.D. Polosa, and V. Riquer, hepph/ 0412098

[32] E. Eichten, K. Lane, and C. Quigg, Phys. Rev. Lett. **89**, 162002 (2002); T. Barnes and S. Godfrey, Phys. Rev. D **69**, 054008 (2004).

[33] B. Aubert *et al.* [BABAR Collaboration], Phys. Rev. Lett. **95**, 142001 (2005)

[34] Q. He *et al.* [CLEO Collaboration], Phys. Rev. D **74**, 091104 (2006)

[35] T. E. Coan *et al.* [CLEO Collaboration], Phys. Rev. Lett. **96**, 162003 (2006)

[36] C. Z. Yuan *et al.* [Belle Collaboration], Phys. Rev. Lett. **99**, 182004 (2007)

[37] B. Aubert *et al.* [BABAR Collaboration], arXiv:0710.1371[hep-ex]

[38] B. Aubert *et al.* [BABAR Collaboration], Phys. Rev. D **74**, 091103 (2006)

[39] B. Aubert *et al.* [BABAR Collaboration], Phys. Rev. D **73**, 012005 (2006)

[40] B. Aubert *et al.* [BABAR Collaboration], Phys. Rev. D **73**, 011101 (2006)

[41] B. Aubert *et al.* [BABAR Collaboration], Phys. Rev. Lett. **98**, 212001 (2007)

[42] X. L. Wang *et al.* [Belle Collaboration], Phys. Rev. Lett. **99**, 142002 (2007)

[43] C. Amsler et al. (Particle Data Group), Phys. Lett. **B**667, 1 (2008)

[44] S. L. Zhu, Phys. Lett. B **625**, 212 (2005)

[45] Yu. S. Kalashnikova and A. V. Nefediev, Phys. Rev. D **77**, 054025 (2008)

[46] L. Maiani, V. Riquer, F. Piccinini and A. D. Polosa, Phys. Rev. D **72**, 031502 (2005)

[47] L. Maiani, F. Piccinini, A. D. Polosa and V. Riquer, Phys. Rev. Lett. **93**, 212002 (2004)

[48] L. Maiani, F. Piccinini, A. D. Polosa and V. Riquer, Phys. Rev. D **71**, 014028 (2005)

[49] C. F. Qiao, J. Phys. G **35**, 075008 (2008)

[50] K. Abe *et al.* [Belle Collaboration], Phys. Rev. Lett. **100**, 142001 (2008)

[51] C. F. Qiao, Phys. Lett. B **639**, 263 (2006)

[52] E. Fermi and C. N. Yang, Phys. Rev. **76**, 1739 (1949).

[53] PEP-II Conceptual Design Report, SLAC-R-418 (1993).

[54] *BABAR* Collaboration, B. Aubert *et al.* ,, Phys. Rev. D **69**, 071101 (2004);

[55] *BABAR* Collaboration, B. Aubert *et al.* , Nucl. Instrum. Methods Phys. Res., Sect. A**479**, 117 (2002).

[56] I. Adam *et al.* [BABAR-DIRC Collaboration], Nucl. Instrum. Meth. A **538** (2005) 281.

[57] D. Boutigny *et al.* [BABAR Collaboration], "BaBar technical design report", chapter 7

[58] X. C. Lou, T. Benninger and W. M. Dunwoodie, "Physics with the initial state radiation events at B-factory experiments", Nuclear Physics **A675**, 253c (2000).

[59] J. P. Alexander *et al.*, "Heavy Flavor Resonance and QED Radiative Corrections", SLAC-PUB-4501, December 1988.

[60] M. Benayoun *et al.*, "Spectroscopy at B-Factory Using Hard Photon Emission", Mod. Phys. Lett., **A14**, 2605 (1999).

[61] Kamal K. Seth, "A New Analysis of the R Measurements: Resonance Parameters of the Higher Vector States of Charmonium", hep-ex/0405007.

[62] G. Punzi, "Sensitivity of searches for new signals and its optimization", eConf **C030908** (2003) MODT002 [arXiv:physics/0308063].

[63] C. Amsler et al. (Particle Data Group), Phys. Lett. B667, 1 (2008)

[64] arXiv:0808.1543v2 [hep-ex] (2008)

[65] S. K. Choi *et al.*, Phys. Rev. Lett.91, 262001 (2003).

[66] S. Uehara *et al.*, Phys. Rev. Lett.96, 082003 (2006).

[67] S. K. Choi *et al.*, Phys. Rev. Lett.94, 182002 (2005).

[68] K. Abe *et al.*, Phys. Rev. Lett.98, 082001 (2007).

[69] T. Appelquist *et al.*, Annu. Rev. Nucl. Part. Sci. **28**, 387 (1978).

[70] B. Aubert *et al.*, Phys. Rev. Lett.95, 142001 (2005).

[71] C. F. Qiao, J. Phys. G **35**, 075008 (2008).

[72] S. Zhu, Phys. Lett. B **625** 212 (2005).

[73] C. Z. Yuan *et al.*, Phys. Rev. Lett.99, 182004 (2007).

[74] X. Liu, Eur. Phys. J., C **54** 3, 471 (2008).

[75] B. Aubert *et al.*, Phys. Rev. Lett.98, 212001 (2007).

[76] X. L. Wang *et al.*, Phys. Rev. Lett.99, 142002 (2007).

[77] C. Amsler *et al.*, Phys. Lett. **B** 667, 1 (2008).